

Copyright  
by  
Sigfried William Haering  
2010

**The Thesis Committee for Sigfried Haering certifies that  
this is the approved version of the following thesis:**

**Nanoparticle Mediated Photodisruption**

APPROVED BY

SUPERVISING COMMITTEE:

---

Adela Ben-Yakar, Supervisor

---

Carlos Hidrovo Chavez

**Nanoparticle Mediated Photodisruption**

by

**Sigfried William Haering, B.S.M.E.**

**THESIS**

Presented to the Faculty of the Graduate School of  
The University of Texas at Austin  
in Partial Fulfillment  
of the Requirements  
for the Degree of

**MASTER OF SCIENCE in ENGINEERING**

THE UNIVERSITY OF TEXAS AT AUSTIN

August 2010

Dedicated to the pals.

## Acknowledgments

I wish to thank the multitudes of people who helped me. Time would fail me to tell of . . .

# **Nanoparticle Mediated Photodisruption**

Sigfried William Haering, M.S.E.

The University of Texas at Austin, 2010

Supervisor: Adela Ben-Yakar

We present experimentally determined photodisruption enhancement of 50 nm gold spheres irradiated with 780 nm 180 fs pulses using a pump-probe scattering system. Our results indicate a 300 nm cavitation bubble threshold reduction of 31 times when compared to an ultra-pure water base control solution. We utilize a method of matching time between bubble initiation in a continually circulated nanoparticle solution with theoretical focal volume size dependent time between particle-focal volume collision events based on simple particle kinetics. We propose the observed photodisruption is due to electrostatic particle ablation kinetics due to electron photoemission. We apply the Fowler-Dubridge theory for photoemission to nanospheres experiencing strong near-field enhancement to describe particle electric fields induced by non-zero particle charge densities resulting from emitted electrons. An apparent ultra-energy efficient photodisruption mechanism results from multiphoton emission processes in the sub 100 femtosecond pulse regime exceeding typical methods utilizing explosive boiling. In the process of explaining experimental results, we develop a near complete picture of nanoparticle mediated photodisruption as a function of identified relevant system non-dimensional groups and particle enhancement. These results may be used to guide the selection of laser and particle parameters for imaging and different photodisruption regimes.

# Table of Contents

<b>Acknowledgments</b>	<b>v</b>
<b>Abstract</b>	<b>vi</b>
<b>List of Tables</b>	<b>ix</b>
<b>List of Figures</b>	<b>x</b>
<b>Chapter 1. Introduction</b>	<b>1</b>
1.1 Motivation . . . . .	2
1.1.1 Cancer Diagnosis and Treatment . . . . .	3
1.1.2 Gene Study and Therapy . . . . .	4
1.2 Modeling and Experimental Overview . . . . .	5
<b>Chapter 2. Theory and Literature Review</b>	<b>7</b>
2.1 Photodisruption and Optical Breakdown . . . . .	7
2.2 Laser Induced Cavitation Bubbles . . . . .	10
2.2.1 Bubble Formation Mechanisms . . . . .	12
2.2.2 Bubble Dynamics . . . . .	14
2.2.3 Cellular Manipulation . . . . .	18
2.3 Nanoparticles . . . . .	19
2.3.1 Particle-Light Interaction . . . . .	21
2.3.2 Specific Targeting . . . . .	22
2.3.3 Particle Heating . . . . .	24
2.3.4 Electron Emission . . . . .	26
2.3.5 Enhanced Photodisruption and Cellular Manipulation . . . . .	29

<b>Chapter 3. Experimental Methods</b>	<b>34</b>
3.1 Experimental Setup . . . . .	34
3.2 Particle-Focal Volume Interaction . . . . .	36
3.3 Data Processing . . . . .	41
3.3.1 Data Reduction . . . . .	42
3.3.2 Gilmore Model of Bubble Expansion & Collapse . . . . .	44
<b>Chapter 4. Theoretical Modeling and Numerical Analysis</b>	<b>48</b>
4.1 Particle Heating . . . . .	48
4.1.1 Two-Dimensional Electron and Phonon Heating . . . . .	49
4.1.2 One-Dimensional Particle and Medium Heating . . . . .	54
4.2 Electrostatic Ablation of Particles . . . . .	60
<b>Chapter 5. Numerical Results and Discussion</b>	<b>67</b>
5.1 Particle Electron Equilibrium . . . . .	67
5.2 Maximum Temperature Surfaces . . . . .	69
5.3 System Temperatures Evolution . . . . .	73
5.4 Particle Ablation Threshold . . . . .	76
<b>Chapter 6. Experimental Results and Discussion</b>	<b>82</b>
6.1 Threshold Reduction . . . . .	82
6.2 Size Distribution . . . . .	89
<b>Chapter 7. Conclusions</b>	<b>91</b>
<b>Appendix</b>	<b>93</b>
<b>Appendix 1. Neglect of Brownian Motion</b>	<b>94</b>
<b>Appendix 2. Scaled Temperature Response Surface Fits</b>	<b>96</b>
<b>Bibliography</b>	<b>101</b>
<b>Vita</b>	<b>115</b>



## List of Tables

2.1	Laser-induced photodisruption thresholds in biological settings . . .	20
2.2	Single gold particle mediated photodisruption thresholds . . . . .	31
2.3	Variable loading effects of gold sphere mediated photodisruption . .	32
2.4	Clustered and other non-biological particle mediated photodisruption thresholds . . . . .	32
2.5	Biological particle mediated photodisruption thresholds . . . . .	33
4.1	Constants and material properties . . . . .	54
5.1	Maximum temperatures for $\beta = 1.4 \times 10^3$ . . . . .	75

## List of Figures

2.1	Absorption efficiencies for gold nanospheres . . . . .	23
3.1	Experimental Setup Picture . . . . .	36
3.2	Experimental Setup Schematic . . . . .	37
3.3	Flow cell velocity . . . . .	39
3.4	Scattered signal edge find . . . . .	43
3.5	Effects of dynamic interior bubble pressure . . . . .	47
4.1	2D electron source term . . . . .	52
4.2	Surface near field enhancement . . . . .	66
5.1	Electron temperature difference across particle . . . . .	68
5.2	Maximum scaled surface water temperatures . . . . .	70
5.3	Maximum scaled particle lattice temperatures . . . . .	71
5.4	Maximum scaled particle electron temperatures . . . . .	72
5.5	Three temperature system behavior . . . . .	74
5.6	Photodisruption diagram . . . . .	77
5.7	38 nm Au sphere photodisruption diagram . . . . .	79
6.1	Nanoparticle bubble measurements . . . . .	83
6.2	Blow-up of nanoparticle bubble measurements . . . . .	84
6.3	Experiment photodisruption diagram . . . . .	88
6.4	Bubble size distribution . . . . .	89
2.1	Electron subsystem numerical fit . . . . .	98
2.2	Phonon subsystem numerical fit . . . . .	99
2.3	Water subsystem numerical fit . . . . .	100

# Chapter 1

## Introduction

This thesis discusses the application, theory, optimization, and experimental confirmation of nanoparticle mediated photodisruption via cavitation bubble formation for the purpose of highly selective and precise cellular manipulation and necrosis. In particular, we examine the mechanisms of the interaction of femtosecond NIR laser pulses and nanoscale gold particles. By fully understanding the processes and effects of simultaneous absorption and focusing of short-pulsed irradiation in the near-field of nanoparticles, we may utilize these particles in biological systems and submicron-scale fabrication to guide and tune photon induced disruption (photodisruption) of the surrounding medium. Additionally, particles may be functionalized to target specific bio-marker of our choice to selectively photodisrupt cellular membranes and tissue. These unique properties coupled with light of the near-infrared therapeutic window, where tissue exhibits minimal scattering and absorption, offer the prospect of both non-invasive and highly selective manipulation of individual or groups of cells.

First, we briefly discuss the general motivation and need for such technique and then move to theories and types of photodisruption with review of associated previous works. General mechanisms of photodisruption are explored followed by their potential enhancements using nanoparticles. A pump-probe experimental setup is utilized to determine laser-induced cavitation bubble sizes created with and without nanoparticles to show potential enhancements, minimum damage thresholds, extent and variability of damage associated with these methods. We then

transition to numerical modeling of these processes with an emphasis on the differing disruption regimes and frame our experimental findings within the context of the presented model results and theories. Additionally, we provide general guidelines for the selection of specific particle and laser parameters based upon derived relevant non-dimensional groups to attain desired imaging or photodisruption outcomes.

## 1.1 Motivation

The enhanced absorption and scattering properties of noble metal nanoparticles and their ability to "focus" light near their surface present a wealth of potential applications. With the application of surface molecules, particles allow for the identification and manipulation of a wide variety of sub-diffraction size objects such as sub-cellular organelles, proteins, and DNA. Increased light scattering and luminescence from nanoparticles at selective plasmonic wavelengths allows for the tracking of specific interactions and identification of specific targets such as individual cancerous cells or specific genes through a variety of imaging modalities. Increased absorption and near-field enhancement result in a very precise application of laser energy to induce transient or permanent modifications to particle surroundings. In addition, fabrication of particle-sized surface features, such as trenches and holes, may lead to manufacturing of new optical and photonic components and nano-devices. Perhaps most promising is the use of nanoparticles and light to selectively porate cellular membranes. So-called optoporation allows for the introduction of exogenous material such as DNA into targeted cells and also, in the case of cancerous cells, for inducing necrosis.

### 1.1.1 Cancer Diagnosis and Treatment

In the US, cancers are attributed to over half a million deaths per year and are the second leading cause of mortality [1]. Skin cancer is the most frequently occurring and diagnosed cancer due to the skins constant replication and exposure to radiation. Up to 85% of all types of human cancers arise from the epithelium [2]. Cancer cells confined to the epidermis can become metastasized by entering lymphatic system and blood vessels and be transported to vital organs forming new life threatening tumors. Thus, it is imperative to identify and remove such cancers before metastasis can occur. Current diagnosis and treatment typically involve biopsies and excision of cancerous cells and neighboring healthy tissue. Such treatments can lead to significant scarring and incomplete removal of all malignant cells allowing the cancer to return. The depth of such skin cancers may be on the order of millimeters and may be below a layer of healthy tissue [3]. However, early stages of skin cancer are often confined to the relatively shallow epidermis. A method targeting only cancerous cells and capable of penetrating to epidermal depth ranges in human tissue is a highly desirable and potentially life-saving technique when diagnosed early before metastatic spread.

While promising, optical based methods suffer due to the turbidity of human tissue. Scattering and absorption of tissue attenuates pulsed light-based treatments by both reducing the overall energy and broadening the beam spot size. Broadening of beam spots result in decreased laser fluences (energy/unit area) thus, a decrease in delivered energy. Choosing light in the near-infrared range minimizes these effects but in order to prevent damage to healthy surrounding tissue there is still a need to reduce the amount of deposited energy necessary to induce selective disruption of malignant tissue before optical-based therapy and diagnosis becomes a clinical reality. Additionally, we would like to be able to apply light broadly over regions

of malignant tissue without having to resort to spatial scanning of focused laser beams. Such scanning methods would require extremely precise mechanical control and prolonged patient immobilization, making them very impractical. Thus, optical-based treatments and screening methods must accommodate relatively unfocused light while resulting in highly selective regions of photodisruption.

### **1.1.2 Gene Study and Therapy**

Though we have made great strides identifying specific genes directly or partially responsible for various diseases, the function and complex interactions of the some 20,000 plus genes remains largely a mystery. By introducing exogenous nucleic acids into cells we can study the function of specific genes and potentially treat genetic diseases such as cystic fibrosis and sickle cell anemia. Gene therapy by transfection or transduction introduces foreign genes into cells which can alter the genetic program of the cells. In this way, we may permanently alter cellular function by providing missing genetic material, correcting defective genes, or increasing the expression of proteins from genes already present [4]. Additionally, it has been demonstrated that adult cells can be reverted into a totipotent or pluripotent state so that ones own cells may be used to heal previously irreparable damage such as severed nerve connections in cases of paralysis [5]. However, there is still no reliable, completely successful method to transport these reparative genes into cells. To one day be able to safely eliminate genetic diseases, we must develop methods of rapidly and sequentially introducing varying gene combinations to study these interactions and effects.

Gene studies have been hampered by the fact that bare DNA will only very rarely internalize into cells naturally [6]. Existing methods include: transduction by viral vector thus infecting cells with genetic material, transfection by cellular

uptake of gene loaded liposomes, and transfection by transient membrane poration by means including electroporation, sonoporation, and focused pulsed lasers. Viral based carriers suffer from the difficult process of creating tailor-made viruses and avoiding host immune system recognition [7]. Transfection by liposomes also involve complex formation processes and limited efficiency due to immune system response. Additionally, the formation process may involve cytotoxic materials and many cell types of particular scientific interest, such as nerve and stem cells are difficult to transfect with this method. Transfection methods such as electroporation and sonoporation are simpler and cheaper but, often suffer from reduced cell viability and very little potential for *in vivo* application. Thus, an efficient, cheap, and safe physical method for gene therapy studies is still elusive.

## 1.2 Modeling and Experimental Overview

There is a new opportunity to utilize light-interacting nanoparticles to overcome some of the difficulties outlined above with cancer diagnosis, treatments and gene therapy. However, research has been generally performed sporadically and lacks a complete analysis of the mechanisms and optimization of the processes involved. To this end, we seek to understand the exact extent to which nanoparticle based treatments and experiments are viable options and how they can be optimized by examining the multiple and complex photodisruption pathways they present.

We use a relatively simple experiment to measure particle photodisruption enhancements by detecting bubbles initiated around irradiated nanoparticles. This pump-probe system relies on femtosecond excitation pulse to induce bubble formation and a continuous wave interrogation beam which scatters through these rapidly expanding and collapsing bubbles. The probe beam signal may be collected after bubble scattering and analyzed to determine resulting photodisruption. This

experiment provides valuable insight into nanoparticle assisted photodisruption enhancement and damage variability.

To explain our experimental results and gain further insight into the underlying processes and mechanisms behind particle enhanced disruption, we performed a series of numerical studies. Numerical analysis of particle damage mechanisms must be performed due to the difficulties of performing experiments to detect and measure photodisruption on these extremely small size scales and extremely short time scales of interest here. We used a two-dimensional model of particle heating to determine the validity of lumped (uniform temperature) approximations of particle electron temperatures during laser heating. Afterwards, a one-dimensional heating model is used to define particle melting and medium boiling damage regimes based upon relevant system non-dimensional parameters. Finally, we modify an additional electron emission model to the case of particles and pulsed laser interaction to describe and predict particle ablation.

Using these methods, we have identified laser-induced nanoparticle-mediated damage mechanisms and formation thresholds. Although not entirely comprehensive, this work represents the most complete description to date. These results provide indications for the applicability of using short pulsed laser interactions with noble metal nanoparticles in both research and clinical settings as well as guidelines for other researches to selectively tailor desired outcomes.



## Chapter 2

### Theory and Literature Review

In this thesis, we are interested in the results of counter-intuitive situations where transparent media become absorbing and reflective to light while metals become lenses and antennae, focusing light in unique and predictable patterns. The mechanisms driving these seemingly bizarre interactions are fairly well-understood and are not the subject of the current work. However, a brief description of these processes is necessary to develop the optimization and experiments of nanoparticle-light photodisruption that are the focus of this thesis.

We first examine the phenomena of optical breakdown and the various resulting damage pathways with an emphasis on cavitation bubbles. Next, nanoparticle interaction with light is reviewed with a development of the theory of how these particles can be used to guide and enhance photodisruption. Previous works are, of course, inexorably tied to this theory review and are thus also included here. Although discussed in this section, previously derived and utilized equations are presented in Chapter 3.

#### 2.1 Photodisruption and Optical Breakdown

Typically, light does not interact with transparent media such as water and glass. If an electron of a nearly transparent dielectric material does interact with incident photons, or "feels" its electric field, the energy gained is not enough to excite it to the conduction band. Such quasi-excited electrons will near-immediately decay

through electron-photon relaxation resulting in the re-emission of the photon or electron-phonon relaxation resulting in medium heating. However, as the intensity of incident irradiation is increased, the probability of multiple photons interacting near-simultaneously with a single valence electron becomes non-negligible. Through this nonlinear mechanism, electrons may gain enough energy to be freed using tightly focused short laser pulses. From an alternate perspective, the electric field strength corresponding to tightly focused pulsed laser beams may exceed the binding electric field of valence electrons.

Excellent reviews of laser-induced optical breakdown and plasma formation are given in [8] and [9] among others, we provide a brief recount here. Multi-phonon ionization (MPI) events become probable as absorbed energy of multiple photons by a single electron exceed the material's band gap energy and the electron is promoted to the conduction band becoming 'quasi-free.' This freed electron may then continue to absorb photon energy and may gain sufficient energy to excite other electrons through additional collision events with bound electrons. Electron excitation past the conduction band energy by photons need not be simultaneous as there are no longer "forbidden" quantum states, that is, every absorbed photon will translate into increased kinetic energy. However, during quasi-freed electron absorption of a photon, ions or atoms must also interact in order to simultaneously maintain conservation of energy and momentum thus, the electrons are never truly "free" though we will use this term from now on as is customary. This process is referred to as inverse Bremsstrahlung ionization and through series of these events, the electron has enough energy to free another electron through impact ionization. These newly free electrons undergo additional inverse Bremsstrahlung collision events and gain enough energy to free more electrons resulting in a "cascade" or "avalanche" of free electrons. Depending upon the wavelength of incident light, so-called tunneling

ionization may also be significant or even dominate as the seeding mechanism. Here, the incident electric field alters and reduces the barrier height for electron promotion so that they may "tunnel" to the conduction band without absorbing the same amount of energy as MPI.

In short, MPI and tunneling ionization seeds inverse Bremsstrahlung ionization resulting in avalanche ionization and an overall exponential growth in free electron population during laser pulses. So-called optical breakdown is achieved when the resulting plasma becomes both strongly reflective and absorbing to additional incident radiation as the plasma frequency is elevated to the incident electric field frequency due to a critical density of free electrons ranging from  $\rho_e = 1$  to  $9 \times 10^{21} \text{ cm}^{-3}$  for the visible to NIR spectrum. The plasma is somewhat similar to a conducting metal at this point, ions surrounded by a sea of flowing electrons. Femtosecond pulses have been shown by both calculations and experiments to require approximately two orders-of-magnitude less energy than nanosecond pulses to induce critical plasma formation due to the higher temporal confinement of energy in addition to the spatial confinement provided by focusing [10].

A distinct advantage of MPI initiated processes over linear single photon absorption processes is their inherently increased spatial confinement. Given a focused beam, single photon processes will occur throughout the beam's propagation leading to significant attenuation above the focal plane. Multiphoton processes will only occur where the intensity is above the threshold value for the particular process (ablation, fluorophore excitation, etc.). Typically, laser conditions are selected so this process only occurs in the focal volume. Thus, MPI processes reduce out-of-plane attenuation and increases signal-to-noise ratios. Additionally, due to the Gaussian spatial nature of laser cross-sections, the intensity necessary to achieve MPI or tunneling ionization may only occur over a small portion of the beam.

Sub-diffraction limited photodisruption and manipulation is achievable due to this spatial distribution of energy within a laser beam [8].

Simple zero-dimensional rate equations are often used to find the temporal evolution on free electrons due to the effects of MPI, tunneling, cascade, diffusion, and recombination effects [11, 12, 13, 8, 9]. More complicated one- and two-dimensional models have also been used to capture effects of laser beam spatial distribution, high NA self-focusing effects, and plasma defocusing [14, 15, 16, 17]. No models have been developed to include the effects of nanoparticles on free electron generation to this point.

Nonlinear absorption of focused ultrashort laser pulse provides an efficient means of converting electromagnetic energy into chemical, thermal, and mechanical energy for the purpose of highly localized and non-invasive micromanipulation. Photodisruption of this sort results in the formation of plasmas followed by creation of rapidly decaying pressure waves, highly reactive free radicals, medium heating, and possible cavitation bubbles [8]. Various combinations of laser parameters result in different damage pathways: continuous or long pulses of low power tend to results in large heat-affected-zones (HAZ), short pulses of low energy and high repetition rates result in accumulation of reactive oxygen species and other free radicals, while short pulses of high energy produce cavitation bubbles and shock waves.

## **2.2 Laser Induced Cavitation Bubbles**

The rapid expansion of laser-induced cavitation bubbles and associated shock wave propagation cause mechanical damage by introducing both high strains and strain rates in the surrounding material. Cavitation-induced photodisruption results in a more defined and isolated region of damage than laser-induced material decomposition and laser-generated heat diffusion while still being tunable to sub-

diffraction limited scales. Free electrons generated by ionization will be significantly diminished long before bubble collapse due to the short electron-phonon relaxation times of a few picoseconds. Long-lived free radicals will still be produced during bubble formation however, bubble walls act as a natural confinement mechanism impeding the diffusion of these species. The use of individual bubbles for disruption as opposed to the accumulation of reactive species using multiple pulses to cause chemical breakdown results in higher disruption confinement due to reactive species diffusion versus stationary bubble formation. Furthermore, bubble walls act as an insulating barrier and greatly reduce heat transfer to surrounding medium confining thermal effects. Additionally, bubbles and shock waves may be formed at temperatures below the ambient boiling temperature of the medium. Thus, we may use cavitation bubbles to finely disrupt tissues, cells, and organelles without direct contact and without the creation of large populations of harmful free radicals or the creation of significant HAZ.

Cavitation bubble dynamics and formation mechanisms have been studied extensively in aqueous media alone [18, 19, 20, 21, 22, 23]. Previous characterization of nanoparticle enhancement and resulting bubble sizes have been limited to primarily pico- and nano-second pulse regimes [24, 25, 26]. Only very limited information is available for femtosecond pulse interactions with nanoparticles and is specifically related to the inception of vapor shell around the nanoparticle [27]. Additionally, there is a complete lack of data and analysis pertaining to the variability of damage caused by nanoparticles exposed to typical Gaussian spatial profile beams where particles will experience drastically different intensities at different locations. In order to understand and utilize nanoparticle mediated photodisruption we must characterize both the enhancement and the possible range of damage resulting from their use.

### 2.2.1 Bubble Formation Mechanisms

Bubble formation is often divided into two separate regimes: explosive boiling and tensile cavitation. However, this distinction is fundamentally unnecessary as the terms cavitation and boiling are essentially identical phenomena in a thermodynamic sense. Boiling usually serves to indicate isobaric conditions while cavitation indicates isothermal conditions. Thus, where this separation is often used is in defining bubble formation in terms of ambient thermodynamic states. Laser-induced bubbles may be formed by rapid localized heat deposition from electron-lattice recombination due to collision events between energetic electrons and cold ions and/or fluid rupture due to pressure/shockwave expansion with trailing rarefaction wave. The initial shockwave is a result of the high energy and pressure plasma being formed essentially instantaneously with respect to the acoustic relaxation time in the medium. Thus, the term explosive boiling is used when the medium temperature meets or exceeds the ambient vaporization temperature while cavitation is used when the medium ambient tensile yield stress is achieved. Note cavitation bubbles may be created without inducing boiling when short laser pulses are used [8].

Regardless of the label and regardless of whether light (focused pulsed laser beams), acoustic (piezo/horns), electrical (spark-gaps), or mechanical (impeller blades) induced, bubbles are formed when the thermodynamic state of the fluid medium exceeds the binodal and before or at the spinodal state. The binodal defines the boundary of liquid-vapor coexistence; under homogeneous thermodynamic conditions, exceeding the binodal leads to vaporization and boiling. However, if energy is deposited faster than diffusion time scales, rapid temperature confinement results with accompanying vapor pressure rises taking place slower than the temperature rise and the binodal no longer defines phase change [28]. The kinetic spinodal defines a locus of thermodynamic states where the average nucleation time of the

vapor phase becomes shorter than the average decay time of fluctuations to local equilibrium. Near this critical state, bubble formation is imminent while prior to this limit, spontaneous microscopic pockets of vapor that develop will rapidly disappear. This phenomena is similar to the onset of turbulence in fluid flows where transition region eddies will be quickly dissipated by viscous diffusion.

An alternative statement of the kinetic spinodial is when the work required to increase the radius of a randomly nucleated vapor inclusion approaches zero, that is, when the derivative of the nucleation barrier work function with radius is zero,  $\frac{\partial W}{\partial r}_{P,T} = 0$ . This work function depends upon the viscosity of both the liquid and vapor states, surface tension, vapor pressure, and ambient pressure. Accurate relation between all these parameters relies on an accurate fundamental relationship for the medium. Limits to accurately predicting bubble formation are due the lack of an accurate fundamental relationship for water, especially in metastable states. Experimental data such as the IAPWS-95 [29] must be used when attempting to predict bubble formation and behavior. However, Kiselev [30] derived a kinetic spinodial function for water using the analytic fundamental relation for water of Saul and Wagner [31] over the regimes of superheated and stretched water with excellent agreement of experiments in the superheated regime and satisfactory agreement in the stretched fluid regime.

An interesting result of this formulation is the ability to calculate critical stable bubble radii as a function of fluid temperature. Over a range 300-600K, this radius is relatively constant at about 1 nm. It is only after 600K that the minimum stable bubble radius begins to rapidly increase. This result has important implication for bubbles formed around nanoparticles and will be discusses further later.

With the kinetic spinodial limit, it is possible to calculate bubble formation

thresholds if we can determine the temperature and pressure of the fluid from the applied laser irradiation. The temperature distribution resulting from laser-induced plasma for femtosecond pulse can be determined roughly from the total number of free electrons generated during the pulse multiplied by the average energy gain of the electrons. Simple heat diffusion may be used to determine the spatial distribution of temperature over time if desired (assuming no bubble formation) or for longer pulse durations where heat will diffuse during the pulse. Initial pressure distributions in the free-electron generation may be calculated from the integral of the thermal expansion coefficient over the fluid compressibility from pre- to post-pulse temperatures  $p(r) = \int_{T_o}^{T_f(r)} \frac{\beta(T)}{K(T)} dT$  [8]. The determination of the evolution of fluid pressure is complicated by the creation of plasma-induced pressure waves and must be determined using the thermoelastic wave equation. A fast solution method for pressure wave propagation is presented in [32]. With the pressure and temperature distribution known after the laser pulse, approximate bubble thresholds may be determined.

Using this outlined method, Vogel and co-workers analytically determined an approximate cavitation bubble initiation threshold of  $5.1 \times 10^{12} W/cm^2$  in pure water for 800 nm 100 fs laser pulses[8]. Their theoretical minimum bubble radius is 70 nm while the kinetic spinodal formulation by Kiselev predicts minimum stable bubble sizes on the order single nanometers[30]. Though these predictions may seem to be in conflict, Vogel's result indicates the peak radius for an expanding and collapsing bubble while Kiselev's indicate the minimum stable size for non-oscillating bubbles.

### 2.2.2 Bubble Dynamics

Once a bubble has been initiated, the vapor pressure causes a rapid expansion of the bubble walls. Heat will be continually transferred from the vapor through



the bubble wall resulting in a reducing vapor pressure. However, if the bubble created is smaller than the heated region by the laser pulse, heat may actually flow into the bubble for a brief period further fueling its expansion. In the case of high energy, longer pulses on the order of nanoseconds, the laser itself may fuel bubble expansion by heating bubble vapor content while it expands. Once the bubble expands to a size where the interior bubble wall pressure approaches equilibrium with the ambient pressure and Laplace pressure, the wall slows and collapses as heat is continually removed via conduction and the vapor temperature drops due to expansion. Due to the high bubble wall velocities, a second pressure wave typically separates and continues through the fluid while the actual wall arrests and retreats [9]. During the bubble collapse, the vapor pressure rises and temperature increases so it may again become large enough to cause an expansive rebound. A third pressure wave may be emitted at the bubble's minimal radius due to fluid compression to a near singular point [33]. This sequence may be repeated multiple times leading to rapidly oscillating bubbles of diminishing maximum radii before the bubble energy is finally exhausted and it breaks up into a short-lived vapor-liquid mixture. Viscous damping of the liquid serves to reduce both bubble radii and oscillation times.

Not accounted for in this discussion is vapor condensation across the bubble wall. This effect is typically assumed to be negligible in treatments [18, 21]. Akhatov *et al.* considered evaporation-condensation kinetics in [33] using an assortment of boundary matched models and shifting equations of state to show an appreciable dependance of bubble dynamics with inclusion of this effect for bubbles of approximately  $500\mu m$  radius. However, condensation occurs only in the thin Knudsen layer at the bubble wall surface. For larger bubbles of this size, there is a significant area over which the effects of mass loss through the wall and latent heating insulation occurs. For smaller bubbles of interest in this research, these effects are negligible.

To predict bubble expansion and collapse we may turn to the treatment of Gilmore [18] where he reduced the governing equations for flow of a compressible fluid surrounding a spherical bubble to a single bubble wall velocity nonlinear differential equation. As opposed to other models such as the commonly used Rayleigh model, Gilmore includes the effects of surface tension ( $\sigma$ ), fluid viscosity ( $\mu$ ), and compressibility. These factors are of crucial importance in the cases of Bond number, in terms of bubble wall acceleration ( $Bo = \frac{\rho \ddot{r} r^2}{\sigma}$ ), and Reynolds number ( $Re = \frac{\rho \dot{r} r}{\mu}$ ) are on the order of unity, that is, when predicting small energetic bubble behavior. Conservation of mass and momentum are reduced with the assumptions: spherically symmetric and irrotational flow, density is a function of pressure alone and follows isentropic compression behavior given by the Tait equation of state, and terms including both viscosity and compressibility are negligibly small. We use the resulting model to interpret experimental results. Full-field numerical models have also been performed but are significantly more complex due to the vapor bubble interface and discontinuous material properties experienced there and are ultimately limited by the accuracy of the equation of state used [34].

Measured and calculated strengths of laser-induced pressure waves vary depending upon the study and experimental parameters [8, 35, 20, 21]. The strength of shockwaves increase with shorter laser pulses because the deposition of energy and pressure increase in the plasma occur more rapidly than the acoustic relaxation time of the material. In general, for femtosecond pulses in pure water, pressure waves decay with an approximate  $r^{-1.1}$  to  $r^{-2}$  [20], an initial peak compressive pressure wave equal to approximately 25% the plasma pressure, and a maximum rarefaction pressure equal to approximately 40% of the maximum compression [8]. The exact values depend upon laser conditions (pulse duration, focusing conditions, and wavelength). These approximate percentages may be used when considering

damage tolerances of nearby structures.

When bubbles are generated near boundaries, an asymmetric pressure distribution and flow field will develop during the expansion and collapse sequence. The result is some combination of bubble motion, breakup and jet formation depending on the complex interaction between the bubble size, proximity to the boundary, fluid properties, and boundary properties. The mechanisms behind the jet formation are still unclear however, it is clear that jets develop when one portion of the bubble collapses at a different rate than other regions and that regions where the curvature is highest correspond to where the jets will initiate from [33, 36, 37].

Multiple possible bubble-jet outcomes are possible depending upon the stand-off distance ( $d$ ) and maximum bubble size ( $\gamma = \frac{d}{R_{max}}$ ). For  $\gamma = 1.1$  an axial jet forms from the boundary side of the bubble which pierces through the bubble and out into the solution; for  $\gamma = 0.75$  bubble collapses in an hourglass shape and two jets are created in equal and opposite directions; for  $\gamma = 0.62$  formation of a fluid jet initiating on the side away from the boundary side of the bubble which pierces through the bubble and impacts the boundary; finally, for  $\gamma < 0.45$  bubble directly pushes against the boundary and a jet of boundary material is ejected outward or a jet originated from the bubble pierces into the boundary [36]. These outcomes were determined for boundaries made of a polyacrlamide gel with a modulus similar to that of corneal tissue. For the relatively large bubbles of 1.5 mm radius used in this study, jets of over 900 m/s velocity were measured. Clearly, jets of this type may be the dominant damage mechanism when initiating bubble near or at cell membranes. An excellent summary of the various types of jet behavior near elastic boundaries is given in [37]. They used numerical simulations are used to perform a parametric study of various combinations of boundary material and  $\gamma$  conditions. There are currently no studies of sub-micron sized bubble-boundary interactions; it is possible

the surface tension may strongly reduce or completely negate any jet formation at these scales.

### 2.2.3 Cellular Manipulation

Cell disruption resulting from cavitation bubble creation may be caused by pressure waves, high tensile stress at the bubble wall, and/or bubble jet production. Of course, pulsed lasers may induce photodisruption by other previously identified mechanisms. Lipid membranes and cytoskeletons are well known for their ability to deform to a high degree without rupturing; this is due to the viscoelastic behavior of the material [38]. When low rates of loading are applied, cells behave as an elastic deformable solid with induced stress being a function of strain. Once the cell has been deformed, stress may be partially or completely relieved by cytoskeleton reorganization. However, at high deformation rates, cells behave more as a fluid and the induced stress is a function of the strain rate.

Rau *et al.* experimentally determined the yield stress of cells due to cavitation bubbles at high strain rates of approximately  $95 \mu s^{-1}$  [39]. They applied 6 ns 532 nm pulses of 5-6  $\mu J$  to an area 400  $\mu m$  above a monolayer of cultured *PtK<sub>2</sub>* cells. High-speed photography was used to track both the bubble expansion and shockwave propagation. Laser-induced shock waves of 480MPa initial strength did not seem to have an effect on the cell membrane integrity while the actual cavitation bubble resulted in cell removal surrounded by an area of dead cells. An observed shear stress of 60-85 KPa at the bubble wall induced cell lysis. This experiment, while an invaluable first step, leaves much to be determined. For instance, the seemingly unimportant shockwave may have actually served as a pre-rupture mechanism, weakening cells for the bubble wall. Irradiation with shorter pulses will develop stronger shock waves as opposed to nanosecond pulses of similar total

energy thus, these results may not be applicable to femtosecond pulses. Additionally, cells affixed to a rigid boundary will certainly experience various pressure wave reflections altering their response as opposed to those in an *in-vivo* setting. Cells exposed to smaller single or multiple bubbles initiated adjacent to the plasma membrane may also have very different responses to bubble wall shear stress and emitted shockwaves.

Numerous studies involving cell poration, transfection, or necrosis using pulsed lasers have been performed with observed energy thresholds differing from study to study depending upon widely varying test conditions. The use of lasers to ablate biological material is not a new subject and multiple *in-vivo* applications are currently in use as well [40]. Some experimental biological manipulations without the use of foreign particles are given in Table 2.1 showing typical damage thresholds. Evident from this list is the complex interactions between different cell types and laser parameters. For instance, eventhough many femtosecond pulses of higher energy are used in [41] as compared to the longer single pulses used in [42] and [43], long nerve cells targeted along axons survive while more typical small ( $10\mu m$ ) circular retinal epithelium pigment (REP) cells die. As will be discussed later, melanosomes in REP are strongly absorbing structures in cells and are likely one cause of this discrepancy. Although, very specific and repeatable disruption may be obtained, where these current methods suffer is the requirement of precise targeting.

## 2.3 Nanoparticles

Plasmon resonant nanoparticles may mediate and guide photodisruption and bubble formation by both targeting specific biomarkers and greatly reducing the laser energy necessary to induce free electron generation, ablation, cavitation, and thermal therapy. These features allow for increased penetration in scattering media

Table 2.1: Laser-induced photodisruption thresholds in biological settings

Effect	Energy	$\tau_p$	$\lambda$ (nm)	Conditions	Ref.
50% REP death	114 $mJ/cm^2$	250 ns	527	excised monolayer	[42]
50% REP death	129 $mJ/cm^2$	350 ns	527	excised monolayer	[43]
50% REP death	140 $mJ/cm^2$	1 $\mu s$	527	excised monolayer	[42]
50% REP death	180 $mJ/cm^2$	1.7 $\mu s$	527	excised monolayer	[43]
50% REP death	223 $mJ/cm^2$	3.0 $\mu s$	527	excised monolayer	[42]
PtK2 death 240 $\mu m$ dia	8 $\mu J$ 0.8 NA	6 ns	532	cultured monolayer	[44]
PtK2 death 440 $\mu m$ dia	24 $\mu J$ 0.8 NA	6 ns	532	cultured monolayer	[44]
75% HL60 poration within $0.75R_{bubble}$	10 $\mu J$ 0.25 NA	6 ns	532	microfluidic chamber free cells	[44]
<i>C. Elegan</i> axotomy	2.2 $J/cm^2$ 1kHz 100 pulses	200 fs	780	<i>in-vivo</i> 1 $\mu m$ axons	[41]
pyramidal neuron necrosis	0.04 $\mu J$ 0.8 NA	200 fs	780	coronal brain slice	[10]
mouse NIH3T3 transfection	5 nJ 1.25 NA 1kHz 20 pulses	120 fs	800	culture cells EGFP expression	[45]
HeLa mitochondria transfection	0.39 nJ 76 MHz 2 $\times 10^6$ pulses	120 fs	930	culture cells EYFP expression	[46]

and reduced collateral radiation exposure. Nanoparticle enhanced photodisruption may act through multiple mechanisms: particle heating followed by conduction to surrounding medium, near field enhancement resulting in increased free-electron generation, and electron emission seeding cascade ionization and leading to particle ablation by electrostatic repulsion (so-called coulombic explosion). By tailoring particle geometries and material, we may selectively induce desired plasmon resonance frequencies to tune and optimize particles to laser wavelengths exhibiting minimal scattering and absorption in tissues. Thus, nanoparticle mediated cavitation bubble photodisruption is ideal for precise biological applications.

### 2.3.1 Particle-Light Interaction

Many studies have been performed showing the reduction of necessary laser power to initiate ablation and to induce high contrast for imaging [47]. These phenomenon are due to the coherent oscillation of surface conduction band electrons with respect to the lattice in resonance with incident electric fields, referred to as surface plasmon resonance (SPR) [48]. Particles of size much smaller than the wavelength of incident light may result in enhanced absorption and scattering by the particle as well as a large increase in the electric field near the particle surface. Freely moving electrons in metal particles polarize to a high degree in response to incident electric fields inducing a net charge at the surface. An electrostatic restoring force is generated to compensate for the non-zero surface charge difference resulting in electron cloud oscillations [48, 28]. Extinction cross sections can be achieved many more times larger than the physical particle area. Increased absorption is due to excited electron plasmon oscillations non-radiatively decaying via electron-phonon relaxation resulting in particle heating. Alternatively and simultaneously, the plasmon oscillations may decay radiatively by emitting photons at the resonant wavelength resulting in selective wavelength increased scattering. Finally, the coherently oscillating electrons create their own strong electric field in the vicinity of the particle causing the phenomena of near-field enhancement.

The resonance frequencies of nanoparticles are related to their size, shape, material (electron energy band structure), and external medium but are in the vicinity of  $\epsilon_r(\omega) = -2\epsilon_m$  where,  $\epsilon$  is the dielectric constant and the subscript r indicates the real, frequency dependent portion of the particle material and m indicates the medium. In general, smaller particles ( $< 40$  nm) exhibit strong absorption while larger particles exhibit larger scattering. Exact determination of the extent of scattering, absorption, and near field enhancement require use of the Mie solution of

Maxwell’s equations for spherically symmetric particles. Many programs and solution methods have been developed to perform these calculations [47].

Gold nanospheres exhibit resonance in the visible spectrum making them particularly useful for imaging. Silica core nanoshells and nanorods have been developed which exhibit resonance in the NIR spectrum with specific aims of deep-tissue imaging and disruption [49][50]. For this study, we focus on 50 nm diameter Au spheres irradiated with 780 nm light due to their frequent use and ease of fabrication to evaluate their potential for deep tissue application. Particles of this size and shape exhibit resonance at 540 nm with a peak efficiency ( $Q_{abs}$ ) of 2.7. At 780 nm, the efficiency is reduced to 0.15 (Figure 2.1). Clearly, these particles are not optimized for NIR applications however, we will show how significant enhancements are possible even with such a non-ideal combination due to near-field enhancement. The methods used may be applied to shells or rods for further tuning towards biological applications.

### 2.3.2 Specific Targeting

Gold nanoparticles are especially applicable for noninvasive seek-and-treat laser-based cancer treatment systems. Their biocompatibility is ideal for biomedical applications where other cytotoxic particles such as heavy metal quantum dots cannot be used. Additionally, particles can be altered to preferentially bind to tumor tissue by attaching proteins and ligands that bind with certain over expressed receptors on cancerous cells.

Many cancerous cells exhibit over expression of certain receptors such as epidermal growth factor receptor (EGFR), transferrin, and tyrosine. Antibodies corresponding to these receptors may be bound to particles so that non-specific administration results in highly specific cell targeting. El-Sayed *et al.* demonstrated



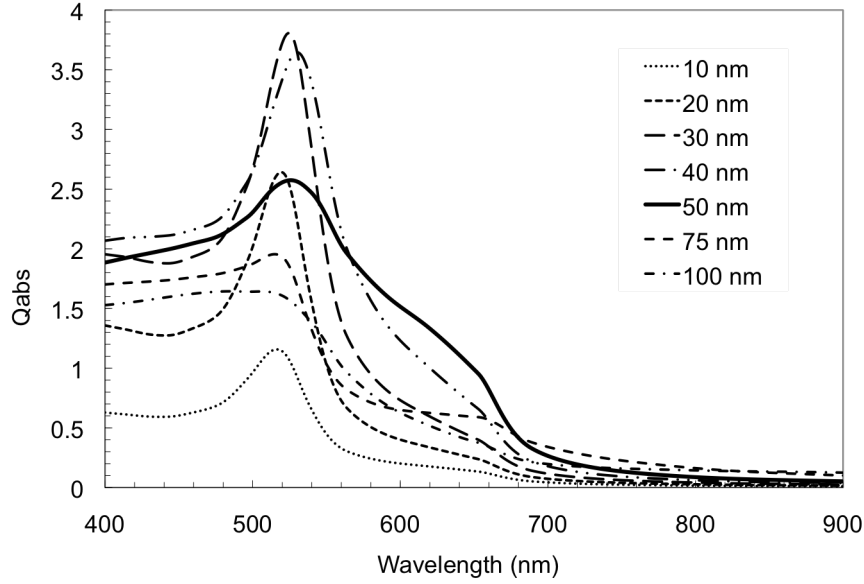


**Figure 2.1:** Absorption efficiencies for gold nanospheres in water medium of varying diameter as a function of applied laser wavelength. Courtesy of R. K. Harrison.

a 600 percent greater affinity for cancer cells of gold nanoparticles conjugated with anti-EGFR as compared to healthy cells. Additionally, particles bound with vascular endothelial growth factor (VEGF) have been shown to preferentially accumulate at abdominal tumors when injected intravenously through mouse tails [51].

A wide range of moieties can be conjugated to nanoparticles such as ligands, peptides, proteins, DNA, plasmids, and siRNA [6]. Particle-moiety binding is typically a process of covalent attachment where a single Au particle conduction band electron is exchanged with positively charged moiety or linker molecule ends. Other electrostatic adsorption binding processes, such as with polyethylene glycol or poloxamers, results in binding of hydrophobic portions with the particle surface and hydrophilic portions extending outward into solution forming nanoscale micelles.

Though not explored here, the natural agglomeration and endocytosis processes of gold particles on cellular membranes may lead to methods of direct drug delivery, without the need for radiation, by loading particles with drugs or genes which release or de-bond from the particle after some time. Recently, nanoparticle induced apoptosis in cancer has been demonstrated without the use of radiation [52]. Particles were loaded with arginine-glycine-aspartic acid peptide causing them to be internalized and adsorbed to the nucleus. Particles were seen to interrupt cell division and induce cellular apoptosis. These preliminary findings are not fully understood and are the subject of active investigation. However, were this technique found to be tailorable to multiple types of cancers, intravenous particle delivery may one day be used to kill hard-to-access and very lethal cancers such as glioblastoma multiforme (GBM) brain tumors.

### **2.3.3 Particle Heating**

Particle and particle-mediated surrounding medium heating proceeds in sequential manner. Initially, particle electrons are excited through the absorbed portion of incident radiation and may achieve temperature well exceeding that of the lattice due to the relatively low specific heat of electrons. Rapid electron-phonon relaxation occurs over a 10 - 50 picoseconds followed by conduction through the particle surface to the medium over a few hundred picoseconds to a few nanoseconds [28]. Interfacial conduction resistance between the particle and surrounding medium prolong the latter relaxation time with smaller particles exhibiting higher resistance. Exact relaxation times depend upon particle geometry, absorbed energy, and pulse duration; characteristic time scales will be developed in Chapter 3.

If the laser pulse is shorter than the electron-phonon relaxation time, nearly all of the deposited energy will be contained in the electron sub-system for a short

time. Excited electrons may be emitted or 'freed' from the particle during the laser pulse leading to cascade ionization seeding in the material immediately adjacent to the particle surface. If a sufficient number of electrons have been emitted from the particle, electrostatic repulsion from neighboring ions will exceed the lattice binding strength and initiate the process of particle ablation or Coulombic explosion if emission rates are large [53]. Similarly, if the laser pulse is shorter than the phonon-phonon relaxation time of the particle and medium, the particle may melt or even vaporize *prior* to boiling of the surrounding fluid.

Particle heating studies have been centered about the hyperbolic two-temperature model (TTM) for electron-phonon relaxation first derived by Qiu and Tien from the Boltzmann transport equation[54, 55]. In their derivation, they use the near-equilibrium approximation allowing the use of analytic functions for electron and lattice energy distributions. Strictly speaking, this is not appropriate for short energetic laser pulses because it enforces zero electric current during heating. More recently, Chen *et al.* relaxed this restriction to include terms for electron drift-diffusion and are thus, more appropriate forms for femtosecond laser pulses [56].

Only very limited particle heating experimental data is available; Plech and co-workers appear to be the only group who have devised a successful method of directly measuring nanoparticle heating due to laser irradiation [57]. They essentially used a pump-probe technique similar to the experimental setup used here with the exception of the probe beam being x-rays allowing the measurement of particle lattice expansion due to heating. The observed lattice expansion was related to particle temperature through bulk gold expansion coefficient.

### 2.3.4 Electron Emission

As briefly mentioned above, conduction band electrons at high temperatures may be emitted into the surrounding medium if the component of their kinetic energy oriented normal to the material interface exceeds the work function of the material. Low electron heat capacity and short energy deposition times associated with short pulse illumination result in highly non-equilibrated electron temperatures with respect to the lattice. Electron emission due to high temperatures, referred to as thermionic emission, will always be possible unless at absolute zero. High absorption cross sections of plasmonic particles coupled with short pulses create conditions favorable for emission of this sort.

In addition to thermionic emission, electrons may be released from surfaces by exposure to high intensity fields at the surface. Multiphoton emission is similar to MPI of dielectric materials relying on near-simultaneous interactions with sufficient number of photons to promote electron to energy states above the material work function. High intensity field strengths at a material surface result in sufficient photon density so that one or more photons are absorbed by conduction band electrons at the material surface causing their surface-normal kinetic energy components to exceed the barrier energy necessary for electron escape resulting in effective reduced work function. Electrons emitted in the later fashion would normally not have enough energy to escape the metal's potential well, that is, their temperature alone is insufficient. The near-field of nanoparticles is highly favorable for multiphoton emission due to large near-field intensity enhancements. Three-photon processes have been confirmed by Logothetis *et al* by monitoring photoelectric current induced in Au films irradiated with 690 nm pulses [58].

Due to the escape of excited electrons, particles gain high positive charge densities establishing electric fields which peak at the particle surface. The repulsion

force between the positive lattice ions may become large enough to exceed the lattice binding strength resulting in surface ablation by electrostatic repulsion. With sufficient applied fields, particles will near-instantaneously ablate, a process referred to as Coulombic explosion [59].

Based upon the Einstein equation, the Fowler-DuBridge theory of electron emission was the first to successfully incorporate both temperature and spectral dependence on thermionic and single photon assisted emissions [60]. Their derivation made use of the Fermi-Dirac electron energy distribution, constant electron absorption probability, and constant material work function to describe the total current density ( $J$ ) at a material surface. The resulting equation takes form from the integral of the probability of all electrons with temperature-dependence surface normal energies exceeding the intensity-dependent effective barrier height for promotion to vacuum that arrive at the surface. This theory was later generalized and extended to any number photon process by Bechtel and co-workers [61]. Their treatment decomposed all sources of emission into the sum of all discrete  $n$ -photon order processes to arrive at a total surface current density. Particle charge density may then be determined by integration of the Fowler-DuBridge current density over particle surface area and time. The induced electric field strength in the particle may then be determined from application of Gauss' law.

Space-charge potential barrier effects may increase the effective work function for electrons to be freed at high electron emission yields due to electron-electron repulsion near the particle after escaping. That is, some of the initially emitted electrons may not have sufficient energy to continue and be re-absorbed by the particle. Inclusion of this effect has been shown to be significant at high electron temperatures ( 0.4 eV) [62]. However, we have calculated space-charge potential barrier effects to be negligible due the relatively small number of electrons emitted from

our nanoscale particles before the onset of particle ablation.

We now turn our attention to a brief discussion of the regime where the electron temperature and field strengths are not sufficient to induce complete particle ablation but, the photoemission of electrons serves to seed avalanche ionization during the laser pulse. We have not performed the calculations involved with this discussion but, free electron donation and enhancement of free electron generation in the particle near-field are important for photodisruption utilizing generation of reactive species in tissue with multiple low power pulses.

In addition to electron emission serving as seeds for avalanche ionization, particle near-field enhanced electric and magnetic fields would increase local MPI rates and electron drift-diffusion via Lorenz forces. To include all these effects, a particle surrounding medium energy, momentum and species conservation solution for free electrons would be necessary in addition to particle electron temperature and photoemission calculations performed in this work. In particular, species continuity for electrons would utilize free electron generation source terms initially introduced by Kennedy *et al.* [63] and later refined by Noack *et al.* [11] of transparent dielectric ionization. Spatial distribution of the free electron density source term would be introduced by using a Gaussian electric field with modifications due to the particle near-field as appropriate. Both the electric field and magnetic field would be retained in Lorenz force terms in electron conservation of momentum as they both will increase electron transport by increasing kinetic energy and causing  $\mathbf{E} \times \mathbf{B}$  drift. The inclusion of field effects on electron transport and generation may be significant and would suggest an optimal pulse duration for particle free-electron seeding. That is, we would like to have a long enough laser pulse to have photoemitted electrons diffuse out from the near-field to the surrounding medium during the laser pulse to aid in avalanche ionization away from the particle while having a pulse duration

short enough to generate significant photoemitted electrons to seed the process. Such calculations will be the study of future works.

### **2.3.5 Enhanced Photodisruption and Cellular Manipulation**

We now present experimental particle enhancements observed by various other research groups and discussion general trends (Tables 2.2-2.5). It is difficult to compare results due to the varying test conditions and methods of determining photodisruption thresholds. Some groups list only cellular blebbing or dye uptake as thresholds while others cite observed bubble oscillation times or sizes or that simply bubbles were observed. Further confusing matters is a general lack of quantification of nanoparticle loading on cells.

We observe the following general trends which are largely expected from the previously discussed theory of nanoparticle assisted photodisruption mechanisms. Shorter pulse durations result in lower thresholds for ablation or detectable bubble formation; increased heat confinement as shorter pulses are below the particle-surrounding equilibration times. Clusters of particles reduces thresholds however, initial observed bubble sizes tend to be larger than those with single particles; a cluster of heated particles will transfer more energy to the surrounding medium reducing the threshold and creating bubbles at a minimum size of the cluster. There may be additional clustering enhancements resulting from shifting of the plasmon resonance. Smaller particles result in lower thresholds for bubble formation in the visible regime; higher absorption cross sections are typical for smaller particles. Particle loading of cells up to 250-500 particles reduces damage thresholds after which, diminishing returns with increased loading is seen. Natural organelles and substances can function as absorbers with similar threshold reductions as larger particles. This is an expected result as natural pigment particles are evolved to absorb in the visible

regime as a defense mechanism sunlight damage.

There are clearly large discrepancies between different research groups and occasionally, with the same groups; we examine one potential explanation for photodisruption threshold disagreements in Chapter 6. An important observation of all these experiments is the near complete lack of femtosecond pulse duration threshold measurements with nanoparticles or with NIR excitation wavelengths.



Table 2.2: Single gold particle mediated photodisruption thresholds

	Particle (size)	Fluence ( $KJ/m^2$ )	$\tau_p$	$\lambda$ (nm)	Effect	Ref.
	sphere 9 nm	0.09	100 fs	400	surface vapor initiation	[57]
	sphere 9 nm	0.29	100 fs	400	surface vapor initiation	[27]
	sphere 39 nm	0.3	100 fs	400	surface vapor initiation	[57]
	sphere 20 nm	2	8 ns	420	lymphoblast bubble initiation	[26]
	sphere 105 nm	0.845	6 ns	532	90% dye uptake kidney cells	[64]
	sphere 30 nm	7.2	500 ps	532	bubble formation in lymphoblasts	[24]
	sphere 30 nm	93.6	10 ns	532	20 ns bubbles	[25]
1	sphere 100 nm	173	10 ns	532	20 ns bubbles	[25]
	sphere 100 nm	50	500 ps	532	20 ns bubbles	[25]
	rods	3.5	500 ps	532	20 ns bubbles	[25]
14 x 15 nm	rods	35	10 ns	532	20 ns bubbles	[25]
14 x 15 nm	rods	30 77 MHz	200 fs	780	KB tumor blebbing	[65]
	sphere 500 nm	1.0	12 ns	532	bubble formation	[66]
	sphere 500 nm	2.0	240 ns	532	bubble formation	[66]
	sphere 500 nm	6.4	1.8 $\mu s$	532	bubble formation	[66]
	sphere 82 nm	1.98	5 ns	532	2.5 MPa bubble creation	[67]

Table 2.3: Variable loading effects of gold sphere mediated photodisruption

Particle (size/num)	Fluence ( $J/m^2$ )	$\tau_p$	$\lambda$ (nm)	Effect	Ref.
20 nm/100	5000	20 ns	565	50% lymphocyte death	[68]
20 nm/250	5000	20 ns	565	90% lymphocyte death	[68]
20 nm/500	5000	20 ns	565	95% lymphocyte death	[68]

Table 2.4: Clustered and other non-biological particle mediated photodisruption thresholds

Particle (size)	Fluence ( $J/m^2$ )	$\tau_p$	$\lambda$ (nm)	Effect	Ref.
Au sphere/cluster (30) 200 nm	600	10 ns	532	20 ns bubbles	[25]
Au sphere/cluster (30) 400-500 nm	880	500 ps	532	20 ns bubbles	[25]
Au sphere/cluster (100) 400-500 nm	20K	500 ps	532	20 ns bubbles	[25]
Au- $SiO_2$ shell/custer (60) 500-700 nm	120	500 ps	532	200 ns bubbles	[69]
Au- $SiO_2$ shell/custer (60) 500-700 nm	1000	10 ns	532	200 ns bubbles	[69]
Au- $SiO_2$ shell/custer (170) 500-700 nm	700	500 ps	532	200 ns bubbles	[69]
Au- $SiO_2$ shell/custer (170) 500-700 nm	5000	10 ns	532	200 ns bubbles	[69]
Latex/ $FeO_2$ sphere 0.77 $\mu m$	4000	20 ns	532	60% BAEC necrosis	[70]
Latex/ $FeO_2$ sphere 0.83 $\mu m$	3500	20 ns	565	70% T lymphocyte death	[68]

Table 2.5: Biological particle mediated photodisruption thresholds

Particle (size)	Fluence ( $J/m^2$ )	$\tau_p$	$\lambda$ (nm)	Effect	Ref.
blood cells / $7\mu m$	2810	10 ns	532	bubble generation	[71]
hemoglobin	19K	10 ns	532	bubble generation	[71]
melanosomes $0.8 \times 2.3 \mu m$	1400	12 ns	532	bubble formation	[66]
melanosomes $0.8 \times 2.3 \mu m$	3000	240 ns	532	bubble formation	[66]
melanosomes $0.8 \times 2.3 \mu m$	6000	$1.8 \mu s$	532	bubble formation	[66]
melanosomes $1 \times 2.5 \mu m$	550	30 ps	565	melanocyte cell death	[72]
melanosomes $1 \times 2.5 \mu m$	1100	20 ns	565	melanocyte cell death	[72]
melanin 150-200 nm	1100	20 ns	565	trabecular meshwork cell death	[72]

## Chapter 3

### Experimental Methods

We conduct experiments with a high sensitivity pump-probe setup with bubble size determined from the Gilmore model for bubble collapse. Measurements take advantage of the scattering properties of laser-induced cavitation bubbles to track their growth and collapse allowing for the determination of their maximum size. In short, a pulsed pump beam is focused into the sample where cavitation bubbles are created according to the mechanisms identified in the theory section. A continuous pump beam is focused to the same spot where it scatters through the bubble interface. Unscattered light is then collected and used to measure bubble dynamics. Pump-probe methods have been used by multiple researchers and shown to be very reliable [73, 20, 9].

#### 3.1 Experimental Setup

We synthesized gold nanospheres using the Turkevich method [74]. Particles of nominal diameter  $50 \pm 4$  nm with 1.2 ellipticity and concentration of  $3.3 \times 10^{10}$  np/mL were mixed with a surfactant (BASF F108 Pluronic) at 20 mg/mL to prevent agglomeration after ablation of stabilizing citrate ions from continually applied pump beam pulses. Nanospheres of this size and shape exhibit resonance at 540 nm (Figure 2.1) however, we utilize 780 nm excitation due to minimal absorption of tissues at this wavelength. We focused 180 fs (FWHM) laser pulses (Spectra Physics Spitfire) into the nanoparticle solution using a back aperture filled 0.95 NA

water-dipping objective lens (Olympus apochromatic 20x) resulting in 751 nm pump and 609 nm probe spot sizes ( $\frac{1}{e^2}$ ). Diffraction limited spot size calculations utilize the standard method outlined by Urey [75]. In this study, only short-lived bubbles of a maximum lifetime of a few microseconds were of concern; thus, 1KHz pulse repetition rates are appropriate to ensure no pulse-to-pulse interactions.

We used a pump-probe scattering technique to measure bubble oscillation created by excitation pulses. Figure 3.1 shows the actual setup with labeling and an overlay of beams paths while Figure 3.2 depicts a simple schematic representation. A collinear spatially filtered (Newport M900, 25  $\mu m$  pinhole) 633 nm HeNe (Uniphase, 21 mW) probe beam scattered through rapidly expanding and collapsing cavitation bubbles. Two dichroic mirrors (DM, CVI 700 nm cutoff) both combine and separate the beams before and after the test chamber, respectfully. Both pump and probe beams were focused through the same objective lens into the nanoparticle solution with the scattered light being collected by a 0.28 NA objective lens (Mitutoya). We then focus the collected and collimated probe light through an iris to further block scattered light before filtering any remaining femtosecond pulsed light (Thorlabs FB780-10) and sampling by 150MHz photodetector (ThorLabs PDA10A). Scattered signals initiate automated data acquisition through a 300MHz digitizer (National Instruments PCI5152) and custom LabView program with a low-frequency trigger filter and recording of trigger initiation times.

The fluid chamber is a custom-machined unit from aluminum stock measuring approximately 3 cm square with three glass coverslip windows. This chamber is held with an xyz translation stage to control precise insertion of the Olympus lens. A peristaltic pump (Welco WPX1) constantly circulated new particles into the focal volume throughout the experiment at an average rate of 15.8 mL/min as measured from timing dyed fluid speeds in a clear tube of known diameter.

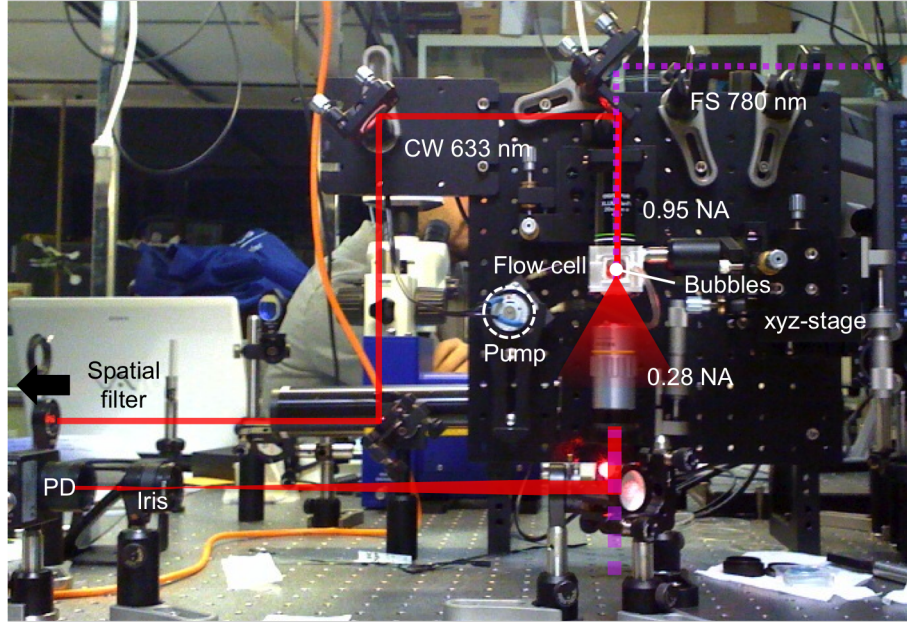


**Figure 3.1:** Actual pump-probe bubbles oscillation measurement system. Colinear CW 633 nm and pulsed 780 nm beams are focused into a sample chamber where the pump beam induced bubble formation and the probe beam scatters through the bubbles. Scattered light is collected, filtered, and sent to a photodetector where signals are sampled by a high-speed digitizer card and initiate automated data acquisition.

We prepared a control sample by removal of gold nanospheres from an identical solution including the pluronic stabilizing agent by centrifuging at 300g for 45 minutes to ensure identical fluid properties as seen by the particles. Our experimental system is capable of discerning minimum bubble lifetime of 25 ns and is limited by HeNe probe beam signal to noise ratio rather than detector noise or risetime.

### 3.2 Particle-Focal Volume Interaction

Due to the Gaussian energy distribution of laser beams, particles at different locations within a focal volume will experience significantly different intensities and will result in significantly different bubble sizes. Each laser pulse may be viewed

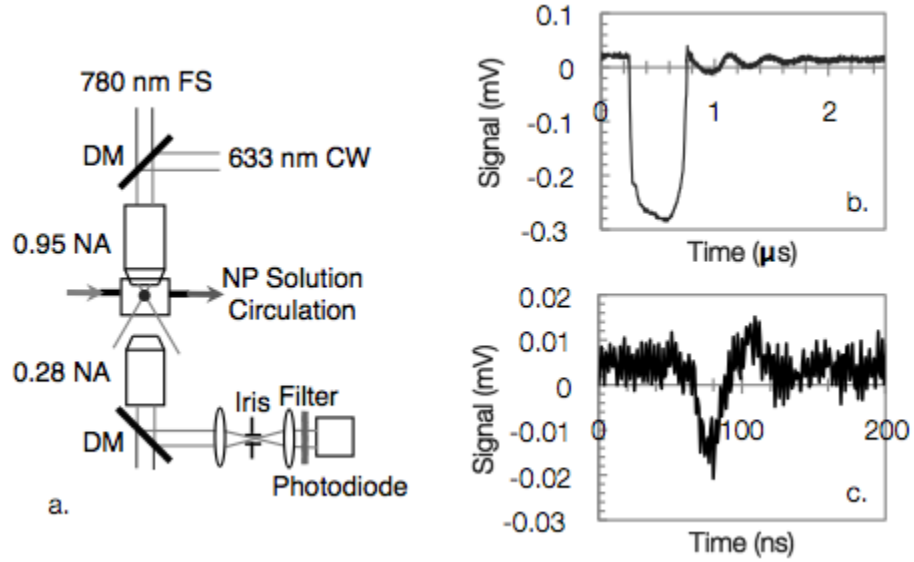


**Figure 3.2:** Schematic of bubbles oscillation measurement system (a) and two typical scattered signals (b) a large bubble showing additional oscillations following the initial bubble collapse and (c) a smaller bubble with a single collapse. Scattered signals are used to initiate automated data acquisition through a digitizer and custom driver program. A small portion of pre-triggered signal is recorded for each bubble to establish a baseline signal value.

as a random sampling of a small volume of the test solution with detected bubble sizes varying with nanoparticle position. Due to the inverse relation between radial location and intensity, the most frequently observed, or most probable, bubble size will occur when particles are at the minimum intensity to induce the smallest detectable bubbles. Conversely, the largest possible bubbles size would occur when a particle is at the exact center of the focal volume and are therefore the least probable occurrence. In fact, the probability of a particle being at any single point in space is zero so that the largest bubble size will never be detected at a given laser energy ( $\bar{E}$ ). Additionally, nanoparticle synthesis and storage result in some amount of clustering of particles. Bubbles initiated from such outliers, though infrequent,

would skew maximum observed bubble sizes. Due to the vanishing probability of particles being at the peak laser intensity and particle clustering it would be wholly inappropriate to correlate largest observed bubble sizes with peak laser intensities for a given average energy. Thus, we cannot explicitly determine cavitation bubble size as a function of applied laser energy with the current experimental setup. However, we may still determine the nanoparticle-mediated reduction in applied energy necessary to induce the smallest-detectable-sized bubble versus water alone. To do so, we measure the time-between detected bubbles and match this to the time-between particles being present in a sphere of an unknown radius. With the radius determined, the local intensity experienced by the particle at this location is given by the beam intensity distribution at its waist [76]

$$I(r) = 0.94 \left( \frac{2\bar{E}}{\pi w_o^2 \tau_p} \right) \exp \left( - \frac{2r^2}{w_o^2} \right), \quad (3.1)$$

where  $w_o$  is  $\frac{1}{e^2}$  spot size. To find the time-between particles being present in a sphere as a function of sphere size we must know the particle number density and particle speed.

To determine the actual speed of particles passing through the focal volume, we performed a simple 3D incompressible flow model in COMSOL Multiphysics. The volume is approximated using a mesh of approximately 10,000 second-order tetrahedral Lagrange elements. No-slip boundary conditions were enforced at all chamber and objective lens surfaces while zero-shear was used at the fluid-air interface. Asymmetric flow patterns result from the pump connection ports orientation, however, this is unimportant when concerned only with the speed of particles traveling through the focal volume (2 mm below objective lens tip). We determine the average focal volume particle speed to be  $\bar{u}_p = 17 \mu\text{m/s}$ . Figure 3.3 shows the finite element velocity field results at the flow cell midplane. Brownian motion of 50 nm particles in water at room temperature based upon Stokes-Einstein diffusion is



negligible when compared with fluid speeds calculated here (details in Appendix I). Fluid speeds induce bubble shifts of nano to pico meters over the bubble lifetimes of interest here and will therefore not effect oscillation time measurements.

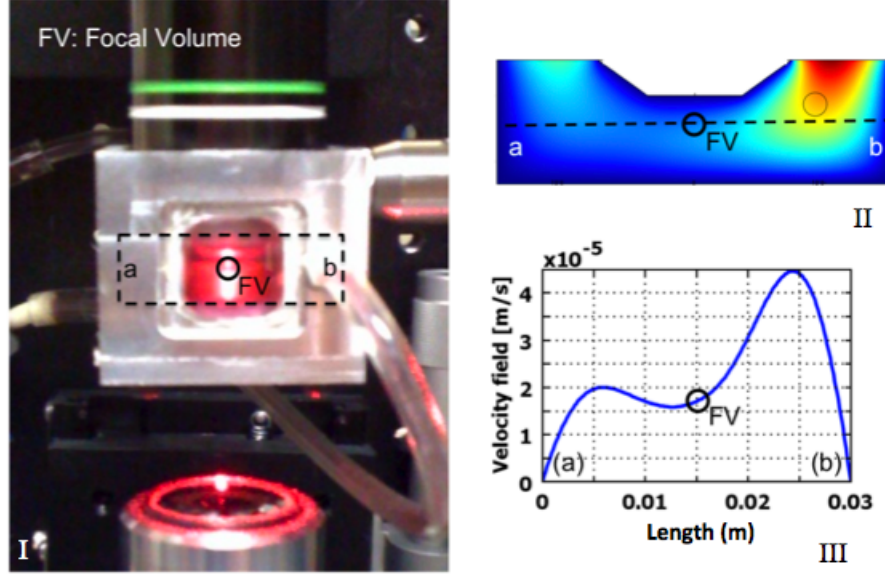


**Figure 3.3:** A picture of the machined flow cell (I), contour plot of the finite element approximation in a plane across the focal volume (II) showing flow asymmetry and (III) a line plot showing the average fluid and nanoparticle velocity in the focal volume. Section a-b spans the midplane of the flow cell.

Using the estimated nanoparticle flow speed and particle absorption cross section we calculate the average time between a particle being present in a spherical focal volumes of given radius,  $r_{fv}$ , using a simple particle kinetics approach describing the collision frequency of particles and our focal volume. That is, the particle speed, process cross-section, and particle concentration,  $n_p$ , completely define the specific process mean-free-path and collision frequency [77].

$$\delta t_c = \frac{\lambda}{\bar{u}_p}, \quad (3.2)$$

where the mean free path a particle has traveled between successive collisions with a stationary focal volume sized sphere,  $\lambda$ , is

$$\lambda = \frac{1}{\pi n_p (r_{eq} + r_{abs})^2} \quad (3.3)$$

Additionally, we must account for the particle dwell time within the focal volume by taking the average path length across a sphere as a function of sphere radius. Given a uniform field of particles entering and traveling through a sphere at random locations, the average distance traversed through the sphere is simply  $\bar{l} = \frac{r_{sphere}}{2}$ . Thus, the average time a particle spends within our focal volume after "colliding" with it is the mean traverse length over the mean particle speed, or

$$\delta t_d = \frac{(r_{eq} + r_{abs})}{2\bar{u}_p}, \quad (3.4)$$

so that the total time-between particles being present in the focal volume is

$$\delta t = \delta t_c - \delta t_d \quad (3.5)$$

In the above discussion we have used the radius of volume equivalent sphere,  $r_{eq}$ , instead of the actual cross-sectional radius,  $r_{fv}$ , due to ellipticity in the actual focal volume. That is, the radius of a sphere of the same total volume as the volume of the actual elliptical focal volume ( $\frac{4}{3}\pi r_{eq}^3 = \frac{4a}{3b}\pi r_{fv}^3$ ).

$$r_{fv} = \left(\frac{a}{b}\right)^{1/3} r_{eq}, \quad (3.6)$$

where the ellipticity ratio ( $a/b$ ) for a focused beam is [8]

$$\frac{a}{b} = \frac{1 - \cos\alpha}{(3 - 2\cos\alpha - \cos 2\alpha)^{1/2}}, \quad (3.7)$$

with solid angle,  $\alpha$ , being a function of the objective lens numerical aperture and medium index of refraction  $\alpha = \sin^{-1}\left(\frac{NA}{n_{water}}\right)$ . Elliptical focal volumes cause higher collision frequencies due to a larger effective collision cross-section. (As an extreme

example, imagine a zero-volumed point versus a zero-volumed plane; the point will have a cross-section of zero while the plane's will be infinite). The true focal volume radius calculated using the above equations may be used with Equation 3.1 to find the threshold intensity for detectable bubble formation.

Times calculated using equation 3.5 may be matches with experimentally measured time between triggers to determine the particle location within the focal volume resulting in the minimum observable bubble size at different energy levels. The focal volume radius gives the bounds of minimum intensity necessary to initiate our observed bubbles with the assumption of a Gaussian beam profile. Thus, we may determine the local intensity around a particle from the average intensity. By setting the calculated local particle intensity to peak intensity and corresponding average intensity, we determine the absolute particle mediated photodisruption threshold reduction. Our procedure is perhaps the only viable method of experimentally determining aqueous suspended nanoparticle photodisruption enhancements. Particle photodisruption enhancements have been determined for gold spheres on substrates by affixing the particles and measuring ablation depths [78, 79]. However, these results are not valid for particles in a fluid suspension because particle near-field enhancement and plasmon resonance change drastically at solid interfaces. Using results generated under particle-on-a-surface conditions would be inappropriate in a biological setting where particles are essentially suspended in fluid.

### 3.3 Data Processing

We must extract bubble oscillation times from thousands of recorded scattered light signals and convert these oscillation times into bubble radii. We automated these analysis by creation of a bubble edge search algorithm and iterative solution of the nonlinear Gilmore model for bubble collapse.

### 3.3.1 Data Reduction

Given the large volume of data acquired with this system, extraction of bubble oscillation times from scattered signals manually is not feasible. We developed an oscillation time extraction script using Matlab. This script functions by first applying a small amount of smoothing, that is, averaging over a translating box of 5 data points. Smoothing is necessary to avoid an excess of local minima in signal due to random HeNe noise. The script takes an overall signal average from the first 5% of signal which contains pre-triggered information to establish a baseline mean signal value and noise range. Based upon the baseline value, the algorithm searches initially for points which are below the noise range and then checks if the data after this continue to descend. Once this point has been identified, the bubble initiation time is found by back-tracking through the noise, that is, the true initiation is assumed to occur at the identified point of descent less the average noise. This step is necessary to avoid artificial shorting of oscillation times due to only being able to identify areas of signal descent outside the noise region.

Essentially, the program searches for points below signal noise with a negative slope for a time approximately equivalent to the risetime of the photodetector. The reverse is applied to find the rising edge of the bubble. Figure 3.4 illustrates the initial signal in green, averaged signal in black, and oscillation time edge points identified by the algorithm with blue circles. This algorithm identifies oscillation times remarkably well as compared to manual measurement. However, due to random electrical signals (for example if a light or appliance is switched on during the experiment) false triggers are initiated which can sometimes fool the script into believing it is a bubble and not random noise. The result is the unfortunate necessity to scan through every signal manually to throw out these bad triggers. Fortunately, bubbles create very unique signals and false triggers are easily identified by eye.

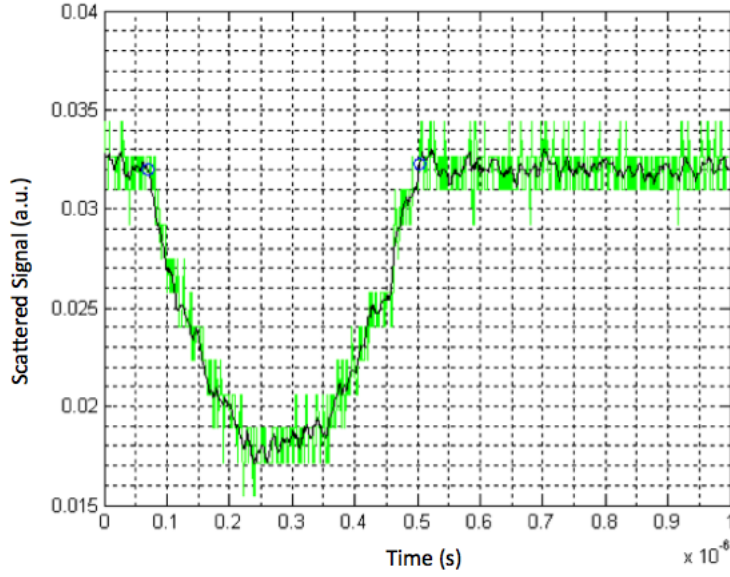


**Figure 3.4:** Example signal of collected light (green line) due to scattering of a laser-induced bubble with averaging (black line) for the identification of the bubble oscillation through the difference of the automatically detected bubble collapse and initiation times (circles).

For large bubbles, forward scattering may pass through the iris 'pinhole' and cause a large signal rise within the first bubble oscillation. These cases are also easily identifiable by inspection and we make use of a slightly modified search algorithm.

We determine errors associated with the edge-find method of identifying bubble oscillation times from the signal noise ( $\pm 0.004$  mV corresponding to approximately 2 ns) and detector risetime (1 ns). The corresponding time error is  $\pm 3.1$  ns. Because of the non-linear relation between bubble size and oscillation time, a static time error does not correlate to a static bubble radius error. Using the Gilmore model, discussed in the next Section, this time error corresponds to a bubble radius error of  $\pm 16$  nm for the smallest bubbles detected (300 nm) and  $\pm 18$  nm for larger bubbles on the order of microns.

### 3.3.2 Gilmore Model of Bubble Expansion & Collapse

We estimate maximum bubble radii using the Gilmore model for bubble expansion and collapse based upon oscillation times extracted from scattered signals. The basic theory and assumptions utilized in its derivation are given in Section 2.2.2. The elegance of the Gilmore model lies in his reduction of the full-field partial differential equations governing compressible flow outside a sphere to a single differential equation for bubble wall velocity. The final nonlinear equation governing only the bubble wall location  $R$ , is given as [18]:

$$\ddot{R} = \left[ -\frac{3}{2}\dot{R}^2 \left(1 - \frac{\dot{R}}{3C}\right) + H \left(1 - \frac{\dot{R}}{C}\right) + \frac{R\dot{H}}{C} \left(1 - \frac{\dot{R}}{C}\right) \right] \left[1 - \frac{\dot{R}}{C}\right]^{-1}, \quad (3.8)$$

where the enthalpy is determined using the thermodynamic relation  $\rho dh = dp$  and assuming isentropic compression of the form

$$\frac{P+B}{P_o+B} = \left(\frac{\rho}{\rho_o}\right)^n, \quad (3.9)$$

yielding

$$H = \frac{n(p_o+B)}{(n-1)\rho_o} \left[ \left(\frac{P+B}{p_o+B}\right)^{\frac{n-1}{n}} - 1 \right], \quad (3.10)$$

and the local speed of sound is

$$C = c_o \left(\frac{P+B}{p_o+B}\right)^{\frac{n-1}{2n}}, \quad (3.11)$$

where the  $o$  subscript indicates ambient conditions,  $P$  is the pressure at the bubble wall, and  $B$  and  $n$  are isentropic compression constants for the medium (for water,  $B \approx 3000$  and  $n \approx 7$ ). The dynamic bubble wall pressure term is a product of the interior vapor pressure ( $p_i$ ), Laplace pressure, and viscous stress resisting bubble wall motion.

$$P = p_i - \frac{2\sigma}{R} - \frac{4\mu\dot{R}}{R} \quad (3.12)$$

where  $\sigma$  is surface tension and  $\mu$  is fluid viscosity. The more commonly used Rayleigh model neglects these terms, which become significant when the Bond number, in terms of bubble wall acceleration, and Reynolds number are not much greater than one, respectively.

Equation 3.8 bares little resemblance to the conservation of mass and momentum equations from which it began. A few highlights of the derivation process are warranted to accept this form without going through the rather lengthy derivation step-by-step. First, the final equation is a result of the integral of conservation of momentum from the bubble wall to infinity. The divergence operator present in the viscous stress term has been replaced through the use of continuity. All density and pressure variations have been absorbed into either the sonic velocity relation  $c^2 = \frac{dp}{d\rho}$  or the enthalpy term through  $h(p) = \int_{P_o}^P \frac{dp}{\rho}$ . After separating density variations and integrating, the convective term becomes the first term on the RHS with  $\dot{R}^2$ . Perhaps the most peculiar features of Gilmore model arise from the application of the quasi-acoustic approximation used by Kirkwood and Bethe to explain wave propagation from underwater explosions [80]. The unsteady term in momentum conservation may be replaced with the gradient of the velocity potential utilizing the condition of irrotational flow. Spherically diverging sounds waves, given by the potential function, will propagate outward with variable velocity of  $(c + u)$  at liquid velocities where incompressibility breaks down. Therefore, all terms equal to the potential must also propagate at this speed leading to the so-called quasi-acoustic approximation that the quantity  $r(h + u^2/2)$  propagates at the variable velocity  $(c+u)$ .

While somewhat vague, the above outlined treatment summarizes crucial steps and assumptions utilized by Gilmore. For all details of its derivation, the curious reader is encouraged to read the full 1952 Office of Naval Resrach technical

report [18].

We solve equation 3.8 using the built-in 4th order Runge-Kutta solver in Matlab nested in an iterative method based on matching of observed bubble collapse time with maximum bubble radius at zero bubble wall velocity (inception of collapse). We have assumed a static interior bubble pressure equal to the vapor pressure of water. This approximation is incorrect but results in only a slight over-prediction of bubble size. Others have correlated a dynamic interior pressure based upon images of large induced plasma and approximate corresponding vaporized volume [20]. For the size of bubbles of interest here, this method is not possible. To quantify the error caused by this static interior pressure, we look at the dynamic pressure terms used in [20] and use properties yielding the maximum possible bubble rebound (Figure 3.5). Cavitation bubbles will never rebound to the same size as the initial expansion so our test case is unrealistically severe. We see the maximum (and unrealistically large) result of neglecting dynamic interior bubble pressure is a 3% over prediction in the maximum bubble radius. Additionally, smaller bubbles never exhibit a rebound sequence thus, for small bubbles, this bias error is vanishing.

Our experimental setup, data acquisition, and data processing system allow for accumulation of large amounts of bubble size data at varying pump laser energies with minimal human assistance. We take an average of 100 measurements for each of over 40 different energy levels resulting in a total of over 3000 data points to establish nanoparticle mediated bubble size ranges below the formation threshold of water alone. For lower energies, the frequency of bubble creation is drastically reduced due to the decreasing probability of nanoparticles being at higher intensity regions within the focal volume during the pump pulse. Consequently, only 30 measurements are made at the lowest energy level. Rather than attempt to identify threshold reductions by waiting for a theoretically impossible condition



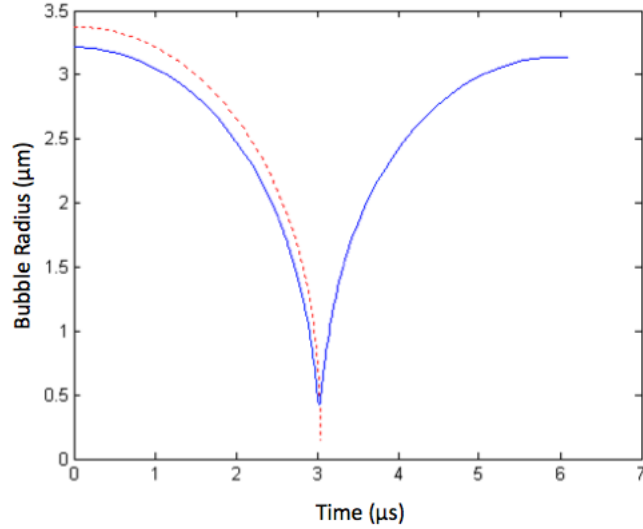


**Figure 3.5:** Effects of dynamic interior bubble pressure on the results of the Gilmore model for bubble collapse. The solid line represents conditions for dynamic interior bubble pressure which result in a complete bubble rebound while the dashed line indicates a constant interior pressure equal to the vapor pressure at ambient conditions

(particle being at exact center of focal volume during the pulse), we perform 1000 measurements at four near-nanoparticle bubble threshold energy levels to establish a statistical average time between triggering events allowing us to determine the true particle threshold reduction as outlined in Section 3.2. Such a large volume of data is necessary to determine both bubble creation energy threshold reduction and bubble size variability due to random nanoparticle location within the ellipsoidal focal volume. While the minimum detectable bubble sizes by this system is not the true minimum bubble size created by femtosecond pulses, it can be used for nanoparticle enhancement determinations by comparing the threshold reduction for our minimum detectable size in solutions with and without nanoparticles.

## Chapter 4

### Theoretical Modeling and Numerical Analysis

We perform a series of numerical simulations of nanoparticle-light interactions to explain our observed experimental results and to determine mechanisms, regimes, and optimization of photodisruption. We utilize and develop models from the pre-existing classical two-temperature equations for electron-phonon interaction and photoemission processes. From the two-temperature model describing non-equilibrium electrons and phonons, we identify significant non-dimensional groups and generalize results for implementation to different particle geometries and materials along with different laser parameters.

#### 4.1 Particle Heating

We used the classical hyperbolic two-temperature model (TTM) for laser heating of a metal to calculate the gold particle electron and lattice heating. Derivation of this model from the Boltzmann transport equation is given in [56] and is not reproduced here. For the purpose of determining electron donation and the onset of electrostatic particle ablation, we must first establish if lumping of electron temperatures across the particle is appropriate. To this end, we perform a full two-dimensional TTM simulation. As will be shown, the assumption of uniform electron temperatures are appropriate for laser pulses studied here. We next proceed to a one-dimensional model including interfacial conduction with the surrounding media to examine damage regimes and thresholds. For this section, a pre-existing and

validated FORTRAN routine developed by Dr. Ozgur Ekici is modified to allow the calculation of a large range of test parameters [81]. We next develop critical electron temperatures and conditions necessary to induce the ablation for a single particle.

#### 4.1.1 Two-Dimensional Electron and Phonon Heating

Contrary to other similar treatments for thin film heating [54] and nanosphere heating [82] which assume uniform temperature distributions, the full TTM equations may be necessary when concerned with electron temperature distributions during laser heating. When only interested in predicting particle melting or heat conduction from the particle surface to induce medium boiling or protein denaturation, lumping electron temperatures is fully justified. However, our calculations of particle ablation and electron emission (Section 4.2) necessitate we establish some validity range for lumping electron temperatures. Simplified 1D formulations ignore electron heat conduction by assuming either out-of-plane or angular heat transfer is zero. In addition, 1D spherical simulations assume uniform laser irradiation across the entire sphere surface. Here, we consider 2D axisymmetric electron conduction when a particle is exposed to a more realistic laser intensity distribution across the particle surface. Equations 4.1 and 4.3 describe electron-phonon coupling and individual electron and lattice conduction while Eqs. 4.2 and 4.4 relate conduction to temperature gradients and relaxation times.

$$C_e \frac{\partial T_e}{\partial t} = -\nabla \cdot \vec{Q}_e - g(T_e - T_p) + S, \quad (4.1)$$

$$\tau_e \frac{\partial \vec{Q}_e}{\partial t} + \vec{Q}_e = -k_e \nabla T_e, \quad (4.2)$$

$$C_p \frac{\partial T_p}{\partial t} = -\nabla \cdot \vec{Q}_p - g(T_e - T_p), \quad (4.3)$$

$$\tau_p \frac{\partial \vec{Q}_p}{\partial t} + \vec{Q}_p = -k_p \nabla T_p, \quad (4.4)$$

where  $T$  is the subsystem temperature,  $Q$  the heat flux vector,  $C$  the heat capacity, and subscripts  $e$  and  $p$  indicate electron and phonon properties, respectively. The thermal conductivity ( $k_e$ ), relaxation time of electrons ( $\tau_e$ ), and the electron phonon coupling coefficient, ( $g$ ), used in this study all are temperature dependent semi-empirical fits[83].

$$k_e = \chi \frac{\left[(T_e/T_p)^2 + 0.16\right]^{5/4} \left[(T_e/T_p)^2 + 0.44\right] (T_e/T_p)}{\left[(T_e/T_p)^2 + 0.092\right]^{1/2} \left[(T_e/T_p)^2 + \eta(T_p/T_e)\right]}, \quad (4.5)$$

$$\tau_e = (A_e T_e^2 + B_p T_p)^{-1}, \quad (4.6)$$

$$g = g_{rt} \left[ \frac{A_e}{B_p} (T_e + T_p) + 1 \right], \quad (4.7)$$

where  $g_{rt}$ ,  $A_e$ ,  $B_p$ ,  $\chi$ , and  $\eta$  are material constants (See Table 4.1).

The electron subsystem Eq. 4.1 can be explained as the rate of change of electron energy is equal to the net out-flow of energy via electron-electron conduction less energy transferred to the phonon subsystem via electron-phonon relaxation plus laser heating source,  $S$ . The phonon subsystem Eq. 4.3 can be explained in a similar manner except the source term is the sink of the electron subsystem. Conduction to the surrounding medium would manifest itself as only a boundary condition; this interaction is examined in the next section. The hyperbolic nature of the process is seen in Eqs. 4.2 and 4.4 where heat transfer is not instantaneous within each subsystem as would be assumed with parabolic Fourier-type conduction.

To account for spatial variation of laser heating, we modify the commonly used source term equation to include 2D effects [56]. Assuming incident plane waves and neglecting plasmon oscillations, the particle heating should drop to zero at its zero-volume edges as opposed to a uniform source term for all angular locations. The modified source term as a function of radial position ( $r$ ), angular position ( $\theta$ ),

and time (t) becomes

$$s(r, \theta, t) = Q_{abs} \frac{(r_o - r \sin \theta)}{r_o} \sqrt{\frac{4 \ln 2}{\pi}} \frac{F}{\delta \tau_p} \exp \left[ \frac{(r_o^2 - r^2 \sin^2(\theta))^{1/2} - r \cos \theta}{\delta} - 4 \ln 2 \left( \frac{t - 2\tau_p}{\tau_p} \right)^2 \right], \quad (4.8)$$

where  $Q_{abs}$  is the particle wavelength dependent absorption efficiency,  $r_o$  is the particle radius,  $F$  is the local average fluence,  $\delta$  is the optical penetration depth of photons in gold (where the intensity amplitude is decreased by a factor  $e$ ), and  $\tau_p$  is pulse duration (FWHM). Because our purpose in this section is only to determine the magnitude of electron temperature gradients, we take  $Q_{abs}$  to be constant for all size particles.

Equation 4.8 is essentially a projection of planar fluence onto a curved surface with a depth decay based upon the optical penetration depth of photons in gold. This assumption is valid for the beam waist (where wavefront curvature goes to infinity) and without any coherent electron motion. Particles within the focal volume experience converging rays above the focal plane and diverging rays below so that this treatment is slightly inaccurate. Additionally, surface plasmon resonance may result in a more uniform absorption due to coherent electron motion across the particle surface. Given that we are only concerned with the validity of a lumped electron temperature assumption, this treatment of the source term is actually a worst-case scenario. Despite these short falls, the current source formulation is more applicable for sphere heating than those previously used in [56]. An example of the resulting source term distribution is given in Figure 4.1 overlaid on the grid discretization.

We use a modified MacCormack scheme to advance the solution in time with predictor and corrector formulations given below. The variable temperatures and heat fluxes are arranged into vectors allowing for a more cohesive representation

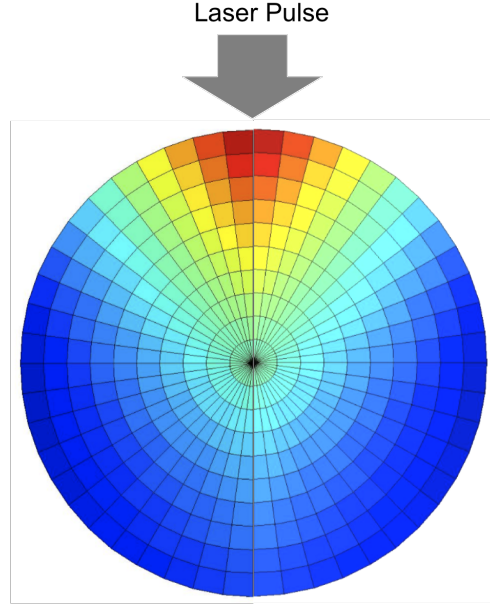


**Figure 4.1:** Normalized source term for electron heating of a nanoparticle (D=25 nm shown here) and grid points using equation 4.8 for 2D axisymmetric case. For the actual simulation, only half the area is used.

and coding.

*Predictor:*

$$\hat{U}_{i,j}^{n+1} = U_{i,j}^n - \frac{\Delta t}{2\Delta r}(E_{i+1,j}^n - E_{i-1,j}^n) - \frac{\Delta t}{2\Delta\theta}(F_{i,j+1}^n - F_{i,j-1}^n) + \Delta t(S_1 + S_2) \quad (4.9)$$

*Corrector:*

$$U_{i,j}^{n+1} = \frac{1}{2} \left[ U_{i,j}^n + \hat{U}_{i,j}^{n+1} - \frac{\Delta t}{2\Delta r}(\hat{E}_{i+1,j}^{n+1} - \hat{E}_{i-1,j}^{n+1}) - \frac{\Delta t}{2\Delta\theta}(\hat{F}_{i,j+1}^{n+1} - \hat{F}_{i,j-1}^{n+1}) + \Delta t(S_1 + S_2) \right] \quad (4.10)$$

where

$$\vec{U} = \begin{bmatrix} T_e \\ Q_e^r \\ Q_e^\theta \\ T_p \\ Q_p^r \\ Q_p^\theta \end{bmatrix} \quad \vec{E} = \begin{bmatrix} Q_e^r/C_e \\ T_e k_e/\tau_e \\ 0 \\ Q_p^r/C_p \\ T_p k_p/\tau_p \\ 0 \end{bmatrix} \quad \vec{F} = \begin{bmatrix} Q_e^\theta/C_e r \\ 0 \\ T_e k_e/\tau_e r \\ Q_p^\theta/C_p r \\ 0 \\ T_p k_p/\tau_p r \end{bmatrix} \quad (4.11)$$

$$\vec{S}_1 = \begin{bmatrix} \frac{s}{C_e} - \frac{g(T_e - T_p)}{C_e} \\ 0 \\ 0 \\ \frac{g(T_e - T_p)}{C_p} \\ 0 \\ 0 \end{bmatrix} \quad \vec{S}_2 = \begin{bmatrix} \frac{-2Q_r^e}{C_e r} \\ -Q_r^e/\tau_e \\ -Q_\theta^e/\tau_e \\ \frac{-2Q_r^p}{C_p r} \\ -Q_r^p/\tau_p \\ -Q_\theta^p/\tau_p \end{bmatrix} \quad (4.12)$$

The classical scheme would include forward and backward differencing with swapping of these directions within each predictor and corrector step as well as in the entire time integration sequence to maintain stability. For this hyperbolic heat transfer formulation, these steps are replaced by a single central difference scheme for spatial derivatives.

We assume 2D axisymmetric spherical heating about the axis of laser propagation. Heat transfer to surrounding medium is negligible during the rapid heating process in the time scales of several femtoseconds for electron-electron equilibration so that the 2D half circle geometry is insulated on all sides. Experimentally measured heat transfer rates from a heated nanosphere to surrounding water verify this assumption [84]. The center of the sphere requires special attention due to the artificial singularity resulting from spherical formulation [85]. Radial derivatives at the ring of grid points immediately adjacent to the center are performed using  $(i + 2, j)$  and  $(1, \pi - j)$  grid points, that is, by using a larger stencil and symmetry to avoid including singular values in temperature calculations. To prevent a non-physical multivalued temperature at the single center location, we use an average of all immediately adjacent grid point values. Smoothing is necessary to avoid small

numerical noise from propagating into instability, to this end, we perform four-point neighbor stencil for averaging after each time step. Radial grid point locations are discretized by  $\Delta r = R/10$  and angular locations by  $\Delta\theta = \pi/24$ . We find a numerically stable time step of  $\Delta t$  to be  $6 \times 10^{-17}$  s.

We examine cases of different pulse duration and particle size to determine the extent on non-equilibrium electron heating during applied pulses. Values used in these calculations are given in Table 4.1 as follows [56, 54, 86, 87, 81].

Table 4.1: Constants and material properties

$g_{rt}$	$2.2 \times 10^{17}$	$[Wm^{-3}K^{-1}]$
$A_e$	$1.2 \times 10^7$	$[K^{-2}s^{-1}]$
$B_p$	$1.23 \times 10^{11}$	$[K^{-1}s^{-1}]$
$\chi$	353	$[Wm^{-1}K^{-1}]$
$\eta$	0.16	
$C_p$	$1.5 \times 10^6$	$[Jm^{-3}K^{-1}]$
$C_w$	4.18	$[kJkg^{-1}K^{-1}]$
$\rho_{Au}$	19,300	$[kgm^{-3}]$
$k_p$	315	$[Wm^{-1}K^{-1}]$
$k_{water}$	0.61	$[Wm^{-1}K^{-1}]$
$G$	$105 \times 10^6$	$[Wm^{-2}K^{-1}]$
$\delta$	15	$[nm]$
$T_o$	300	$[K]$
$T_f$	64,130	$[K]$

#### 4.1.2 One-Dimensional Particle and Medium Heating

The details of the above 2D TTM results are presented and discussed in Section 5.1 however, the main result can be summarized as: for gold particles, lumped electron temperatures are valid for pulse as short as 10 fs for particles as large as 75 nm radius. Subject to these constraints, we cast the general TTM into a naturally-scaled, non-dimensional form to reveal its underlying physical parameters. Our goal is to identify non-dimensional groups which generalize TTM and surrounding medium heating solutions for a wide range of particle-laser cases and applications.



To produce simple, yet relevant, non-dimensional groups, we turn to a simpler form of the TTM than used in the previous section. This more commonly used set of equations assumes no temperature gradients across the particle and utilizes a top-hat laser heating source term. Energy deposition into the particle is assumed to be uniform both spatially and temporally for the  $\frac{1}{e^2}$  pulse duration. Spherically symmetric heat diffusion is used to model energy removal by the surrounding medium [81].

$$C_e \frac{dT_e}{dt} = g(T_p - T_e) + \frac{Q_{abs} A_c F}{V_p \tau_p} \quad (4.13)$$

$$C_p \frac{dT_p}{dt} = g(T_e - T_p) - \frac{A_s G}{V_p} (T_p - T_{w,s}) \quad (4.14)$$

$$\frac{\partial T_w}{\partial t} = \frac{\alpha}{r^2} \frac{\partial}{\partial r} \left( r^2 \frac{\partial T_w}{\partial r} \right) \quad (4.15)$$

where  $A_s$  indicates the particle surface area,  $A_c$  indicates the particle cross-section area,  $T_{w,s}$  is the water temperature at the particle surface,  $G$  is the gold-water interfacial conductance and  $\alpha$  is the thermal diffusivity of water. For Debye length scale-contact areas, such as our particle-water interface, there will be a discontinuous temperature "jump" across the interface due to restriction of interacting phonon frequency [88], hence,  $G$  is the effective conductance with this discontinuity (Table 4.1).

In scaling Eqs. 4.13, 4.14, and 4.15, the only assumed argument is the electron equation time scales naturally with the pulse duration. This is different than in [89] where Nolte and co-workers assumed this time scaled with the electron-phonon relaxation time. Scaling by electron-phonon relaxation times produce uncollapsed scaled temperatures and does not properly indicate the non-dimensional groups that are important over all ranges of fluence, pulse durations, and particle geometries of interest. Since the electron-phonon relaxation time is a function of electron specific heat which is a function of the electron temperature ( $C_e = 70T_e$

for gold below the Fermi temperature [56]), it thus becomes inconsistent over large ranges.

By transforming Eq. 4.13 with time normalized by pulse duration, previously unknown electron and phonon temperature scaling as well as appropriate non-dimensional groups become apparent. These additional scalings are subsequently passed to the phonon system Eq. 4.14 where the surface water characteristic temperature and time scale as well as an additional non-dimensional group are identified. The transformed form of Eq. 4.13 is:

$$\left(\frac{T_{e,c} - T_o}{T_o}\theta_e + 1\right)\frac{d\theta_e}{d\zeta} = \frac{\tau_p g}{C_e^o} \left(\frac{T_{p,c} - T_o}{T_{e,c} - T_o}\theta_p - \theta_e\right) + \frac{Q_{abs} A_c F}{V_p C_e^o} \frac{T_o}{T_{e,c} - T_o}, \quad (4.16)$$

where  $T_{c,\chi}$  are the unknown characteristic temperatures for each subsystem ( $\chi = e, p, w$ ) stemming from the assumed scaled form  $\theta_\chi = \frac{T_\chi - T_o}{T_{c,\chi} - T_o}$  and  $\zeta = t/t_{e,c}$ . The last term on the RHS reveals the characteristic electron system temperature,  $T_{c,e} = \frac{Q_{abs} A_c F}{V_p C_e^o} + T_o$ , by setting equal to unity. Substitution of this temperature yields

$$\left(\frac{Q_{abs} A_c F}{V_p C_e^o T_o}\theta_e + 1\right)\frac{d\theta_e}{d\zeta} = \frac{\tau_p g V_p}{Q_{abs} A_c F} (T_{p,c} - T_o)\theta_p - \frac{\tau_p g}{C_e^o}\theta_e + 1, \quad (4.17)$$

From the first term on the LHS and the second term on the RHS, we identify non-dimensional groups,  $\beta = \frac{Q_{abs} A_c F}{C_e^o V T_o}$  and  $\gamma = \frac{g \tau_p}{C_e^o}$ , respectively. The first term on the RHS is used to solve for the characteristic phonon temperature,  $T_{c,p} = \frac{Q_{abs} A_c F}{\tau_p g V_p} + T_o$ . Transforming the phonon subsystem Eq. 4.14 according to the above arguments and a yet to be determined characteristic time scale,  $t_{p,c}$ , yields

$$\frac{d\theta_p}{d\xi} = \frac{g t_{p,c}}{C_p} (\gamma \theta_e - \theta_p) + \frac{3 G t_{p,c}}{r_o C_p} \left[ \theta_p - \frac{T_{w,c} - T_o}{\beta T_o} \gamma \theta_w \right] \quad (4.18)$$

where  $\xi = t/t_{p,c}$ . From the first term on the RHS, we find  $t_{p,c} = \frac{C_p}{g}$  and from the last term on the RHS, we identify our third non-dimensional group,  $\epsilon = \frac{3G}{r_o g}$ . The characteristic time scale for the heat diffusion equation is given by the Fourier number and the particle radius.

The transformed and scaled form of equations 4.1 and 4.3 with the lumped assumption of no flux  $\vec{Q}_{e,p} = 0$  and the inclusion of spherical heat diffusion in to the surrounding medium are as follows.

$$(\beta\theta_e + 1)\frac{d\theta_e}{d\xi} = \theta_p - \gamma\theta_e + 1 \quad (4.19)$$

$$\frac{d\theta_p}{d\xi} = \gamma\theta_e + (\epsilon - 1)\theta_p - \theta_w \quad (4.20)$$

$$\frac{\partial\theta_w}{\partial F_o} = \frac{1}{R^2} \frac{\partial}{\partial R} \left( R^2 \frac{\partial\theta_w}{\partial R} \right) \quad (4.21)$$

with the non-dimensional temperatures:

$$\theta_\chi = \frac{T_\chi - T_o}{T_{\chi,c} - T_o} \quad \text{where } \chi = e, p, w \quad (4.22)$$

given by the characteristic temperatures:

$$T_{c,e} = (\beta + 1)T_o \quad T_{c,p} = \left(\frac{\beta}{\gamma} + 1\right)T_o \quad T_{c,w} = \left(\frac{\beta}{\gamma\epsilon} + 1\right)T_o \quad (4.23)$$

non-dimensional times:

$$\zeta = \frac{t}{\tau_p} \quad \xi = \frac{tg}{C_p} \quad F_o = \frac{\alpha t}{r_o^2} \quad (4.24)$$

and non-dimensional parameters:

$$\beta = \frac{Q_{abs} A_c F}{C_e^o V T_o} \quad \gamma = \frac{g\tau_p}{C_e^o} \quad \epsilon = \frac{3G}{r_o g} \quad (4.25)$$

where  $C_e^o$  is the initial electron specific heat,  $A_c$  and  $V$  are the physical particle cross section and volume, and  $G$  is the interfacial conductance of the particle to surrounding medium which accounts for contact resistance between the small particles and surrounding medium [84]. Note the electron specific heat dependence on electron temperature manifests itself as a non-linearity in the electron subsystem equation 4.19 which is significant when  $\beta \approx 1$  or greater, an imbedded fact that is not clear in the unscaled version. The process may seem a bit peculiar given the "flow" of scaling arguments from the electron temperature equation to subsequent equations, however, we will show the success of this method in Chapter 5. We next interpret the physical significance of the  $\gamma, \beta$ , and  $\epsilon$  non-dimensional groups and later demonstrate these meanings with numerical results.

The  $\beta$  parameter represents the ratio of energy transferred to the electron subsystem versus its initial energy; it is simply a scaled absorbed energy term. However, as previously mentioned,  $\beta$  of any significant value induce a nonlinearity in the system and modify the electron temperature behavior with respect to the electron energy transfer parameter. Increasing electron specific heat values with temperature are responsible for this behavior modification as increased absorbed energies cause lower electron temperature increases and lower energy transfer rates to the lattice due to smaller  $\delta T_{e-p}$  values. Though not included in scaling of the TTM, the lattice specific heat is also a function of lattice temperature but much more weakly; we neglected this dependence in scaling and discuss the consequences with other results from this model in Chapter 5.

The  $\gamma$  group is a ratio of energy transfer to the phonons versus stored in the electrons; it represents the rate of energy lost to phonons to the energy deposited in the electron subsystem and will thus be referred to as the electron energy transfer parameter. At  $\gamma = 1$ , energy is removed as rapidly as it is deposited. For cases

where  $\gamma > 1$ , the two systems will rapidly reach equilibrium after the laser pulse ends while for  $\gamma < 1$ , we can expect elevated electron temperatures to be maintained for some time. However, as we show in Chapter 5, these general guidelines are only true when  $\beta \leq 1$  after which  $C_e$  changes significantly. The  $\gamma$  value distinguishing the two behavior regimes becomes a function of  $\beta$ .

The  $\epsilon$  group is the ratio of energy removed via conduction to the surrounding medium versus energy transferred to the lattice via electron-phonon coupling. The particle radius,  $r_o$ , may be extended to particles other than spheres (rods, pyramids, shells, etc.) using a characteristic length scale of  $L_c = \frac{V}{A_s}$  where  $A_s$  is the particle surface area. The non-dimensional group  $\epsilon$  would then become  $\frac{G}{gL_c}$  though we must still perform calculations to confirm the validity of this generalization to different particle geometries. The latter form bares a striking resemblance to the Biot number ( $\frac{hL_c}{k}$ ) commonly used in heat transfer analysis to neglect either convection or conduction. Indeed, the  $\epsilon$  group can be viewed as a modified Biot number where instead of being concerned with the validity of lattice temperature lumping we are concerned with the validity of lumping electron-phonon temperatures with respect to surface conduction. Thus, we shall refer to  $\epsilon$  as the two-temperature Biot number. When the two-temperature and lattice Biot numbers ( $\frac{GL_c}{k_{Au}}$ ) and are less than 1, we can neglect all electron heating effects and lump the lattice temperatures.

We ran 2500 test cases with varying combinations of these three non-dimensional groups to accommodate typical particle size ranges and very large ranges of laser fluence, particle absorption, and pulse duration combinations. We modified a previously validated FORTRAN routine, written by Dr. Ozgur Ekici, to maintain numerical stability over a long pulse durations [81]. Additionally, we used a Matlab wrapper script to prepare test parameter arrays, call the modified FORTRAN routine, and extract and organize solution data of interest. As opposed to the constant

lattice specific heat used in the 2D treatment of Section 4.1.1, this code utilizes a fifth-order polynomial fit which is very weakly varying over all temperature below the melting point of gold. Chapter 5 summarizes results of these calculations. Solutions result in four-dimensional surfaces of scaled temperatures being functions of the identified non-dimensional groups. These results are valid over all potential applications, ranging from imaging to photodisruption using lasers with pulse durations from 10 fs to 10 ns. We create continuous fits to these 4D surfaces to provide general equations and eliminate the need to perform tedious simulations for specific cases. The procedure of fitting is to identify regions of log-log linearity and join the transitions with arctangent 'switch' functions of the form

$$switch = A \arctan \left( w(\chi - c) \right) + l \quad (4.26)$$

where  $A$  is the transition weight,  $w$  is the width of the transition,  $c$  is the center of transition, and  $l$  is the lift. Note this switch function is essentially a smoothed heavy-side step function. Indeed as  $w$  approaches zero, the function becomes a discontinuous step. Functional fits are given in the results section as well.

With this set of universal equations, we can determine at what parameter combinations will the system lead to medium boiling, particle melting, and particle evaporation. However, as we have described in the theory section, when electrons are excited to sufficiently high temperatures, the probability of emission from the particle surface becomes significant and can lead to electron seeding and electrostatic ablation. We examine these two damage regimes next.

## 4.2 Electrostatic Ablation of Particles

Understanding the ablation and emission of electrons from particles is crucial for predicting photodisruption using femtosecond-pulses. For the purpose of

imaging, we must select laser conditions so that not only does the particle not melt, but also not ablate nor emit significant electrons to cause formation of free radicals or seed optical breakdown of the surrounding medium. However, for photodisruption, the latter mechanisms are desirable. A cohesive theory to predict ablation and electron emission from short-pulse irradiated particles has not yet been proposed. However, laser-irradiated thin-film metal surface current density has been successfully described as a combination of thermionic and multiphoton-assisted electron emission comprising the generalized Fowler-Dubridge theory of photoemission (GFD)[60, 61, 58, 90, 91]. Thermionic emission occurs when electrons arriving at the metal surface have velocity components oriented normal to the surface exceed the work function of the material. Thus, thermionic emission is solely due to electron temperature. Multiphoton-assisted emission may occur if surface conduction band electrons absorb one or more photons to exceed the barrier height and be emitted. That is, electrons arriving at the metal surface, without sufficient kinetic energy oriented normal to the interface, near-simultaneously absorb  $n$ -photons to overcome the material potential barrier.

We must briefly distinguish between the generalized Fowler-DuBridge theory of photoemission used here and the alternate Fowler-Nordeim theory of field emission. Fowler-Nordeim theory describes the emission of electrons due to very intense or very low frequency fields "deforming" the atomic potential barrier so that conduction band electrons can tunnel through the distorted barrier. Thus, the distinction is tantamount to the description of MPI and tunneling ionization of dielectric materials presented in Section 2.1. The dimensionless parameter introduced by Anisimov and co-workers indicates which process will be dominant [90].

$$\Gamma = 2m\Phi\left(\frac{\omega}{eE_{\perp}}\right)^2 \quad (4.27)$$

where  $\Phi$  is the material work function (4.25eV for Au),  $e$  the elementary electron charge,  $m$  the electron mass,  $\omega$  the incident light frequency and,  $E_{\perp}$  the electric field component normal to the surface. If  $\Gamma \ll 1$  Fowler-Nordeim type emission will be dominant; if  $\Gamma \gg 1$  Fowler-DuBridge type emission will be dominant. Eq. 4.27 shows tunneling will only occur at very high field strengths or very low frequencies. Individual photon energies are small at low frequencies, thus, multiphoton-assisted processes would require an improbably high number of photons to be simultaneously absorbed. However, high fields will still interact with conduction band electrons via tunneling. For our case of 780 nm light, fields of  $\approx 3\text{GV/m}$  would be necessary to consider Fowler-Nordeim emission, well above anything we consider here.

The original Fowler-DuBridge theory incompassed only thermionic ( $n=0$ ) and single photon ( $n=1$ ) absorption processes [60]. Bechtel *et al.* generalized the Fowler-DuBridge theory of photoemission current density,  $\vec{J}(r, t)$ , to incorporate all orders of emission processes as a simple expansion with activation energy being a function of electron temperature, material work function, and multiphoton process order [61].

$$\vec{J}(\vec{r}, t) = \sum_{n=0}^{\infty} \vec{J}_n(\vec{r}, t) \quad (4.28)$$

where

$$\vec{J}_n(\vec{r}, t) = a_n (e/h\nu)^n A I_o(\vec{r}, t)^n (1 - R)^n T_e(\vec{r}, t)^2 \dot{F} \left[ \frac{nh\nu - \Phi}{k_B T_e(\vec{r}, t)} \right] \quad (4.29)$$

and  $\dot{F}$  indicates the Fowler function

$$\dot{F}(\chi) = \sum_{j=0}^{\infty} \frac{(-1)^{(j-1)}}{j^2} e^{j\chi} \quad (4.30)$$

where  $R$  is the surface reflectivity,  $A_o$  is the theoretical Richardson coefficient ( $120\text{A/cm}^2\text{K}^2$ ),  $(h\nu)$  is the laser photon energy,  $k_B$  is Boltzmann's constant,  $I$  is the incident irradiation, and  $a_n$  is a constant, usually experimentally determined. The



index  $n$  indicates the photon interaction order of the process;  $n = 0$  for thermionic emission,  $n = 1$  for single photon promotion and so on. Note that we do not actually compute Fowler function values due to the costly nature of its computation, instead we interpolate values provided by Bechtel [61]. The rather peculiar Fowler function is a result of the integral of Fermi-Dirac energy distribution over all electron energies.

Current density from equation 4.28 may be used to find electron flux from the particle surface and thus serves as boundary condition in species momentum and energy conservation equations as discussed in the next section. For now, we will just use this term to find critical electron temperatures to induce particle ablation.

For our 780 nm wavelength light and gold material, multiphoton emission is a three photon process, that is, the energy necessary to exceed the 4.25 eV work function for gold may only be achieved by the energy of three absorbed 780 nm photons of 1.59 eV energy. The third-order effect was confirmed by Logothetis and Hartman [58] up to powers of  $\approx 1.4 MW/cm^2$ ; at higher energies, electron yield shifted to a thermionic dominated process. Thus, we are only concerned with the  $n = 0$  and  $n = 3$  terms. Higher order multiphoton processes are possible but occur at a negligible rate. Logothetis and Hartman additionally determined the empirical 3-photon current cross section coefficient,  $c$ , value to be  $1 \times 10^{-7} (A/cm^2)/(MW/cm^2)^3$  by monitoring current induced in thin Au films by high power laser pulses [58]. Included in  $c$  is the effects of electron escape probability, escape depth, and energy gain. The expression  $\frac{2k_B^2}{(3h\nu - \phi)^2}$  is used by Bulgakova *et al* [59] for  $(e/h\nu)^3$  in  $J_3$  so that this  $c$  constant may be used instead of  $a_3$  in Eq. 4.29 yielding

$$J_3 = c \frac{2(K_B T_e)^2}{(3h\nu - e\Phi)^2} \dot{F} \left( \frac{3h\nu - e\Phi}{k_B T_e} \right) (1 - R)^3 I_o^3 \quad (4.31)$$

Equation 4.31 is a direct result of equated current density of the empirical form  $J = cI^3$  containing the experimentally determined current cross-section coefficient

to the predicted current density from the Fowler-DuBridge theory of Eqs. 4.28 and 4.29.

To include near-field effects of plasmonic nanoparticles in the Fowler-DuBridge multiphoton emission theory we use a modified typical Gaussian laser intensity function.

$$I(t) = Q_{NF} \frac{2F}{\tau_p} \sqrt{\frac{\ln 2}{\pi}} \exp \left[ -4 \ln 2 \left( \frac{t}{\tau_p} \right)^2 \right], \quad (4.32)$$

where  $Q_{NF} = \frac{I_{NF}}{I_{incident}}$  is the near field enhancement of the incident laser intensity. The near-field intensity scales with the magnitude of the Poynting vector  $S$  where  $|\vec{S}| = |\vec{E} \times \vec{H}|$ ; thus,  $I_{NF}$  is calculated from the magnitude of the Poynting vector [92]. Others [93, 94] have used the magnitude of only the real portion of the Poynting vector (where the imaginary contains frequency information) when considering total intensity; a clear distinction on which to use is not apparent so we utilize the textbook interpretation of Hecht [92]. The critical electric field strength in gold to exceed the lattice binding strength is approximately  $2.76 \times 10^{10}$  V/m [59]. The total electron deficient, or holes, present in the particle due to emission processes may be found by integrating Eq. 4.28 over both space and time. A non-zero charge distribution results from this electron deficit inducing an electric field within the particle describable by Gauss's Law.

$$\nabla \cdot \vec{E} = \frac{\rho_e}{\epsilon_o} \quad (4.33)$$

Combining Eq. 4.29 and Gauss's Law with the assumption of uniform charge distribution within the particle gives the desired function containing critical electron temperature, particle enhancement, and laser intensity to exceed this binding strength.

$$E_{cr} \leq \frac{r_o}{3\epsilon_o V_{np}} \int_t \int_{A_s} (\vec{J}_o + \vec{J}_3) dt dA \quad (4.34)$$

At the particle surface, this assumption of uniform charge distribution is not valid below electron-equilibrium times and may lead to an over prediction in electron tem-

perature needed to induce monolayer particle ablation by electrostatic ion repulsion during photoemission.

Local near-field enhancement,  $Q_{NF}$ , necessary for these calculations are found from Mie scattering theory, calculated by Rick Harrison (Figure 4.2). In addition to the case of 50 nm gold particles exposed to 780 nm light, we also include 38 nm gold particles exposed to 400 nm light theory validation. Plech and co-workers made ablation measurements of the later particle and light combination in a water medium exposed to 100 fs using an elegant x-ray diffraction technique where changes in lattice configuration are measured by changes in Bragg scattering intensity [95]. The observed particle reshaping in the near-field polar regions at average fluences (if particles were centered in the Gaussian pulse, the local fluence would be twice this) of  $9 \text{ mJ/cm}^2$ . They attributed their observed polar ablation to particle near-field enhancement but did not provide a theory to predict or describe the process. This experiment is ideal for validation of our application of the GFD to nanoparticle ablation by ultrashort laser pulses. Note that for 400 nm light and gold, a two-photon process will result. Conveniently, Logothetis and Hartman also measured the two-photon current cross-section ( $b$ ) for gold to be  $4.2 \times 10^{-3} (A/cm^2)/(MW/cm^2)^2$ . Combining Eqs. 4.29, 4.31, 4.34, 4.32, we arrive at the final form of critical electron temperature, near-field enhancement and pulse duration to induce ablation at the particle surface due to electrostatic forces for 780 nm light and gold material.

$$E_{cr} \leq \frac{A_o}{\varepsilon_o} \int_t T_e^2 \exp\left(\frac{-\Phi}{k_B T_e}\right) dt + \frac{c}{2\pi\varepsilon_o} \left(\frac{2F}{\tau_p} \sqrt{\frac{\ln 2}{\pi}}\right)^3 \int_t \frac{\dot{F}(\chi)}{\chi^2} \exp\left[-12 \ln 2 \left(\frac{t}{\tau_p}\right)^2\right] dt \int_0^{2\pi} \int_0^\pi Q_{NF}^3 \sin(\theta) d\theta d\phi \quad (4.35)$$

where  $\chi = \frac{3h\nu - \Phi}{k_B T_e}$ . A similar form with  $n = 2$  instead of  $n = 3$  is easily derived for

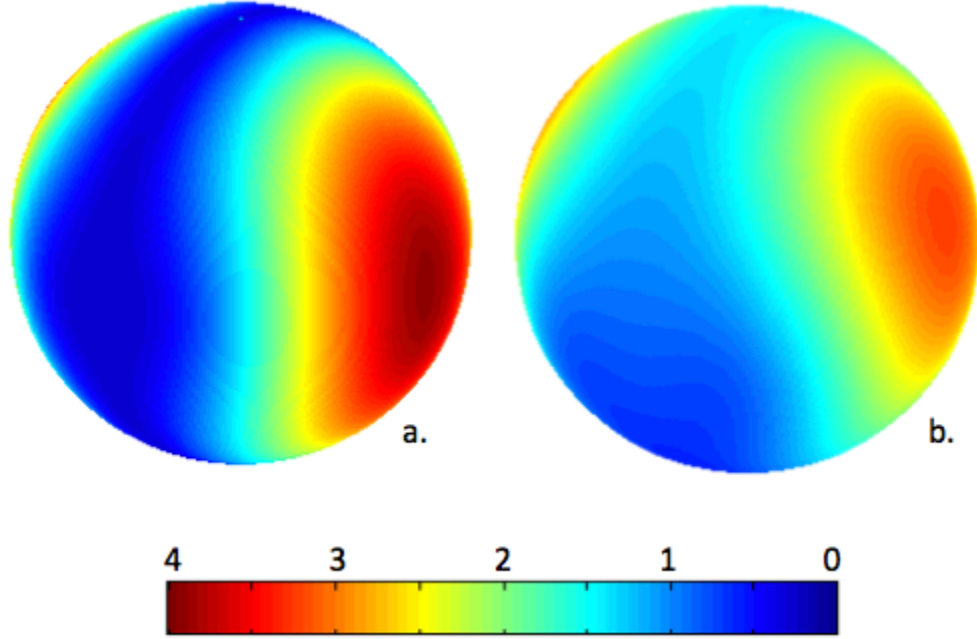


**Figure 4.2:** Surface near-field enhancement of the Poynting vector magnitude for Au spheres suspended in water medium for (a) 50 nm particle exposed to 780 nm light ( $Q_{NF,max} = 3.9$ ) and (b) 38 nm particle exposed to 400 nm light ( $Q_{NF,max} = 3.2$ ),  $Q_{NF} = \frac{S_{NF}}{S_{incident}}$ . Some regions experience a reduction in field strength while others experience a large increase. Courtesy of R. K. Harrison.

the test case of 400 nm light. Note that we have neglected the reflectance term for the case of nanoparticles. We justify this deviation from the classic GFD theory because the optical penetration depth for gold is on the order of our nanoscale particle sizes thus, field rejection is negligible for particles of interest in this work. Our derivation of Eq. 4.35 is apparently the first extension of the Fowler-DuBridge electron emission theory to plasmonic nanoparticles.

## Chapter 5

### Numerical Results and Discussion

Numerical results are kept as generic as possible however, some are focused towards the case of 50 nm particles irradiated with 780 nm wavelength light to correlate with our nanoparticles. We first analyze electron temperature distributions to determine the range of validity of lumped electron temperature assumption followed by continuous three temperature surface fits as a function of non-dimensional parameters. We then determine particle current density for 50 nm particles irradiated with 780 nm wavelength allowing the expression of photodisruption regimes as a function of non-dimensional parameters.

#### 5.1 Particle Electron Equilibrium

To access the validity of lumping electron temperatures, we track the evolution of maximum and minimum temperatures across the particle (Figure 5.1). For comparison, temperatures are normalized by their maximum (value which is at the front-most position with respect to the incoming beam) for comparison. We examine multiple pulse durations of 200, 100, 50, 25, and 10 femtosecond along with 25, 50, and 100 nm diameter spheres with an optical penetration depth,  $\delta$ , of 15 nm. Thus, the most severe case we have examined is  $\delta/d = 0.15$  and a pulse duration of 10 fs. We can expect lower  $\delta/d$  ratios and shorter pulse durations to result in more severe temperature gradients.

Figure 5.1, shows the lumped electron assumption is valid to within 20% of

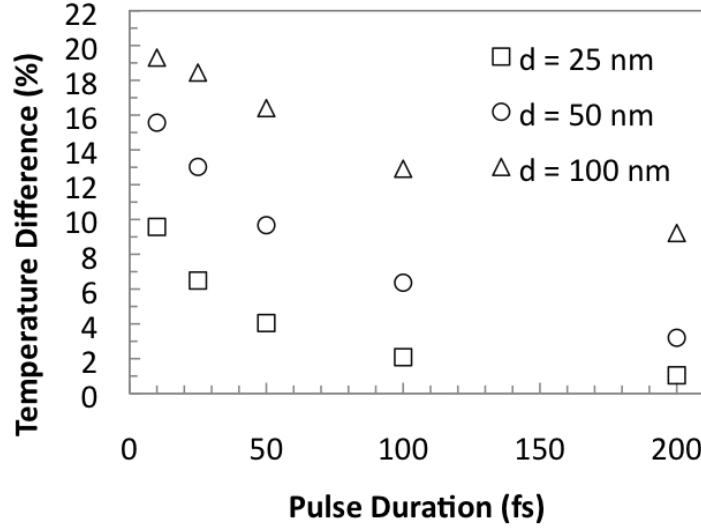


**Figure 5.1:** Maximum electron temperature difference ( $\frac{T_{max}-T_{min}}{T_{max}}$ ) across Au spheres of varying diameter and pulse duration with an optical penetration depth of  $\delta = 15$  nm. Sphere is positioned at the center of the beam axis.

the maximum attained temperature for pulses as short as 10 fs ( $\gamma > 1 \times 10^{-2}$ ) and 100 nm diameter particles. We tentatively extend these model results to broader cases and suggest  $\frac{\gamma\delta}{2r_o} > 5 \times 10^{-3}$  as a lumped electron validity condition for different sized particles or different optical penetration depths. The slightly different slopes seen between the different sized particles are due to the different ratios between particle diameter and optical penetration depth.

Again, we stress that in the case of coherent electron oscillations (plasmon resonance) the deposition of energy into the electron system would be more uniform than the laser heating source term of Eq. 4.8 due to uniform surface electron excitation and subsequent electron-electron relaxation. Given uniform energy deposition along the particle surface, we can expect the temperature gradient across the particle to be more than half of what our current model predicts. Thus, our suggested

validity criteria is very conservative for plasmonic nanoparticles.

Electron temperatures resulting from the lumped particle heating model are effectively volume-averaged values. Below the indicated  $\gamma$  range, electrons will be increasingly non-equilibrated, leading to an under prediction in peak electron temperatures as lumping will average out these local peaks. Thus, inappropriate lumping would also under-predict photoemission of electrons from the particle surface. Potentially, non-equilibrium electrons may cause the particle to fragment, reshape, or pit as the exposed surface ions experience increased repulsion with electron emission than bulk material.

## 5.2 Maximum Temperature Surfaces

We now examine the maximum temperatures achieved by each subsystem as a function of the previously identified non-dimensional parameters. Plots of each temperature subsystem are given in figures 5.2, 5.3, and 5.2 over a range of  $\gamma = \{0.0095 : 9.5 \times 10^4\}$ ,  $\beta = \{0.01 : 1 \times 10^5\}$ , and  $\epsilon = \{0.21 : 3.15\}$ . We also present limited fits of these numerical results for regions of typical operation. More complete fits by the method of stitching different log-linear portions together with the arctangent 'switch' functions as in equation 4.26 are provided in the appendix.

We see in Figures 5.3 and 5.4 scaled electron and phonon subsystems, the  $\epsilon$  parameter has no effect until higher  $\gamma$  values, while for the water temperature in Figure 5.2, it serves to raise or lower the entire temperature response surface. This shows how both scaled electron and phonon temperatures are largely insensitive to surface conduction until  $\gamma \approx 1000$  and  $\gamma \approx 300$ , respectively. While  $\epsilon$ , being a measure of electron-phonon to phonon-water coupling rates, is large there is significant interfacial resistance causing conduction time scales larger than the rate of heat deposition to either the electron or phonon subsystem. Thus, the maximum

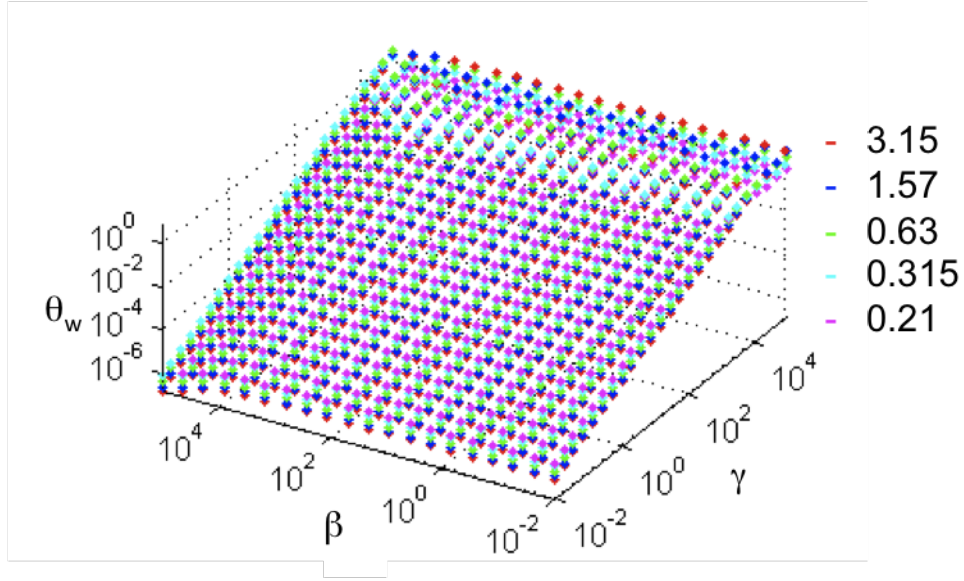


**Figure 5.2:** Maximum scaled surface water temperatures with constant  $\epsilon$ 's as a function of  $\gamma$  and  $\beta$ .

temperatures achieved by both the phonon and electron subsystem is unaffected by  $\epsilon$  until the regimes identified above. However, all water surface maximum temperatures depend directly upon  $\epsilon$  unless the rate of conduction through the particle-water interface is faster than the rate of heat diffusion which, is not possible.

The water and phonon system both see a leveling off of the response surface at a  $\gamma$  which is a function of  $\epsilon$ . The transition value to a constant scaled temperature occurs at  $\gamma \approx 1 \times 10^4 \epsilon^{-2}$  for water and  $\gamma \approx 1 \times 10^4 \epsilon^{-3/2}$  for phonons. Prior to this region, both experience a region dependent only upon  $\gamma$  from  $\beta < 1 \times 10^4$ . At larger  $\beta$  values, both  $\gamma$  and  $\beta$  affect the scaled temperatures. The  $\beta$  dependence is the result of lattice specific heat being a weak function of temperature in the code; in the vicinity melting, although not explicitly accounted for in this analysis, the lattice specific heat experiences significant changes.



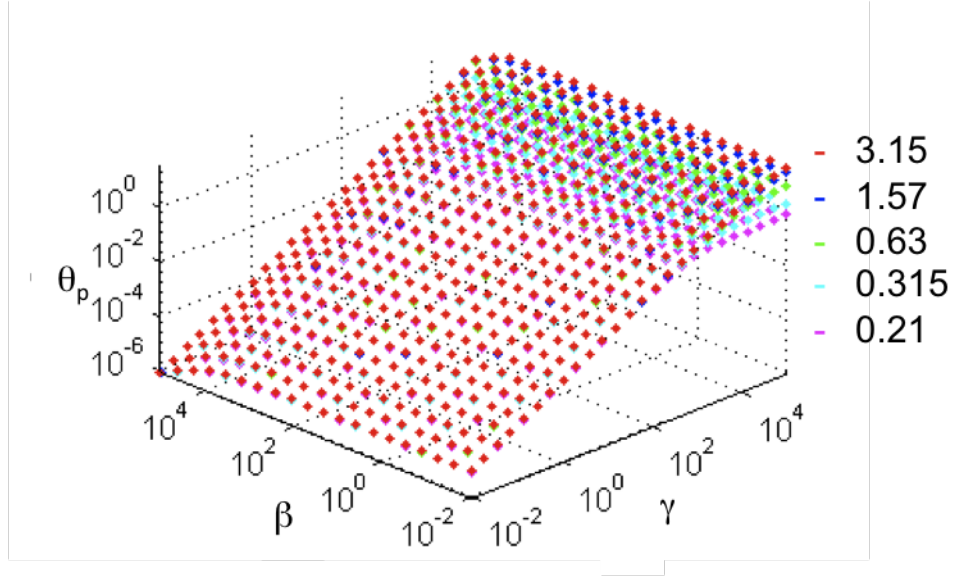


**Figure 5.3:** Maximum scaled particle lattice temperatures with constant  $\epsilon$ 's as a function of  $\gamma$  and  $\beta$ .

The electron subsystem exhibits the most complex behavior with a plateau region and two descending temperature surfaces as independent functions of  $\gamma$  and  $\beta$ , and then an  $\epsilon$  dependent region causing additional non-linearities. The plateau indicates constant scaled temperatures of  $\theta_e = 0.1$  independent of all parameters for the range of  $\gamma < 1$  and  $\beta < 1$ . The  $\beta$  induced non-linearity in equation 4.19 is insignificant when  $\beta < 1$  causing the scaled electron temperature surface to be independent of  $\beta$ . As discussed in the previous section,  $\gamma < 1$  conditions result in energy deposition entirely to the electron subsystem before decaying through electron-phonon coupling manifesting itself as regions of electron temperature surfaces exhibiting a region independent of  $\gamma$ . When both parameters are greater than one, the response surface shows complex dependence on both parameters.

Reduced fits are given in equations 5.2, 5.2, and 5.2 and may be used for

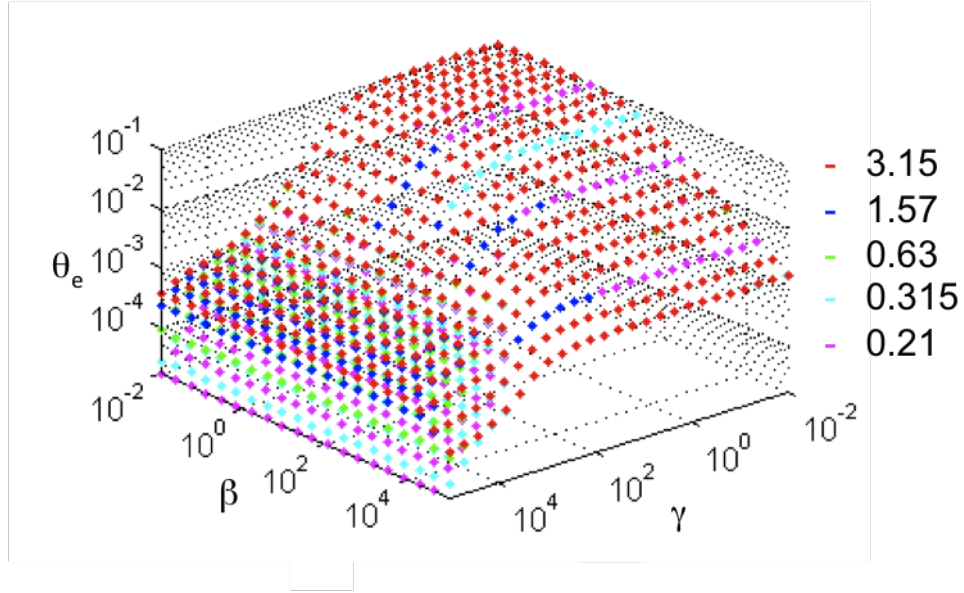


**Figure 5.4:** Maximum scaled particle electron temperatures with constant  $\epsilon$ 's as a function of  $\gamma$  and  $\beta$ .

a variety of particle geometry, material, and laser properties instead of performing additional and specific numerical analysis. Based upon the previous analysis of electron equilibration, the results below  $\gamma = 1 \times 10^{-2}$  and  $\epsilon = 0.315$  are under-predictions of the maximum electron temperature. Also, note that we have *not* included latent heat of melting for the particle or latent heat of evaporation for the water so that if  $T_P > 1337$  or  $T_w > 647$ , these fits and plots are no longer valid. However, they can give us the onset of melting and evaporation and can thus serve as damage regime indicators and bounds.

Electron Temperatures:

$$\theta_e = \begin{cases} 0.1 & \text{if } \gamma < 1 \& \beta < 1, \\ 0.272\beta^{-0.448} & \text{if } \gamma < \beta^{\frac{2}{5}} \& \beta > 40 \end{cases}$$

Lattice Temperatures:

$$\theta_p = \begin{cases} 7.93 \times 10^{-4} \gamma^{0.997} & \text{if } \gamma < 43.3 \epsilon^{1.41} \& \beta < 10^4, \\ 436 \exp(-3.86 \epsilon^{-0.366}) & \text{if } \gamma > 43.3 \epsilon^{1.41} \& \beta < 10^4. \end{cases}$$

Water Temperatures:

$$\theta_w = 2.13 \times 10^{-4} \epsilon^{-0.588} \gamma^{0.997} \exp[0.0978 (\ln \epsilon)^2] \text{ if } \gamma < 77.5 \epsilon^{1.41} \& \beta < 10^4,$$

Coefficient vectors have been optimized using Matlab's built-in nonlinear least-squares curve fitting tools. The fits agree with numerical results for the given parameter range to within a 95% confidence interval of  $\pm 6.9\%$ ,  $\pm 3.0\%$ , and  $\pm 3.8\%$ , for the water, phonon, and electron temperature systems, respectively. Fits of more logarithmic-arctangent form are presented in the appendix and are valid over larger regions of the maximum temperature response surfaces at the cost of significantly more complex form. We recommend the latter fits as they are more general and accurate.

With these equations or scaled temperature response surfaces, we may find particle melting and water explosive boiling curves by iterating or interpolating upon parameters and critical temperatures. We perform these calculations after we establishing the critical electron temperatures and laser conditions for particle ablation by electrostatic repulsion.

### 5.3 System Temperatures Evolution

Figure 5.5 highlights the different behavior of the heating process given four distinct parameter regimes and reinforces Section 4.1.2 discussion of the physical meaning behind the electron energy transfer number,  $\gamma$ , two-temperature Biot number,  $\epsilon$ , and scaled energy absorption,  $\beta$ . Representative cases of  $\gamma < 1 \& \epsilon < 1$ ,  $\gamma < 1 \& \epsilon > 1$ ,  $\gamma > 1 \& \epsilon > 1$ , and  $\gamma > 1 \& \epsilon < 1$  depict the differences in temperature

evolution for the electrons, lattice, and water subsystems. For all cases presented in Figure 5.5,  $\beta = 1.4 \times 10^3$ . Data is plotted until the water temperature at the particle surface reaches its maximum temperature. Table 5.3 shows the unscaled temperatures for comparison. Note that all temperatures start at 300K, the log scale plotting omits the first few steps.

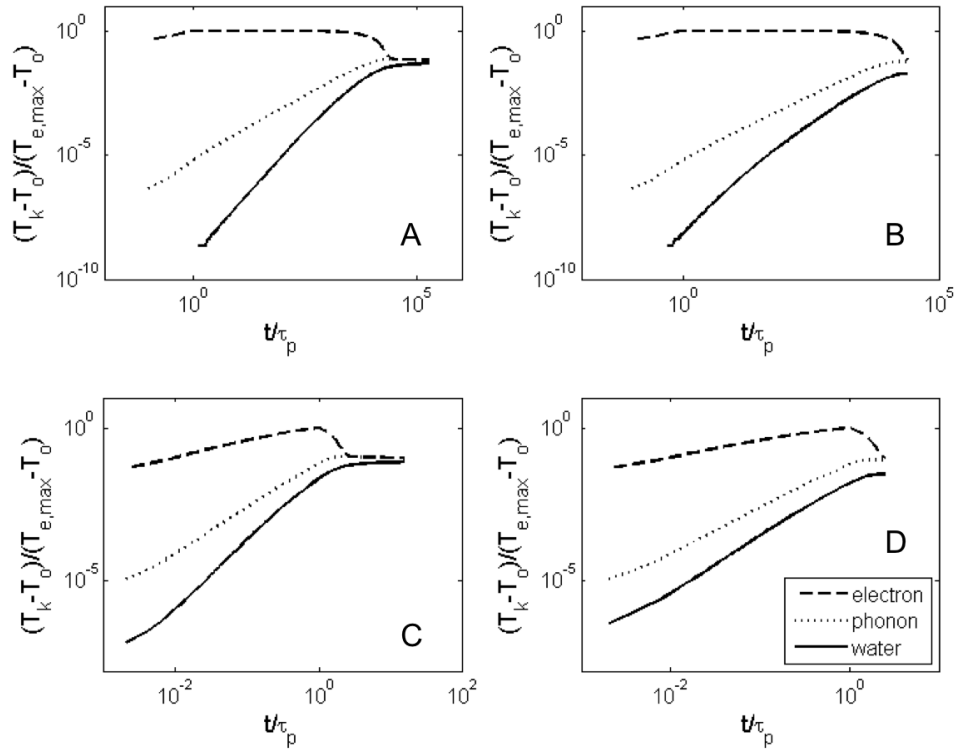


**Figure 5.5:** Temporal evolution of temperatures of the electron, phonon, and water for gold spheres suspended in water and heated with short pulse irradiation for (A)  $\gamma = 0.0095$  ( $\tau_p = 10fs$ ) &  $\epsilon = 0.315$  ( $r_o = 50nm$ ), (B)  $\gamma = 0.0095$  ( $\tau_p = 10fs$ ) &  $\epsilon = 3.15$  ( $r_o = 5nm$ ), (C)  $\gamma = 115$  ( $\tau_p = 120ps$ ) &  $\epsilon = 0.315$  ( $r_o = 50nm$ ), and (D)  $\gamma = 115$  ( $\tau_p = 120ps$ ) &  $\epsilon = 3.15$  ( $r_o = 5nm$ ).

Figures 5.5 A and B with  $\gamma = 0.0095$  are representative of  $\gamma < 1$  cases which, result in electron temperatures reaching a sustained maximum as energy is added

to the electron system at a faster rate than can be removed by phonon coupling. This sustained high electron temperature will be optimal for thermionic electron emission or particle ablation for a given laser energy. For  $\gamma > 1$  in Figures 5.5 C and D, the electron temperature reaches its peak at the end of the laser pulse. This peak is lower than  $\gamma < 1$  case (Table 5.3).

Figures 5.5 A and C with  $\epsilon = 0.316$  show  $\epsilon < 1$  conditions where the electron and phonon system reach equilibrium long before the water achieves its maximum temperature. However, all three subsystems reach equilibrium at the same time for  $\epsilon > 1$  (Figures 5.5 B and D) cases and will then decay at the same rate afterwards. Additionally, as  $\epsilon$  increases, a larger temperature discontinuity between the particle and surrounding medium is achieved. Thus, if we would like to avoid particle melting for imaging applications, operating in the  $\epsilon > 1$  regime would be ideal. If we were interested in causing transient photothermal damage without inducing bubble formation, large  $\epsilon$  and  $\gamma$  values would be ideal. However, to induce successive bubble formation by heating alone without damaging our particles, large  $\epsilon$  and small  $\gamma$  values should be selected. The notion of selective damage regimes is explored further in the following sections.

Table 5.1: Maximum temperatures for  $\beta = 1.4 \times 10^3$

		$\gamma = 0.0095$ $\gamma = 115.4$	
$\epsilon = 0.315$	$T_e(K)$	5097	3281
	$T_p(K)$	639.7	638.5
	$T_w(K)$	526.1	525.5
$\epsilon = 31.5$	$T_e(K)$	5097	3278
	$T_p(K)$	576.7	572.9
	$T_w(K)$	390.2	389.4

## 5.4 Particle Ablation Threshold

For particles exposed to pulsed laser irradiation, we can predict the current density and corresponding electron flux resulting from multiphoton and thermionic emission using the electron temperatures calculated in the previous section and the near-field enhancement such as in Figure 4.2. By combining the critical electric field strength to exceed Au lattice binding strength using calculated current density (eq 4.35) and the critical system temperatures to induce particle melting temperature and explosive water boiling, we can construct photodisruption diagrams for specific particles and laser wavelength. We present these results for 50 nm spheres exposed to 780 nm light (Figure 5.6).

The variations in the binodal, spinodal, and melt curves at higher  $\gamma$  values are due to the pulse duration exceeding the phonon-water relaxation time. Before these pulse durations, the melt and boil energy input needed is constant as the maximum temperatures achieved is essentially constant for a given input energy, that is, the surrounding medium cannot remove heat as fast as it is being applied so that temperatures are incubated and sustained over the applied laser pulse. The kink in ablation curves is due to a change from multiphoton to thermionic dominated emission processes. The near vertical portions are due to sustained electron temperatures, after which (higher  $\gamma$ ) the maximum electron temperature drops and the process of thermionic emission requires higher absorbed energy to maintain. Just below the transition to thermionic emission, we see multiphoton effects dwindling to zero. However, at low  $\gamma$  conditions, multiphoton effects driven by high peak intensities at the particle surface due to near-field enhancements of high intensity laser pulses drastically reduces the required energy to initiated photodisruption.

Region A appears to be a 'safe' zone for imaging where no photodisruption will occur. However, in the region just to the left of the monolayer ablation curve,

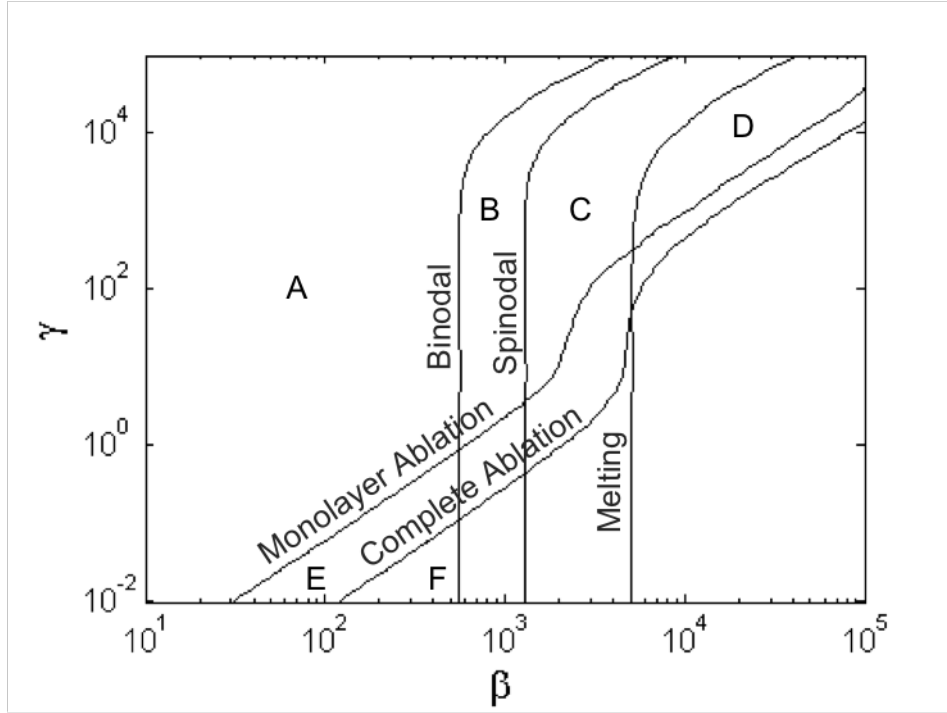


**Figure 5.6:** Photodisruption diagram for 50 nm spheres exposed to 780 nm light as a function of  $\gamma$  and  $\beta$ . Labeled damage regions will occur to the right of their indicated threshold lines.

free electron generation will be significant and lead to ROS formation and possibly small cavitation bubbles. Region B, from binodal to spinodal and above ablation, would result in bubble formation in the longer pulse regime (several nanosecond) with diminishing probability as pulses were shortened. Particles in region C, area bound by spinodal and above ablation will see cavitation bubble formation by water temperature rise alone and the particles themselves will be unaffected. Particles will only melt (area D) in the longer pulse regime as the majority of the melt temperature line is within the particle ablation regime. However, it is important to note these results are for single pulses. Applications such as imaging and ROS generation rely upon many pulses of low power in the MHz regime so that melting may occur due

to heat accumulation without elevated electron temperatures or high intensities.

Region E exceeds  $E_{cr}$  and will experience particle ablation or fragmentation by electrostatic repulsion due to photoemission of electrons. The monolayer ablation line may shift to lower  $\beta$  values at lower  $\gamma$  due to non-uniform charge density in the particle with an increase near the surface resulting in higher induced fields at the surface. Particle ablation by electrostatic repulsion requires very high absorbed energy at long pulse durations (high  $\gamma$ ) while requiring minimal energy to induce photodisruption at short pulse durations. Thus, the theories utilized here suggest an ultra-energy efficient region of photodisruption requiring substantially less energy to induce similar results as longer pulses durations of substantially higher energy. Although, the total energy input in these regions may be small, the power input into the system through energetic electrons and ions can be expected to be significant. Photodisruption at lower energies is extremely important to in-vivo treatment of skin cancer due to the attenuation of laser intensities traveling through human tissue. Region F indicate conditions where particles will be completely ablated and may be optimal if damage is only achievable by ballistic impacts of ions with surrounding material such as cellular membranes due to low total energy inputs.

To validate our application of the generalized Fowler-DuBridge theory to nanoparticle-light interaction, we compare our predictions with experimental results from Plech and co-workers for 38 nm Au spheres exposed to 400 nm light [95]. Using an x-ray scattering technique, they were able to measure polar particle ablation beginning at a fluence of  $9 \text{ mJ/cm}^2$  with 100 fs pulses. Figure 5.7 shows a comparison of Plech and co-workers experimental results and our predictions using the theories and models assembled in Chapter 4. It is unclear in [95] whether the reported fluence is the average or peak value, hence we have plotted both values; however, it is customary to report average values. Additionally, there is no indication of



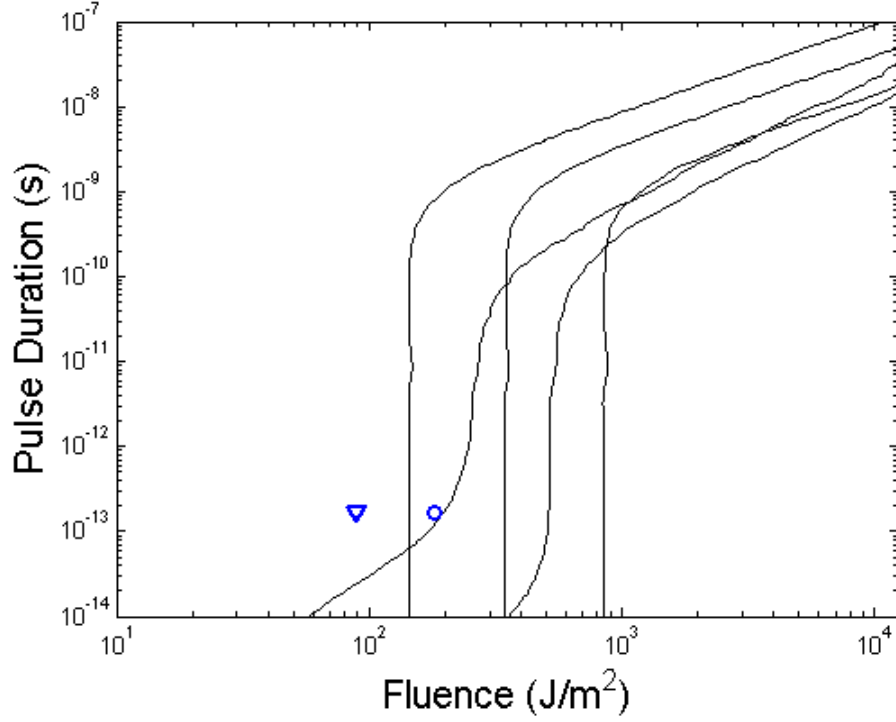


**Figure 5.7:** Photodisruption diagram for 38 nm spheres exposed to 400 nm light as a function of fluence and pulse duration with the experimentally observed polar ablation threshold ( $90 \text{ J/m}^2$ ) of Plech *et al* [95]. Our modeling predicts a monolayer ablation threshold of  $220 \text{ J/m}^2$ . The triangle assumes reported fluences are peak while the circle assumes average

where in the Gaussian pulse the particles are located in their experiment. Given these uncertainties and the assumptions we have made throughout this work, our result for monolayer ablation correlate very well with the experiments of [95]. Our assumptions of uniform charge distribution and uniform electron temperatures are conservative and cause our predictions to be higher than actual values, as observed.

It is worth comparing the location of the monolayer ablation line with respect the water spinodial line at pulse durations lower than electron-phonon relaxation

times for the case for 50 nm particles with 780 nm light (Figure 5.6) and 39 nm particles with 400 nm light (Figure 5.7). For the prior case, thermionic ablation occurs at energies higher than necessary to initiate explosive boiling. It is only at shorter pulse durations, where multiphoton-assisted emission occurs, that ablation requires less energy than boiling. However, for the case of 38 nm particle exposed to 400 nm light, the thermionic ablation line occurs at *lower* energies than the spinodal. Therefore, for sub-electron-phonon relaxation pulse durations, there is a region where explosive boiling is the more energy efficient photodisruption mechanism for 50/780 case while for the 30/400 case, ablation is always more energy efficient. This subtle difference shows how careful selection of particle geometry and light conditions is crucial for optimizing ones application.

Modifications may be necessary to include the reabsorption of electrons that is very likely with longer pulse durations and with free electron formation around the particle. Additionally, induced electric particle fields due to electron emission and the emission itself may play an important role in altering the plasmonic properties of the particle as well as particle re-shaping during ablation. Inclusion of the latter phenomena may cause our predicted monolayer ablation lines to shift to higher fluences. Space-charge induced potential barriers caused by electron repulsion of emitted electrons was examined according to the treatment of Riffe and co-workers and found to have no effect on the monolayer and complete ablation lines presented here due to the compatibly low total electron yield of particles to films [62].

Particle ablation may induce photodisruption by multiple mechanisms: bubble formation as hot energetic Au ions and electrons rapidly expand into the surrounding medium, ballistic disruption of surrounding materials, large additions of free electrons during applied pulses to seed cascade ionization, and the formation of a small region filled with energetic ions that act as nucleation sites for bubble

formation.

As previously noted, cavitation bubbles may form due to free electron generation induced plasma pressure and thermal temperature rise from recombination. Thus, there will be an area in figure 5.6 in the vicinity of the ablation curves where bubble formation may be assisted by particle free-electron seeding. Though not examined in this work, calculation of free electron generation may be performed as outlined in the theory section to determine emission assisted bubble and ROS formation regimes.

## Chapter 6

### Experimental Results and Discussion

We now present and discuss experimental bubble measurements and corresponding average fluences for the particle solution and control solution. From these results, we can determine the particle photodisruption threshold reduction for our 50 nm Au spheres excited by 780 nm 180 fs pulses in water. We frame experimental observed enhancement in the context of the previously developed theories and numerical results. Additionally, we examine the distribution of bubbles sizes for a given energy level.

#### 6.1 Threshold Reduction

As described in Chapter 3, we performed a pump-probe experiment to measure unscattered probe signals, shown in Figure 3.2. Figure 6.1 displays resulting maximum bubble radii calculated using Eq. 3.8 for all energy levels and both nanoparticle and control solutions. The minimum discernible bubble oscillation signal of 25 ns corresponds to a bubble radius of approximately 300 nm at a minimum fluence of  $120 \text{ mJ/cm}^2$  for the nanoparticle solution and  $7.7 \text{ J/cm}^2$  for the control solution (Figure 6.2). It is worth noting that the theoretical minimum bubble radius predicted by Vogel *et al.* is given as 70 nm [8]. Directly comparing the minimum fluences we directly observe bubbles at for the control and nanoparticle solution, a 60 times enhancement results. However, the observed bubbles at the smallest energy levels are likely due to particle clusters. To quantitatively determine

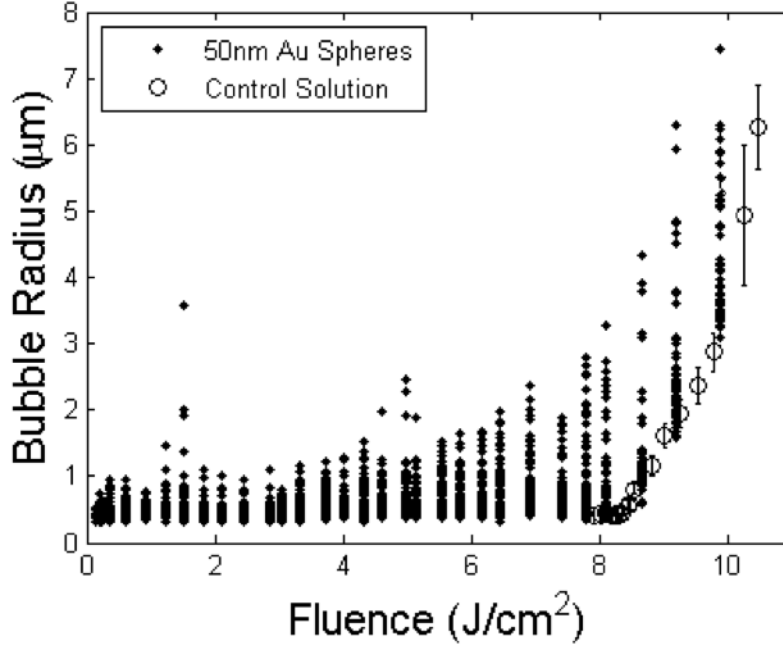


**Figure 6.1:** Maximum bubble radii as a function of applied pump beam average fluence for 50 nm gold nanosphere solution (dots) and control solution (circles). Bubbles created due to nanospheres are shown to converge to the control solution without nanoparticles at higher fluences. Pulses exhibited a  $\pm 2\%$  energy variability.

the true enhancement, we utilize the particle kinetics method developed in Section 3.1. Using average energy levels of 1.46, 1.66, 1.80, 1.86, and 1.94 nJ, 5000 additional bubble measurements are performed allowing a statistically significant measure of the time between bubble triggers and therefore particle location within the focal volume generating the minimal observable bubbles. We assume this method causes any clustered particle triggers to become statistically insignificant with respect to single particle triggers. The calculated true threshold using Eqs. 3.2 through 3.7 for single 50 nm Au spheres exposed to 180 fs (FWHM) 780 nm laser pulses is  $253 \pm 54 \text{ mJ/cm}^2$  yielding a photodisruption enhancement of 31 times. By simply

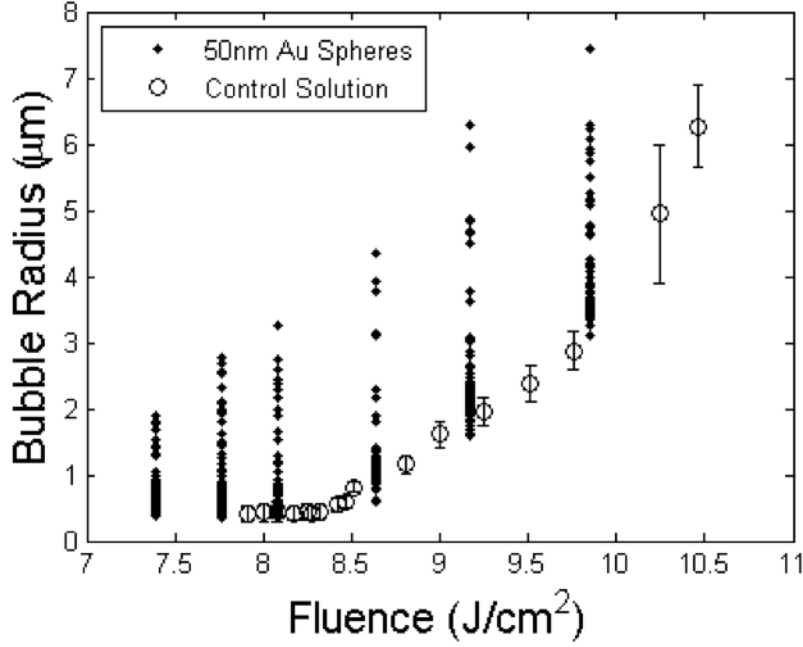


**Figure 6.2:** A blow-up of control solution bubble measurements shown in Fig. 6.1. Maximum bubble radii as a function of applied pump beam average fluence for 50 nm gold nanosphere solution (dots) and control solution (circles). Bubbles created due to nanospheres are shown to converge to the control solution without nanoparticles at higher fluences. Pulses exhibited a  $\pm 2\%$  energy variability.

taking measurements at low energy levels for extended periods of time, there is an increasing probability for clusters to result in detectable bubble formation leading to an incorrect observation of threshold reduction.

We note the technique developed here is the only current quantitative method of determining particle mediated bubble enhancements while suspended in aqueous media without the aid of a large synchrotron radiation facility [84]. While very useful for specific applications, other reports of particle enhancement (Tables 2.2-2.5) have been mostly qualitative in nature, relying on secondary indicators such as cellular dye uptake or minimum observed bubble thresholds which we have shown

can be very misleading.

Observed bubble radii in the nanoparticle solution converge to bubbles created in the control solution without nanoparticles at higher fluences. This is an expected result, as the pump beam will create bubbles without the aid of nanoparticles at these fluences. Additionally, the increase in bubble size due to the presence of nanoparticles diminishes at these higher energy values. The near-constant control solution bubble sizes seen around  $8 J/m^2$  (Figure 6.2) is likely due to an undesirable thresholding of bubble size due to the detection limits of the system; that is, the actual average bubble size created at these lower energies is smaller than we observe. However, these findings are not very inconsistent with measurements by Vogel and co-workers in a pure water solutions where they also report a leveling-off of bubble size decrease at lower energies [96].

Comparison with literature is difficult due to the wide variety of nanoparticle geometries, focusing conditions, and pump beam characteristics used by different groups as indicated in Tables 2.2 - 2.5. Nevertheless, we discuss our finding with respect to others here. Bubbles of  $322 \pm 96$  nm radii in distilled water were created using 18.5 nJ, 150 fs excitation pulses at 1040 nm wavelength using a 0.9 NA objective by Vogel *et al* [96]. Our control solution threshold is found to be 33 nJ for  $300 \pm 24$  nm bubbles and thus agrees fairly well even though we used a different wavelength and longer pulse (180 fs). Additionally, we used a solution with citrate ions and pluronic stabilizer as our control, which results in different bubble formation thresholds due to slightly different breakdown mechanisms and dielectric constant/index of refraction.

Previous measurements using an X-ray probe technique by Kotaidis *et al.* [57] made with 39 nm gold nanospheres and a 400 nm 100 fs pump beam resulted in a threshold of  $300 J/m^2$  for initiation of nano-bubbles on the particle surface. Bubbles

of 80 nm radii were measured in the same experiment at 1000  $J/m^2$  correlating fairly well with our fluence of 2281  $J/m^2$  for 300 nm bubbles. The discrepancy can be attributed to their study operating closer to the nanoparticle resonant frequency and, obviously, their smaller observed bubbles.

Lapatko has made numerous threshold measurements with nanosecond and picosecond pulses [25, 69, 24] at wavelengths of 532 nm. Lapatko's bubble measurement thresholds vary by a large extent, for instance with 532 nm, 100 nm Au spheres, and 500 ps pulses he reports a fluence of 50,000  $J/m^2$  while with 532 nm, 500 nm Au spheres, and 12 ns pulses he reports a fluence of 1,000  $J/m^2$ . The latter is on the order of our observed threshold and based upon our numerical results, we would expect our threshold to be lower based upon the shorter pulse duration. However, 532 nm wavelength light is much closer to the resonant frequency of the range of Au nanospheres than the 780 nm wavelength used in our study (Figure 2.1). It is important to note tissue absorbs approximately 5 times more and scatters 2 times more at 532 nm than 780 nm, hence, our off-resonant selection of wavelength [97].

Our measurements are certainly consistent within the wide range of experimental results in the literature and no groups have performed the combination of nanoparticle size and laser parameters. Also, our observed thresholds are below all those of organic cellular particles (Table 2.5) observed in the visible regime (532 nm). We can assume these thresholds would increase significantly with the use of 780 nm since melanosomes are specifically tuned to absorb visible light as a defense mechanism for the body. What is significant in these findings when compared to the absorption of melanosomes, is that even with focused 780 nm pulses, skin cells will not heat to the point of bubble formation or cell death from light above the focal plane. Less heating would also result from using short pulses instead of the



nano and micro second pulses listed in Table 2.5 due to the deposition rate of energy being below thermal relaxation timescales leading to heating confinement and the overall smaller energy deposition necessary to achieve bubble formation. This is clearly visible when examining the binodal and spinodal lines of the surrounding medium for particle heating as a function of increasing pulse duration (Figures 5.6 and 5.7 ).

This 31x enhancement does not correlate directly with particle near-field enhancement or absorption efficiency resulting from Mie theory, which predict a highly localized ( $\approx 10\text{nm}$ ) maximum Poynting vector magnitude, and therefore intensity, enhancement of  $Q_{NF} = 3.9$  (Figure 4.2) and an absorption efficiency of  $Q_{abs} < 1$  (Figure 2.1). To explain our enhancement, we turn to the previously developed photodisruption regime diagram and place our results in the context of analysis performed in the numerical sections (Figure 6.3). Our test conditions are above the theoretical monolayer particle ablation threshold and the spinodal line while being below the theoretical complete particle ablation line. Therefore, we can not explicitly rule out particle heating and direct conduction to the surrounding fluid in bubble formation at our smallest detectable bubble size. However, the latter phenomena occur at longer timescales than electrostatic ablation so that these mechanisms are unlikely. Although the theory of metal ablation by electrostatic repulsion is not new and has been used quite successfully to explain film ablation, our work is the first application towards nanoscale particles[59, 61, 62]. However, particle ablation and fragmentation has been observed in previous experiments utilizing short-pulse illumination [79, 78] and our theory correlates very well with observed particle ablation of [98] (Figure 4.2). In light of these previous studies and the location, our test conditions being past the monolayer ablation line, and the timescales of ablation being shorter than medium heating, mechanisms of bubble

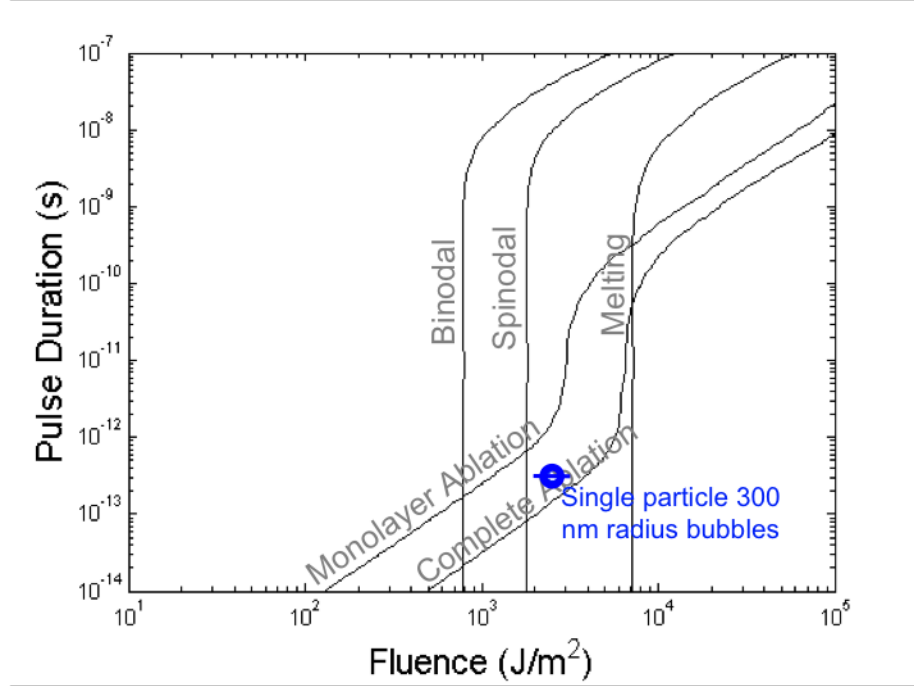


**Figure 6.3:** Photodisruption diagram for 50 nm diameter spheres exposed to 780 nm light as a function of pulse duration and applied local-particle fluence. The blue circle indicates our experimentally determined minimum threshold to induce 300 nm radius bubbles with single particles. Labeled damage regions will occur to the right of their indicated threshold lines.

formation other than thermal diffusion are likely occurring in addition to simple particle heating. Possible mechanisms include hot energetic Au ions and electrons rapidly expanding into the surrounding medium creating cavitation, Au ions (or the particle itself) serving as bubble nucleation sites, and photo-emitted free electron seeding of cascade ionization.

The minimum size of the detectable bubbles in our experiments is well above the theoretical minimum bubble size predicted by Vogel for thermoelastic-initiated bubbles [8] and observed by Plech [98]. Smaller bubbles would be significantly to the left our observed minimum in Figure 6.3.

## 6.2 Size Distribution

In the fluence region below bubble creation without nanoparticles, wide ranges of bubble size are observed at every average fluence level, often with an order-of-magnitude difference. Bubble size distributions normalized by the range of measured bubble radii at each corresponding energy level are plotted in Figure 6.4. The occurrence reduction near zero may be due to reduced detection sensitivity at the smaller bubble size or slight misalignment between the probe and pump beam so that some of the periphery of pump beam focal volume is not overlapping with the pump beam focal volume causing some small bubbles to go undetected. Alternatively, the reduction in small bubble size occurrence may correspond to a reduced probability of small bubble formation.

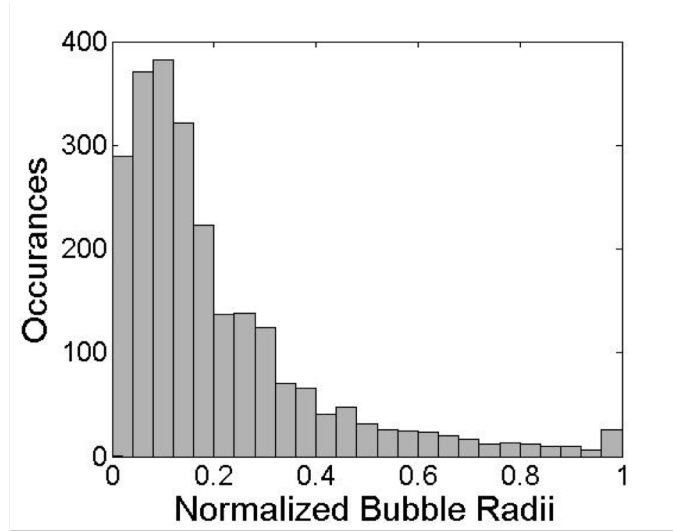


**Figure 6.4:** Summation of normalized bubble radii with respect to size range at each energy level. Occurrence reduction near zero may be due to reduced detection sensitivity at the smaller bubble size. The slight peak at one is an artifact of normalization bounds.

This distribution reflects the increasing particle probability of being located at a lower intensity within the focal volume due to the inverse relationship between

intensity and areas of equal intensity within an ellipsoidal focal volume of Gaussian energy distribution. The significance of these findings is when using nanoparticles to enhance and guide optical breakdown and cavitation bubble formation, we can not be certain of the exact extent of damage we will cause. However, we can tailor our selection of pulse energy and nanoparticles to the most likely or maximum/minimum acceptable damage outcomes. However, there is still much work to be done in the characterization of how bubble wall stress and momentum and shockwaves interact with plasma membranes.

The distribution we have observed here may explain the large degree of variability of previously reported bubble thresholds by other research groups. In addition to reducing supposed single particle thresholds, particle agglomeration and clustering would play a role in increasing bubble size variability. All other reported experimental measurements should thus be viewed with these observations in mind.

## Chapter 7

### Conclusions

To conclude, we will summarize the important findings of this body of work and some general implications. Through non-dimensional analysis of laser induced particle and surrounding medium heating governed by the two-temperature model and general spherical conduction, we identified three unique non-dimensional groups describing the heating process. The parameters includes the electron energy transfer number, two-temperature Biot number, and a scaled total energy absorption term. The numerical solution of these equation with respect to these non-dimensional parameters provide general trends and solutions for pulsed laser heating of electrons, phonons, and surrounding medium for a wide a wide variety of particle geometries, materials and laser conditions. Fits from these numerical results alleviates the need for future researchers to have to recalculate system temperature for their unique test conditions. We have numerically examined the validity of assuming lumped (uniform) electron temperatures and proposed a validity range based upon the electron energy transfer number and ballistic penetration depth of photons. We have extended the generalized Fowler-DuBridge theory of electron photoemission to plasmonic nanoparticles exposed to ultrashort pulsed excitation. The development of particle electron photoemission allow for both the determination of particle ablation thresholds and free electron generation enhancement via seeding of cascade ionization of the surrounding medium. The prior was calculated and validated in this work while the latter will be the subject of future research. Combining two-temperature model calculations with photoemission results provides particle photodisruption di-

agrams where one can select system parameters to achieve the desired outcome.

Experimentally, we have determined the cavitation bubble enhancement of 50 nm gold nanospheres exposed to 780 nm, 180 fs pulse irradiation to be 31 times for our minimum detectable bubble radii of 300 nm. Our method of threshold determination is quantitative while being both simple and cost effective and may be applied to any range of particles and laser parameters. When compared with our numerical analysis, bubbles are likely formed by particle ablation leading to rapidly expanding energetic Au ions leading to bubble nucleation. Our measurements have demonstrated the large degree of bubble radii variability possible for a given average laser fluence indicating the extent of disruption will vary greatly depending upon the random location of particles within a Gaussian beam profile.

The calculations and derivations in this thesis allow for a nearly complete determination of particle mediated photodisruption. Researchers interested in photodisruption via ablation, reactive species generation, cavitation bubble formation, and/or photothermal effects may utilize this work to guide and optimize their efforts. Additionally, multiphoton electron emission suggests extremely energy efficient regimes to induce photodisruption using ultrashort laser pulses. The small bubble sizes measured here would induce sub-diffraction limited mechanical damage to surrounding media and can be selectively and precisely induced by functionalizing nanoparticles to target and bind to specific biological receptors. Our large bubble threshold reductions using off-plasmon resonance test conditions indicate the possibility of using lasers to induce photodisruption with very low energies in deep-tissue applications using NIR tuned particles such as nanorods and shells.

## Appendix

## Appendix 1

### Neglect of Brownian Motion

When calculating the collision frequency between particles and a stationary and imaginary focal volume sphere of radius  $r_{fv}$ , we have neglected Brownian motion of particles considering only the bulk fluid motion. A particle initially at rest in a fluid medium above absolute zero will experience collisions with the medium molecules due to random molecular thermal motion. Each collision will impart some momentum transfer and cause the particle to move about in seemingly random directions. Based upon particle diffusion in a viscous medium, neglecting this motion in favor of bulk fluid motion due to pumping may be easily verified. The famous Stokes-Einstein diffusion coefficient for a particle of radius  $r_p$  traveling in a viscous medium and experiencing random collision events is given by

$$D = \frac{k_B T}{6\pi\mu r_p}, \quad (1.1)$$

where  $\mu$  is the fluid viscosity,  $k_B$  is the Boltzmann constant and  $T$  is the fluid temperature. The average distance,  $s$ , a particle will travel experiencing purely thermal motion over a time  $\delta t$  is thus [99]:

$$\langle s^2 \rangle = 2D\delta t \quad (1.2)$$

Similar to Equation 3.3, the average distance traversed by a particle before successive collisions with our fictitious focal volume particle is

$$\lambda = \frac{1}{n_p \pi (r_{fv} + r_p)^2}, \quad (1.3)$$



where  $n_p$  is the particle number density in the fluid. Setting the Brownian particle motion distance in Equation 1.2 equal to the mean-free-path distance of Equation 1.3 and rearranging yields the total time between successive collision events of a solution of nanoparticles at a given temperature with our focal volume:

$$\delta t = \frac{3\pi\mu r_p}{k_B T} \left[ \frac{1}{n_p \pi (r_{fv} + r_p)^2} \right]^2 \quad (1.4)$$

Let us examine the case of  $r_p=25$  nm and  $r_{fv}=140$  nm; given a fluid medium of room temperature water, the time between Brownian motion successive collisions of nanoparticles and our focal volume is  $\delta t \approx 120$ min. Using the bulk fluid speed and Equation 3.5, the time between bulk particle motion successive collisions is  $\delta t \approx 14$ sec. Thus, the effects of Brownian motion on our calculations of focal volume radius where the laser intensity is high enough to generate a bubble of detectable size is negligible.

## Appendix 2

### Scaled Temperature Response Surface Fits

In Chapter 5, we provided simple functional fits to certain regions of electron, phonon, and water maximum temperature response surfaces. We now provide more complex fits valid over larger ranges of system parameters. As before, we must stress that these fits are not valid if either the particle reaches its melting temperature or the particle has begun to ablate and reshape during the pulse. Additionally, the water fits are strictly inappropriate when the fluid has reached the kinetic spinodal and questionable when exceeding the binodal. In the later two cases, the phonon and electron temperatures will still be valid for pulse duration below diffusion time scales. More complete scaled temperature response surfaces:

$$\gamma \leq \beta^{\frac{2}{5}} \text{ or } \gamma \leq 1 \text{ \& } \beta \leq 1 \times 10^5$$

$$\hat{\theta}_e = c_1 + s_e(c_1 + c_2\hat{\beta}) \quad (2.1)$$

$$s_e = c_3 \text{atan}\left(c_4(\hat{\beta} - c_5)\right) + c_6 \quad (2.2)$$

$$0.0095 \leq \gamma \leq 1 \times 10^5 \text{ \& } \beta \leq 1 \times 10^4$$

$$\hat{\theta}_p = c_1 + c_2\hat{\gamma} + s_p(c_3 + c_4\epsilon - c_2\hat{\gamma}) \quad (2.3)$$

$$s_p = c_5 \text{atan}\left(c_6(\hat{\gamma} - c_7 + c_8\epsilon + c_9\epsilon^{c_{10}} + c_{11}\hat{\epsilon})\right) + c_{12} \quad (2.4)$$

$$0.0095 \leq \gamma \leq 1 \times 10^5 \text{ \& } \beta \leq 1 \times 10^4$$

$$\hat{\theta}_w = c_1 + c_2\epsilon + c_3\epsilon^2 + c_4\hat{\gamma} + s_w(c_5 + c_6e - c_4\hat{\gamma}) \quad (2.5)$$

$$s_w = (c_7 \text{atan}(c_8(\hat{\gamma} - c_9 + c_{10}\epsilon + c_{11}\epsilon^{c_{12}} + c_{13}\hat{\epsilon})) + c_{14}) \quad (2.6)$$

where:

$$c_e = (-2.6982, 1.0063, -0.1580, 0.3171, 2.5753, -0.2360)$$

$$c_p = (-7.0882, 1.0189, -0.9817, 0.9125, 0.1647, 0.5273, 25.8423, -3.5395, 16.9239, 0.5351, -6.7545, 0.2410)$$

$$c_w = (-5.5874, -0.7014, 0.1765, 0.7032, 5.0804, 0.8570, 0.4918, 0.4639, 39.9110, -11.5165, 38.9074, 0.6026, -13.1262, 0.3147)$$

For all fits,  $\hat{\chi} = \ln(\chi)$ . Coefficient vectors have been optimized using Matlab's built-in nonlinear least-squares curve fitting tools. The fits agree with numerical results for the given parameter range to within a 95% confidence interval of  $\pm 4.7\%$ ,  $\pm 0.69\%$ ,  $\pm 0.44\%$ , for the water, phonon, and electron temperature systems, respectively. Corresponding plots of each fit are given in the following figures.

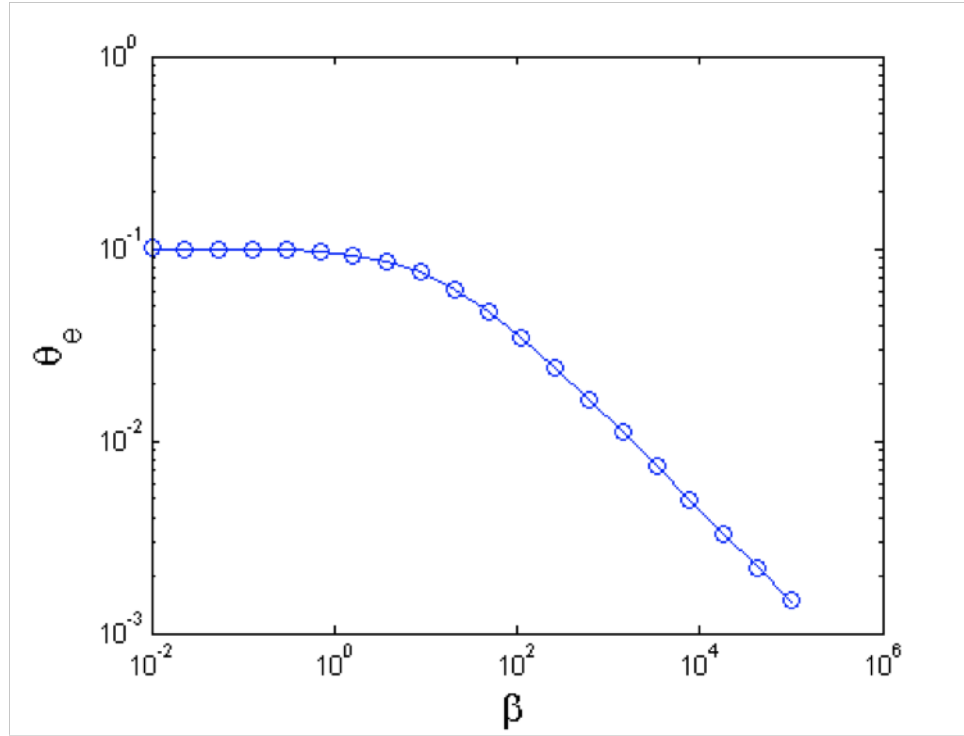


**Figure 2.1:** Maximum scaled particle electron temperatures for all  $\epsilon$ 's as a function of  $\beta$ . Numerical results are indicated by open circles while the fit of Eq. 2.1 is a solid line.

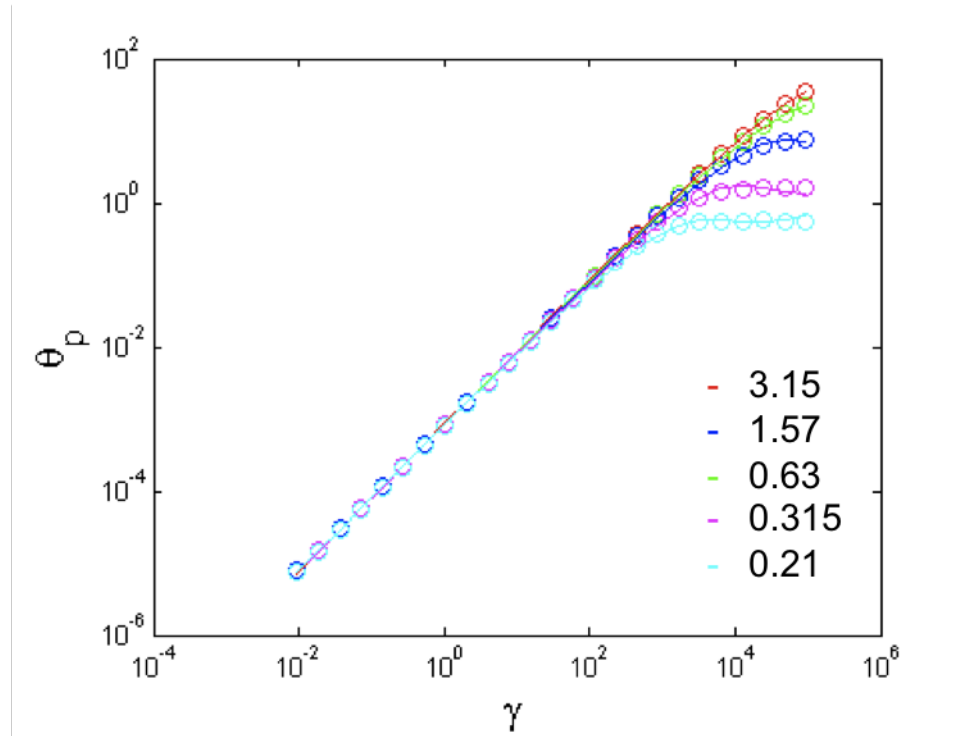


**Figure 2.2:** Maximum scaled particle phonon temperatures for all  $\epsilon$ 's (indicated by color) as a function of  $\gamma$ . Numerical results are indicated by open circles while the fit of Eq. 2.3 is a solid line.

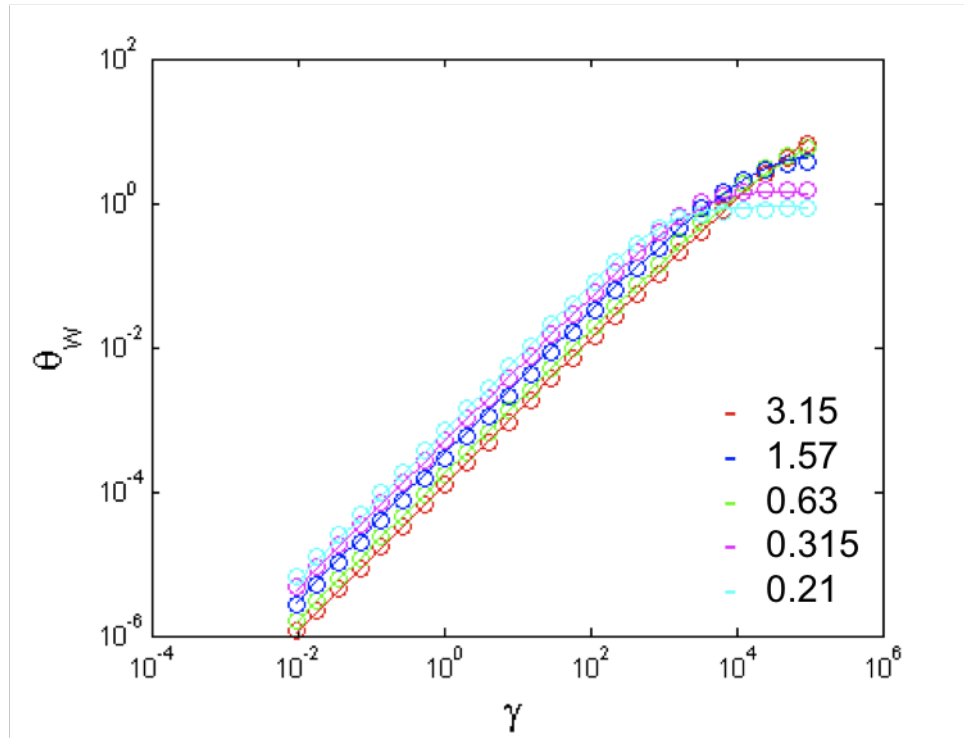


**Figure 2.3:** Maximum scaled surface water temperatures for all  $\epsilon$ 's (indicated by color) as a function of  $\gamma$ . Numerical results are indicated by open circles while the fit of Eq. 2.6 is a solid line.

## Bibliography

- [1] “Cancer statistics 2009,” *American Cancer Society*, 2009.
- [2] N. J. Durr, T. Larson, D. Smith, B. Korgel, K. Sokolov, and A. Yakar, “Two-photon luminescence imaging of cancer cells using molecularly targeted gold nanorods,” *Nano Letters*, vol. 7, no. 4, pp. 942–945, 2007.
- [3] A. Breslow, “Thickness, cross-sectional areas and depth of invasion in the prognosis of cutaneous melanoma,” *Annals Surgery*, vol. 172, pp. 902–908, 1970.
- [4] T. Friedmann, *The Development of Gene Therapy*. Cold Spring Harbor, 1998.
- [5] J. Hanna, S. Markoulaki, P. Schorderet, B. Carey, C. Beard, M. Wernig, M. Creighton, E. Steine, J. Cassady, R. Foreman, C. Lengner, J. Dausman, and R. Jaenisch, “Direct reprogramming of terminally differentiated mature b lymphocytes to pluripotency,” *Cell*, vol. 133, pp. 250–264, 2008.
- [6] M. Arruebo, M. Valladares, and A. González-Fernández, “Antibody-conjugated nanoparticles for biomedical applications,” *Journal of Nanomaterials*, vol. 1, 2009.
- [7] N. Yang, “Gene transfer into mammalian somatic cells,” *Critical Review of Biotechnology*, vol. 12, no. 4, 1992.
- [8] A. Vogel, J. Noack, G. Hüttman, and G. Paltauf, “Mechanisms of femtosecond laser nanosurgery of cells and tissues,” *Applied Physics B*, 2005.

- [9] C. B. Schaffer, A. Brodeur, and E. Mazur, “Laser-induced breakdown and damage in bulk transparent materials induced by tightly-focus femtosecond laser pulses,” *Measurement Science and Technology*, 2001.
- [10] P. Tsai, P. Blinder, B. Migliori, J. Neev, Y. Jin, J. Squier, and D. Kleinfeld, “Plasma-mediated ablation: an optical tool for submicrometer surgery on neuronal and vascular systems,” *Current Opinions in Biotechnology*, vol. 20, 2009.
- [11] J. Noack and A. Vogel, “Laser-induced plasma formation in water at nanosecond to femtosecond time scales: calculation of thresholds, absorption coefficients, and energy density,” *Journal of Quantum Electronics*, vol. 35, no. 8, 1999.
- [12] M. Perry, B. Stuart, P. Banks, M. Feit, V. Yanovsky, and A. Rubenchik, “Ultrashort-pulse laser machining of dielectric materials,” *Journal of Applied Physics*, vol. 85, no. 9, 1999.
- [13] C. H. Fan, J. Sun, and J. Longtin, “Breakdown threshold and localized electron density in water induced by ultrashort pulses,” *Journal of Applied Physics*, vol. 91, no. 4, 2002.
- [14] T. Itina, J. Hermann, P. Delaporte, and M. Sentis, “Modeling of metal ablation induced by ultrashort laser pulses,” *Thin Solid Films*, vol. 453, 2004.
- [15] C. Arnold, A. Heisterkamp, W. Ertmer, and H. Lubatschowski, “Streak formation as side effect of optical breakdown during processing the bulk of transparent kerr media with ultra-short laser pulses,” *Applied Physics B*, vol. 80, 2005.
- [16] A. Vogel, K. Nahen, D. Theisen, R. Birngruber, R. J. Thomas, and B. A. Rockwell, “Influence of optical aberrations of laser-induced plasma formation



- in water and their consequences for intraocular photodisruption,” *Applied Optics*, vol. 38, no. 16, 1999.
- [17] C. Arnold, A. Heisterkamp, W. Ertmer, and H. Lubatschowski, “Computational model for nonlinear plasma formation in high na micromachining of transport materials and biological cells,” *Optics Express*, vol. 15, no. 16, 2007.
  - [18] F. R. Gilmore, “The growth or collapse of a spherical bubble in a viscous compressible liquid,” Tech. Rep. 26-4, Hydrodynamics Laboratory, California Institute of Technology, Pasadena, California, April 1952.
  - [19] E. Faraggi, B. S. Gerstman, and J. Sun, “Biophysical effects of pulsed lasers in the retina and other tissues containing strongly absorbing particles: shockwave and explosive bubble generation,” *Journal of Biomedical Optics*, vol. 10, no. 6, 2005.
  - [20] A. Vogel, S. Busch, and U. Parlitz, “Shock wave emission and cavitation bubble generation by picosecond and nanosecond optical breakdown in water,” *Journal of Acoustics*, vol. 100, no. 1, 1996.
  - [21] E. Brujan, T. Ikeda, and Y. Matsumoto, “On the pressure of cavitation bubbles,” *Experimental and Thermal Fluid Science*, vol. 32, 2008.
  - [22] C. Schaffer, N. Nishimura, E. Glezer, A. Kim, and E. Mazur, “Dynamics of femtosecond laser-induced breakdown in water from femtoseconds to microseconds,” *Optics Express*, vol. 10, no. 3, 2002.
  - [23] W. Lauterborn and C.-D. Ohl, “Cavitation bubble dynamics,” *Ultrasonics Sonochemistry*, vol. 4, 1997.

- [24] D. Lapotko, E. Lukianova, and A. Oraevsky, “Selective laser nano-thermolysis of human leukemia cells with microbubbles generated around clusters of gold nanoparticles,” *Lasers in Surgery and Medicine*, vol. 38, 2006.
- [25] D. Lapotko, “Optical excitation and detection of vapor bubbles around plasmonic nanoparticles,” *Optical Society of America*, 2009.
- [26] V. Zharov, V. Galitovsky, and M. Viegas, “Photothermal detection of local thermal effects during selective nanophotothermolysis,” *Applied Physics Letters*, vol. 83, no. 24, 2003.
- [27] V. Kotaidis and A. Plech, “Cavitation dynamics on the nanoscale,” *Applied Physics Letters*, vol. 87, 2005.
- [28] A. Ben-Yakar, O. Ekici, and D. Eversole, “Spherical and anisotropic metal nanomaterials in laser-based cancer therapy,” *Metallic Nanomaterials*, vol. 1, pp. 493–539, 2009.
- [29] W. Wagner and Pruß, “The iapws formulation 1995 for the thermodynamic properties of ordinary water substance for general and scientific use,” *Journal of Physical Chemistry Reference Data*, vol. 31, 2002.
- [30] S. B. Kiselev, “Kinetic boundary of metastable states in superheated and stretched liquids,” *Physica A*, vol. 269, 1999.
- [31] A. Saul and W. Wagner, “Chemical reference data,” *Journal of Physical Chemistry*, vol. 12, 1989.
- [32] B. Cox and P. Beard, “Fast calculation of pulsed photoacoustic fields in fluids using k-space methods,” *Journal of Acoustic Society of America*, vol. 117, no. 6, 2005.

- [33] I. Akhatov, O. Lindau, A. Topolnikov, R. Mettin, N. Vakhitova, and W. Lauterborn, "Collapse and rebound of a laser-induced cavitation bubble," *Physics of Fluids*, vol. 13, no. 10, 2001.
- [34] S. Müller, M. Bachmann, D. Kröninger, T. Kurz, and P. Helluy, "Comparison and validation of compressible flow simulations of laser-induced cavitation bubbles," *Computers and Fluids*, vol. 38, 2009.
- [35] T. Juhasz, A. Kastis, C. Suarez, Z. Bor, and W. Bron, "Time-resolved observations of shock waves and cavitation bubbles generated by femtosecond laser pulses in corneal tissue and water," *Lasers in Surgery and Medicine*, vol. 19, 1996.
- [36] E. A. Brujan, K. Nahen, P. Schmidt, and A. Vogel, "Dynamics of laser-induced cavitation bubbles near an elastic boundary," *Journal of Fluid Mechanics*, vol. 433, 2001.
- [37] E. Klaseboer, C. Turangan, and B. Khoo, "Dynamic behaviour of a bubble near an elastic infinite interface," *International Journal of Multiphase Flow*, vol. 32, 2006.
- [38] X. Trepas, M. Grabulosa, F. Puig, G. Maksym, D. Navajas, and R. Farré, "Viscoelasticity of human alveolar epithelial cells subjected to stretch," *American Journal of Physiology*, vol. 284, 2004.
- [39] K. R. Rau, P. A. Quinto-Su, A. N. Hellman, and V. Venugopalan, "Pulsed laser microbeam-induced cell lysis: time-resolved imaging and analysis of hydrodynamic effects," *Biophysical Journal*, vol. 91, 2006.
- [40] N. Nishimura, C. Schaffer, and D. Kleinfeld, "In vivo manipulation of biological systems with femtosecond laser pulses," *Proceedings of SPIE*, 2006.

- [41] M. Yanik, H. Cinar, H. N. Cinar, A. Chisholm, Y. Jin, and A. Ben-Yakar, "Nerve regeneration in *caenorhabditi elegans* after femtosecond laser axotomy," *Nature*, vol. 432, 2004.
- [42] R. Brinkmann, G. Hüttmann, J. Rögener, J. Roider, and R. Birngruber, "Origin of retinal pigment epithelium cell damage by pulsed laser irradiance in the nanosecond to microsecond time regime," *Lasers in Surgery and Medicine*, vol. 27, no. 5, 2000.
- [43] J. Neumann and R. Brinkmann, "Cell disintegration by laser-induced transient microbubbles and its simultaneous monitoring by interferometry," *Journal of Biomedical Optics*, vol. 11, no. 4, 2006.
- [44] K. R. Rau, A. Guerra, A. Vogel, and V. Venugoplan, "Investigation of laser-induced cell lysis using time-resolved imaging," *Applied Physics Letters*, vol. 84, no. 15, 2004.
- [45] Y. Hosokawa, S. Iguchi, R. Yasukuni, C. Shukunami, and H. Masuhara, "Gene delivery process in a single animal cell after femtosecond laser microinjection," *Applied Surface Science*, 2009.
- [46] W. Watanabe, S. Matsunaga, T. Higashi, K. Fukui, and K. Itoh, "*In-vivo* manipulation of fluorescently labeled organelles in living cells by multiphoton excitation," *Journal of Biomedical Optics*, vol. 13, no. 3, 2008.
- [47] N. Khlebtsov and L. Dykman, "Optical properties and biomedical applications of plasmonic nanoparticles," *Journal of Quantitative Spectroscopy & Radiative Transfer*, 2010.
- [48] C. Bohren and D. Huffman, *Absorption and Scattering of Light by Small Particles*. Wiley, 2001.

- [49] S. J. Oldenburg, R. D. Averitt, S. L. Westcott, and N. J. Halas, "Nanoengineering of optical resonances," *Chemical Physics Letters*, vol. 288, no. 2-4, pp. 243 – 247, 1998.
- [50] S. Link, M. Mohamed, and M. El-Sayed, "Simulation of the optical absorption spectra of gold nanorods as a function of their aspect ratio and the effect of the medium dielectric constant," *Journal of Physical Chemistry*, vol. 103, no. 16, pp. 3073–3077, 1999.
- [51] S. Singh, H. Grossniklaus, S. Kang, H. Edelhauser, B. Ambati, and U. Kompella, "Intravenous transferring, rgd peptide and dual-targetted nanoparticle enhance anti-vegf intrareceptor gene delivery to laser-induced cnv," *Gene Therapy*, vol. 16, 2009.
- [52] B. Kang, M. Mackley, and M. El-Sayed, "Nuclear targetting of gold nanoparticles in cancer cells induced dna damage, causing cytokinesis arrest and apoptosis," *Journal of the American Chemical Society*, vol. 132, 2010.
- [53] R. Letfullin, C. Joenathan, T. George, and V. Zharov, "Laser-induced explosion of gold nanoparticles: potential role for nanophotothermolysis of cancer," *Future Medicine*, 2006.
- [54] T. Q. Qiu and C. L. Tien, "Short-pulse laser heating on metals," *International Journal of Heat and Mass Transfer*, vol. 35, 1992.
- [55] T. Q. Qiu and C. L. Tien, "Heat transfer mechanisms during short-pulse laser heating on metals," *Journal of Heat Transfer*, vol. 155, 1992.
- [56] J. K. Chen, D. Y. Tzou, and J. E. Beraun, "A semiclassical two-temperature model for ultrafast laser heating," *International Journal of Heat and Mass Transfer*, vol. 46, 2006.

- [57] V. Kotaidis, C. Dahmen, G. von Plessen, F. Springer, and A. Plech, "Excitation of nanoscale vapor bubbles at the surface of gold nanoparticles in water," *Journal of Chemical Physics*, vol. 124, 2006.
- [58] E. M. Logothetis and P. L. Hartman, "Laser-induced electron emission from solids: Many-photon photoelectric effects and thermionic emission," *Phys. Rev.*, vol. 187, no. 2, pp. 460–474, 1969.
- [59] N. M. Bulgakova, R. Stoian, A. Rosenfeld, and I. Hertel, "A general continuum approach to describe fast electronic transport in pulsed laser irradiated materials: the problem of coulomb explosion," *Applied Physics A*, vol. 81, 2005.
- [60] L. A. DuBridge, "Theory of energy distribution of photoelectrons," *Physical Review*, vol. 43, pp. 727–741, 1933.
- [61] J. H. Bechtel, W. Smith, and N. Bloembergen, "Two-photon photoemission from metals induced by picosecond laser pulses," *Physical Review B*, vol. 15, no. 10, 1977.
- [62] D. M. Riffe, X. Y. Wang, M. C. Downer, D. L. Fisher, T. Tajima, J. L. Erskine, and R. M. More, "Femtosecond thermionic emission from metals in the space-charge-limited regime," *Journal of Optics Society of America*, vol. 10, no. 8, 1993.
- [63] P. K. Kennedy, "A first-order model for computation of laser-induced breakdown thresholds in ocular and aqueous media: part i-theory," *IEEE journal of Quantum Electronics*, vol. 31, no. 12, pp. 2241–2250, 1995.
- [64] T. Wu, S. Kalim, C. Callahan, M. Teitell, and P. Chiou, "Image patterned molecular delivery into live cells using gold particle coated substrates," *Optical Society of America*, 2008.

- [65] L. Tong, Y. Zhao, T. B. Huff, M. N. Hansen, A. Wei, and J. Cheng, "Gold nanorods mediate tumor cell death by compromising membrane integrity," *Advanced Materials Deerfield*, vol. 19, 2007.
- [66] J. Neumann and R. Brinkmann, "Boiling nucleation on melanosomes and microbeads transiently heated by nanosecond and microsecond laser pulses," *Journal of Biomedical Optics*, vol. 10, no. 2, 2005.
- [67] R. Roy, C. H. Farny, T. Wu, R. G. Holt, and T. W. Murray, "Nucleating acoustic cavitation with optically heated nanoparticles," *AIP Conference Proceedings*, vol. 838, 2006.
- [68] C. Pistillides, E. K. Joe, X. Wei, R. R. Anderson, and L. C. P, "Selective cell targeting with light-absorbing microparticles and nanoparticles," *Biophysical Journal*, vol. 84, 2003.
- [69] D. Lapotko, "Pulsed photothermal heating of the media during bubble generation around gold nanoparticles," *International Journal of Heat and Mass Transfer*, vol. 52, 2009.
- [70] D. Leszczynski, C. M. Pitsillides, R. K. Pastila, R. R. Anderson, and C. P. Lin, "Laser-beam-triggered microcavitation: a novel method for selective cell destruction," *Radiation Research*, vol. 156, 2001.
- [71] D. Lapotko and E. Lukianova, "Laser-induced micro-bubbles in cells," *International Journal of Heat and Mass Transfer*, vol. 48, 2005.
- [72] C. P. Lin and R. R. Anderson, "Selective cell killing by microparticle absorption of pulsed laser radiation," *IEEE Journal of Selected Topics in Quantum Electronics*, vol. 5, no. 4, 1999.

- [73] D. O. Lapotko and E. Lukianova, “Laser-induce bubbles in living cells,” *Lasers in Surgery and Medicine*, vol. 38, 2006.
- [74] G. Frens, “Controlled nucleation for the regulation of the particle size in monodisperse gold suspensions,” *Nature Physical Science*, vol. 241, 1973.
- [75] H. Urey, “Spot size, depth-of-focus, and diffraction ring intensity formulas for truncated gaussian beams,” *Applied Optics*, vol. 43, pp. 620–625, 2004.
- [76] E. Hecht and A. Zajac, *Optics*. Oxford University Press, 2005.
- [77] M. Mitchner and C. H. Kruger, *Partially Ionized Gases*. John Wiley and Sons Inc, 1973.
- [78] N. Nedyalkov, T. Sakai, T. Miyashita, and M. Obara, “Near field properties in the vicinity of gold nanoparticles placed on various substrates for precise nanostructuring,” *Journal of Applied Physics D*, vol. 39, pp. 5037–5042, 2006.
- [79] D. Eversole, B. Lukyanchuk, and A. Ben-Yakar, “Plasmonic laser nanoablation of silicon by the scattering of femtosecond pulses near gold nanospheres,” *Applied Physics A*, vol. 89, pp. 283 – 291, 2007.
- [80] J. Kirkwood and H. Bethe, “The pressure wave produced by an underwater explosion,” Tech. Rep. 588, OSRD, 1942.
- [81] O. Ekici, M. K. Lee, and A. Ben-Yakar, “Thermal analysis of gold nanorods heated with femtosecond laser pulses,” *Journal of Physics D*, vol. 41, 2008.
- [82] A. Volkov, C. Sevilla, and L. Zhigilei, “Numerical modeling of short pulse laser interaction with au nanoparticle surrounded by water,” *Applied Surface Science*, vol. 253, 2007.



- [83] J. Chen, W. Latham, and J. Beraun, “The role of electronphonon coupling in ultrafast laser heating,” *Journal of Laser Applications*, vol. 17, 2005.
- [84] A. Plech, V. Kotaidis, S. Gresillon, C. Dahmen, and G. von Plessen, “Laser-induced heating and melting of gold nanoparticles studied by time-resolved x-ray scattering,” *Physical Review B*, vol. 70, 2004.
- [85] Y. Morinishi, O. Vasilyev, and T. Ogi, “Fully conservative finite difference scheme in cylindrical coordinates for incompressible flow simulations,” *Journal of Computational Physics*, vol. 197, 2004.
- [86] J. D. McWhirter, “Extinction coefficient and skin depth of alkali metals from 10 to 100 nm,” *Optica and Lasers in Engineering*, vol. 28, pp. 305–309, 1996.
- [87] E. D. Palik, *Handbook of optical constants of solids*. Academic Press, 1998.
- [88] G. Chen, *Nanoscale energy transport and conversion*. Oxford University Press, 2005.
- [89] S. Nolte, C. Momma, H. Jacobs, A. Tünnermann, B. Chichkov, B. Wellegehausen, and H. Welling, “Ablation of metals by ultrashort laser pulses,” *Journal of Optics Society*, vol. 14, no. 10, 1997.
- [90] J. Girardeau-Montaut and C. Girardeau-Montaut, “Theory of ultrashort nonlinear multiphoton photoelectric emission from metals,” *Phys. Rev. B*, vol. 51, no. 19, pp. 13560–13567, 1995.
- [91] J. Fujimoto, J. Liu, E. Ippen, and N. Bloembergen, “Femtosecond laser interaction with metallic tungsten and nonequilibrium electron and lattice temperatures,” *Phys. Rev. Lett.*, vol. 53, no. 19, pp. 1837–1840, 1984.
- [92] E. Hecht, *Optics*. Addison Wesley, 2002.

- [93] H. Xu, “Electromagnetic energy flow near nanoparticles i: single spheres,” *Journal of quantitative spectroscopy and radiative transfer*, vol. 87, no. 1, pp. 53–67, 2004.
- [94] B. Lukyanchuk, N. Arnold, S. Huang, Z. Wang, and M. Hong, “Three-dimensional effects in dry laser cleaning,” *Applied Physics A*, vol. 77, no. 2, pp. 209–215, 2003.
- [95] A. Plech, V. Kotaidis, M. Lorenc, and J. Boneberg, “Femtosecond laser near field ablation from gold nanoparticles,” *Nature Physics*, vol. 2, 2006.
- [96] A. Vogel, N. Linz, S. Freidank, and G. Paltauf, “Femtosecond-laser-induced nanocavitation in water: implication for optical breakdown threshold and cell surgery,” *Physical Review Letters*, vol. 100, 2008.
- [97] A. N. Bashkatov, E. A. Genina, V. I. Kochubey, and V. V. Tuchin, “Optical properties of human skin subcutaneous and mucous tissues in the wavelength range from 400 to 2000 nm,” *Journal of Applied Physics D*, vol. 38, pp. 2543–2555, 2005.
- [98] A. Plech and V. Kotaidis, “Femtosecond laser near field ablation from gold nanoparticles,” *Laser & Photonics Review*, 2008.
- [99] J. Santiago, S. Wereley, C. Meinhart, D. Beebe, and R. Adrian, “A particle image velocimetry system from microfluidics,” *Experiments in Fluids*, vol. 25, pp. 316–319, 1998.
- [100] A. Bravel, “Vaccine delivery methods using viral vectors,” *Molecular Pharmaceutics*, vol. 4, no. 1, 2006.

- [101] L. Jiang and H.-L. Tsai, “A plasma model combined with an improved two-temperature equation for ultrafast laser ablation of dielectrics,” *Journal of Applied Physics*, vol. 104, 2008.
- [102] R. Zhao, R. Xu, Z. Shen, J. Lu, and X. Ni, “Experimental investigation of the collapse of laser-generated cavitation bubbles near a solid boundary,” *Optics and Laser Technology*, vol. 39, 2007.
- [103] E. A. Brujan, G. S. Keen, A. Vogel, and J. Blake, “The final stage of the collapse of a cavitation bubble close to a rigid boundary,” *Physics of Fluids*, vol. 14, no. 1, 2002.
- [104] A. A. Kokhanovksy, “Optical properties of bubbles,” *Journal of Optics: A*, vol. 5, 2003.
- [105] P. Martson, D. Langley, and D. Kingsbury, “Light scattering by bubbles in liquids: Mie theory, physical-optics approximations, and experiments,” *Applied Scientific Research*, vol. 38, 1982.
- [106] S. Gac, E. Zwaan, A. van den Berg, and C. Ohl, “Sonoporation of suspension cells with a single cavitation bubble in microfluidic confinement,” *Lab on a Chip*, vol. 7, 2007.
- [107] C.-D. Ohl, M. Arora, R. Ikinik, N. de Jong, M. Versluis, M. Delius, and D. Lohse, “Sonoporation from jetting cavitation bubbles,” *Biophysical Journal*, vol. 91, 2006.
- [108] P. K. Jain, X. Huang, I. El-Sayed, and M. El-Sayed, “Review of some interesting surface plasmon resonance-enhanced properties of noble metal nanoparticles and their applications to biosystems,” *Plasmonics*, vol. 2, 2007.

- [109] L. Tong, Q. Wei, A. Wei, and J. Cheng, “Gold nanorods as contrast agents for biological imaging: optical properties, surface conjugation and photothermal effects,” *Photochemistry and Photobiology*, vol. 85, 2009.

## Vita

Sigfried William Haering was born in Guayaquil, Ecuador on 27 August 1981. He received the Bachelor of Science degree in Engineering from the University of New Mexico and was commissioned an Officer in the United States Air Force in 2003. He entered active duty in February 2004, and was stationed at Wright-Patterson Air Force Base, Dayton, Ohio, where he worked at the Air Force Research Laboratory in the field of behavior and life predictions of gas turbine engine components. He separated from the USAF in 2007 to attend graduate school at the University of Texas at Austin in Mechanical Engineering.

Permanent address: 3204 #6  
Tom Green St. Austin, Texas 78705

This thesis was typeset with  $\text{\LaTeX}^\dagger$  by the author.

---

<sup>†</sup> $\text{\LaTeX}$  is a document preparation system developed by Leslie Lamport as a special version of Donald Knuth's  $\text{\TeX}$  Program.